ADDITIVE MANUFACTURING AND MATERIAL PROPERTY CHARACTERIZATIONS OF HIGH-PERFORMANCE CERAMICS AND CERAMIC COMPOSITES

A Thesis
Presented to
The Academic Faculty

by

Noah Dennis

In Partial Fulfillment
of the Requirements for the Degree
Master of Science in Mechanical Engineering

Georgia Institute of Technology
May 2015

ADDITIVE MANUFACTURING AND MATERIAL PROPERTY CHARACTERIZATIONS OF HIGH-PERFORMANCE CERAMICS AND CERAMIC COMPOSITES

Approved by:

Dr. Shuman Xia, Advisor
School of Mechanical Engineering
Georgia Institute of Technology

Dr. H. Jerry Qi
School of Mechanical Engineering
Georgia Institute of Technology

Dr. Hailong Chen
School of Mechanical Engineering
Georgia Institute of Technology

Date Approved: April 3, 2015

ACKNOWLEDGEMENTS

First, I would like to thank my advisor, Dr. Shuman Xia, for offering me the opportunity to work on this project for the past year-and-a-half. You have been extremely helpful in guiding me throughout this project and the research skills you have taught me will serve me well for years to come.

I also would like to thank my committee members: Dr. H. Jerry Qi and Dr. Hailong Chen. I appreciate both of you taking time out of your busy schedules to review this thesis. Additionally, I would like to thank Eric Woods for teaching me the intricacies of taking SEM images and performing EDS analysis, which were crucial parts of the microstructural analysis work.

To the other graduate students in my lab, Xueju Wang and Zhipeng Pan, I would like to take this opportunity to thank you for your support during this whole process. Your help with critiquing the presentation that goes along with this thesis was much appreciated and I wish you both the best on your future endeavors. I would also like to thank Mu Lu, an undergraduate student in my lab, for making the control box for the prototype system.

Lastly, I would like to thank my parents. I love you both with all my heart and this is a product of your work as wonderful parents as it is of mine. You have supported me throughout my entire education and I would not be where I am today without you.

TABLE OF CONTENTS

LIST OF TABLES

LIST OF FIGURES

SUMMARY

Ceramics serve as important engineering materials that have the ability to offer unique advantages over metals and polymers in various extreme-environment applications (e.g., high temperature, corrosion, radiation). This ability, however, has yet to be realized because ceramics are very susceptible to mechanical failure due to their inherent brittleness and low fracture toughness. In order to develop ceramic parts capable of functioning within these environments, ultra-tough ceramic parts must be fabricated with the complex geometries necessary for these applications. To achieve this objective, a new additive manufacturing method is proposed here; the purpose of which is to establish the creation of a new field of additive manufacturing, which involves the fabrication of high-performance ceramics for demanding applications such as high-efficiency jet engines and next-generation nuclear reactors.

A prototype system of the proposed method has been developed. The prototype system is a multi-functional setup that involves the use of the droplet-on-demand (DOD) or fused deposition modeling (FDM) printing technique to deposit build material in a layer-by-layer process. The build material consists of a liquid pre-ceramic polymer (PCP) that is mixed with active fillers to counteract the porosity and shrinkage associated with PCPs during pyrolysis. This facilitates near-net-shape production of final ceramic parts, thus maximizing their strength and toughness.

To validate the system's near-net-shape capabilities, microstructural analysis was executed. This involved the use of scanning electron microscope (SEM) images, energy-dispersive x-ray spectroscopy (EDS), and x-ray photoelectron spectroscopy (XPS) in

addition to a calculation of the volume shrinkage experienced during pyrolysis. Mechanical testing of fabricated samples was performed to measure material properties such as Young's modulus, hardness, and fracture toughness. The addition of carbon nanofibers (CNFs) into the build material was executed to investigate toughening enhancement of fabricated samples. Like with the samples made without the use of CNFs, microstructural analysis and mechanical testing were executed.

The results of the microstructural analysis and mechanical testing indicate that the proposed method can fabricate parts with near-net-shape capabilities and with fracture toughness similar to that of common engineering ceramics. Additionally, the prototype system shows that with some manipulation of the build material, ultra-tough ceramic fabrication should be achievable using the proposed method.

CHAPTER 1

INTRODUCTION

1.1 Existing Additive Manufacturing Techniques

Before the field of additive manufacturing came into existence, parts were made from bulk material that was machined into the final part. Types of manufacturing methods that followed this procedure have several drawbacks. One of the main drawbacks is that once the part is completed, there is usually a significant amount of excess material left over that usually has to be discarded, which means that a significant portion of the money that goes into purchasing the beginning bulk material goes to waste since much of the material is not used. Another drawback is that the available machining methods impose limitations on how parts can be designed. Therefore, there was a need to have a method in which parts were created without any of the drawbacks mentioned.

A little over three decades ago the field of additive manufacturing was established.[1] Techniques that employ additive manufacturing allowed for much more freedom in the design of parts and drastically decreased the amount of waste material that would be involved in fabrication. This is because as opposed to starting from bulk material, which is machined down in order to make a part, material is added in a way that produces the finished part with minimal machining afterwards necessary, if at all.

Over the past three decades, several additive manufacturing techniques have been developed and improved making additive manufacturing one of the most attractive manufacturing processes for fabricating parts nowadays. Techniques include stereolithography (STL), selective laser sintering (SLS), photo-masking, fused deposition

modeling (FDM), laminated object manufacturing (LOM), ballistic particle manufacturing (BPM), and three-dimensional (3D) inkjet printing.

The main advantage of additive techniques is that they allow for the design of geometrically diverse and complex parts with relative ease. However, a significant disadvantage associated with these techniques is that the parts they fabricate are usually brittle and would only serve well as prototypes as opposed to structural parts for real-world engineering applications. Therefore, there is a need to produce parts via additive manufacturing that will function successfully in real-world systems. Here, a new type of additive manufacturing technique is proposed that will address this problem, specifically for ceramics.

The first additive manufacturing method ever developed was stereolithography.[1] Stereolithography makes use of computed aided design (CAD) files in order to fabricate parts. The geometry of the part can be made using three-dimensional (3D) CAD software such as ProEngineer and Solidworks. Using CAD software, one can draw the part, use mathematical equations to describe the part[2], or can even scan data from images of already made parts using Magnetic Resonance Imaging (MRI) or Computed Tomography (CT)[3]. Once the part is modeled, it is saved as a CAD file, which describes the geometry and size of the part. Then, in order for the part to be printed, the file needs to be converted into a STL file. STL files list coordinates of triangles that together make up the surface of the object. The object is virtually sliced into layers of predetermined thickness so that the part will be made layer-by-layer. Once the CAD file had been converted into a STL file, the file is uploaded to a stereolithography apparatus (SLA), which serves as the

machine that performs the actual manufacturing of the part. SLA machines have two types of configurations: bath configuration and layer configuration.

In the bath configuration, an ultra-violet (UV) light beam traces a two-dimensional (2D) cross-section onto a platform in a tub of liquid photo-polymerizable resin, which cures when illuminated by the UV light.[4] Once the cross-section is cured, the platform is lowered further into the resin by a distance equivalent to the layer thickness described in the STL file. A second layer is fabricated on top of the first layer using the procedure explained above. This process is repeated layer-by-layer until the part is completed. To ensure that layers are uniform, a blade loaded with resin is situated in between layers so as to level the liquid resin before it is polymerized.

On the other hand, in the layer configuration, the platform is placed above the liquid resin as opposed to being submerged in the resin as in the bath configuration.[4] The UV light is situated below the tub of liquid resin, which has an optically clear bottom so that light can shine through the tub in order to cure the resin. In this configuration, a thin layer of liquid resin fills the space between the top of the tub and the platform and then, just like in the bath configuration, the UV light traces out the cross-section to be cured. Once curing is completed, the platform is raised a distance equivalent to the layer thickness determined by the STL file and the process is repeated for each layer until the product is finished.[5-7]

Although the STL method provides advantages compared to non-additive manufacturing methods, the method has its disadvantages as well. In both configurations, post-curing is required to make sure that all the reactive groups of the resin have been cured so that bonding is fully strengthened.[4, 8, 9] Other limitations involve the materials

that SLA machines use as build material. One limitation is that only one resin can be used at a time. Another limitation is that the types of resin are limited to epoxy and acrylic-based resins, which are brittle and can shrink during polymerization. [1, 4, 8]

Another type of additive manufacturing process is photo-masking. This method is initialized by electrostatically charging a glass plate with a negative image of the cross-section of the part on top of it. While charging occurs, a thin layer of photopolymer is spread across a surface. Once charging of the glass plate is complete, the plate is laid on top of the polymer. The surface is exposed to a UV laser, which cures all exposed areas of the polymer. The liquid polymer remaining is removed and replaced with hot wax, which serves as support material. Once the wax is solidified, the layer surface is milled down to the desired layer thickness. The mask is discharged so that it can be used for the next layer. This process is repeated until a complete part has been formed.[10] Advantages of photo-masking are that the layer is cured all at once[11] and that no post-curing is necessary. Disadvantages include the need for support material and that the support material must be melted off after fabrication in order to achieve the desired part.

In addition to using liquid resin as build material, additive manufacturing techniques have been developed that use powder as build material. One of these techniques is selective laser sintering (SLS).[12, 13] In SLS, a CO_2 laser is used to sinter successive layers of powder. At first, a thin layer of powder is applied to a workplace via a counter-rotating roller mechanism. The powder is heated to just below the melting temperature and the CO_2 laser traces out the cross-section on the powdered surface, further heating the powder to the sintering temperature. This procedure bonds the powder that has come into contact with the laser beam. The remaining powder is used as support

material for the next layer. Afterwards, the entire process is completed for each layer until the part is finished.[10]

An advantage of the SLS method is that it can implement a wide variety of material systems that such as polycarbonate, polyvinyl chloride (PVC), acrylonitrile butadiene styrene (ABS), nylon, resin, polyster, polypropane, polyurethane, and investment casting wax. Another advantage is that these materials are reusable if formed back into powder. In contrast, a major disadvantage of this method is that the sintering and cooling associated with SLS cause the fabricated part to be prone to shrinkage and warping, thus lowering its structural integrity.[10]

As with most technologies, some additive manufacturing techniques have become more popular than others. One technique that has become extremely popular in recent years is fused deposition modeling (FDM).[4, 10, 14] Typically, thermoplastic filaments are transported by two rollers down to the nozzle tip of the extruder of a printhead. In the head, the filament is heated to just above its melting temperature so that when it is deposited, solidification of the filament material occurs almost instantaneously (within 0.1 seconds). The printhead traces out the cross-section of the layer by moving horizontally in the x- and y-directions as the material flows out of the nozzle. Once the entire cross-section has been deposited, the head moves up in the z-direction a programmed distance. This process is repeated layer-by-layer until the whole part has been fabricated. Layers are bonded together via thermal heating.[10] Additionally, FDM can be used to fabricate metal and ceramic parts. But in this case, binders are usually mixed with metal or ceramic powders so that the resulting mixture can serve as filament material.[4]

As with the aforementioned techniques, FDM has its share of advantages and disadvantages. One of the disadvantages of FDM is that parts made with this technique are highly susceptible to staircase and chordal surface defects, which emanate from the slicing software and STL file format. Heterogeneities in the filament feed diameter and density can cause internal defects as well as effect how the material comes out of the nozzle.[15] The main advantage of FDM is the variety of build materials that can be implemented with this technique. These materials include polycarbonate (PC), polystyrene (PS), ABS, glass reinforced polymers[16], metals[17, 18], ceramics[17, 19-21], and bioresorbable materials[22].

Another, less popular, additive manufacturing technique is laminated object manufacturing (LOM), which is a process that creates parts from bonded paper, plastic, metal, or composite sheet stock.[10, 11] In this technique, layers of sheet material are stacked on top of one another. First, a layer of sheet material is loaded onto a stage. Then, a laser or razor traces out the cross-section of the part on the sheet.[23] The excess material is removed, a second layer of sheet material is placed on top of the first layer, and the procedure is repeated layer-by-layer until the part is completed. Layers are bonded together using adhesives or welding depending on which type of sheet stock is used.[4, 24] In addition to what has been stated, LOM also requires a heating step, which is done to make sure that the bonding material correctly serves its intended purpose.[4]

An advantage of LOM compared to FDM is that the heating step in LOM causes minimal defects and nonuniformities within the part.[25] A disadvantage of this technique is that if the temperature in the heating step is not correctly controlled, the part could possibly suffer delamination or structural damage.[26] One of the main disadvantages of

this technique though, is that the build materials that can be used are limited to whether they can be formed into sheets and are compatible with adhesive.[4]

Many paper printers currently in use have an inkjet printhead. In recent years, researchers have made use of inkjet technology and have applied it to the development of new additive manufacturing techniques such as ballistic particle manufacturing (BPM)[10] and three-dimensional (3D) inkjet printing[4, 10].

In BPM, a piezo-driven inkjet system is implemented to spit out droplets of melted material.[27] A layer is fabricated by moving the droplet nozzle of the inkjet system in the x- and y-directions as it traces out the cross-section of the layer onto a baseplate. Afterwards, the baseplate is lowered a specified distance and a new layer is traced on top of the old one. To ensure that adjacent layers bond together, the molten layer is cold-welded to the most recently deposited layer.[27] This process is repeated layer-by-layer until the part is completed. Build materials suggested for this technique include thermoplastics, aluminum, and wax because of their ability to be easily melted and solidified. A disadvantage of BPM is that support material is needed to counteract overhangs and voids.[10]

In 3D inkjet printing, solid powder particles are bounded together by inkjet printed liquid binder material. First, a layer of powder is laid out on a support stage. Then, an inkjet printhead projects droplets of liquid binder onto the powder in the places where solidification is supposed to occur. The stage drops a distance equivalent to the desired layer thickness and a second layer is created on top of the first using the same procedure. This process is repeated layer-by-layer until the desired part is achieved. Once the part is completely fabricated, the part is typically heat-treated to enhance binding.

During the manufacturing process, the remaining unbounded powder serves as support material and is removed once the part has been fabricated.

As with many existing additive manufacturing techniques, 3D inkjet printing has its own drawbacks and advantages. One drawback is that the binding liquid's chemical and physical properties will dominate the powder's chemical and physical properties, which limits what binding liquids can be used for toxicity reasons.[4, 28] Another drawback is related to optical transparency. If there is incomplete interaction of the liquid and powder, reduced transparency ensues and significant porosity as well as surface roughness is generated.[4] Also, as of 2014, non-powder based (usually polymer-based) inkjet methods do not exist.[4, 29] Some advantages of this method are that no additional support is needed and that fabrication does not require photo-polymerizable materials and liquids with modified viscosities.[4]

By looking at the advantages of additive manufacturing, it is clear that these techniques allow one to design parts with less restrictions than ever before. One now has the ability to create geometrically complex parts with relative ease, which could have a huge impact in the engineering field. On the other hand, by looking at the disadvantages associated with these techniques, it is evident that parts fabricated by these methods are usually brittle and would only serve well as prototypes as opposed to structural entities in real-world engineering applications. Therefore, there is a need to produce parts via additive manufacturing that will function successfully in real-world systems.

One material system that could benefit from the development of a new additive manufacturing technique is the ceramic material system. Ceramics serve as important engineering materials that have the ability to offer unique advantages over metals and

polymers in various extreme-environment applications (e.g., high temperature, corrosion, radiation). This ability, however, has yet to come to fruition because ceramics are very susceptible to mechanical failure due to their inherent brittleness and low fracture toughness. In order for development of well-functioning ceramic parts in these situations to take place, ultra-tough ceramic parts must be fabricated with the complex geometries necessary for these applications. To achieve this objective, a new additive manufacturing method is proposed here. Therefore, this method will serve to establish a new field of additive manufacturing, which involves the fabrication of high-performance ceramics for demanding applications, such as armor ceramics[30], high-efficiency jet engines, and next-generation nuclear reactors.

1.2 Fabrication of Ceramics

There are several existing techniques that have been used for fabricating parts made out of ceramic materials.[31-39] These manufacturing techniques can be split up into two different categories: non-additive methods[31, 38] and additive methods[32-37, 39]. These two categories differ in the way in which the ceramic is formed. Different non-additive ceramic manufacturing techniques include slip casting, ceramic shell casting, inject molding, hot wax molding, gel casting, tape-casting, throwing, dry pressing, isostatic pressing, hot isostatic pressing (HIP), hot pressure sintering, and pressure sintering.[31] Additive methods include 3D inkjet printing, SLS, STL, FDM, filament form 3D printing, aerosol jet printing, and direct inkjet printing.[40]

1.2.1 Non-Additive Ceramic Manufacturing Techniques

One of the most widely used non-additive ceramic forming techniques is slip casting. In slip casting, a liquid suspension filled with ceramic particles called the slip is poured into a mold.[41] Pores in the mold activate capillary action, which removes the liquid from the slip.[31] Once the liquid is completely removed, all that remains is a cast on the mold surface, which functions as the finished part once it has been fired. With this method, it is evident that the shape of the mold determines the shape of the part.

Another forming technique is die pressing, in which granular ceramic powder is uniaxially compacted while the powder undergoes confined compression within the die.[31] With this method, the shape of the die ultimately determines the shape of the finished product. Therefore, different dies will produce different shapes.

An alternative forming method is isostatic pressing (also referred to as cold isostatic pressing).[42] In this method, granular powder or die-pressed powder is transferred to a flexible airtight container located in a closed pressure vessel filled with liquid. The pressure increase within the vessel compacts whatever is in the container. Since the pressure increase takes place throughout the liquid, uniform pressure is applied over the whole surface area of the container. This accounts for uniform compaction of the powder and will allow for the powder to keep the general shape of the container and any internal tooling profile within.[31]

Another very popular ceramic forming technique is extrusion. Here, plastic mix of ceramic powder is put through a constructing die in order to make elongated shapes that have a constant cross-section.[43, 44] The mixture consists of fine ceramic powder particles with binder and plasticizer, which give the mixture the proper flow properties to ensure

successful extrusion.[31] The main limitation with extrusion is its shaping capability. Since extrusion can only produce parts with constant cross-sections, extrusion cannot be used to make parts with complex geometries.

Another type of casting technique is tape-casting. With tape-casting, ceramic slurry typically made with ceramic powder, solvent, plasticizer, and binder is casted onto a flat moving carrier surface. In this process, the slurry passes under a knife edge as the carrier surface moves along a support table.[45] Eventually, the solvent within the mixture evaporates resulting in a relatively dense flexible ceramic tape. Once the tape is stripped off the carrier surface, it can be stored in rolls to be used later. One of the main uses of tape-casting is for the manufacturing of electrical components.[31]

A typical non-additive method for producing ceramic parts with complex geometries is injection molding.[46] In this method, plastic mix is made and heated in a barrel located in a molding machine until the mixture has reached the appropriate temperature at which it can flow. When pressure is applied, a plunger is pressed against the heated mixture forcing it through an opening and onto the tool cavity. The molded part is then removed from the die and organic binder is slowly burned out in a controlled atmosphere by means of carefully controlled heating. Injection molding is a good process for making high-volume ceramics, turbo charger rotors, and thrust bearings. An advantage of this method is that it significantly cuts down on fabrication costs. There are also different types of injection molding. One type is low pressure injection molding (LPIM)[46], which is good for making ceramic parts using lower cost tools compared to those used for high pressure molding methods. Advantages of LPIM are that they have

the ability to make both complex and simple geometries and can produce parts with higher levels of integrated function.[31]

Another type of pressing is hot pressing, which consists of a powder/compacted preform that is put in a die (usually made of graphite).[47] External elevated temperature and uniaxial pressure is simultaneously applied to increase densification of the part. Disadvantages of using this method are that it can only be used for fabricating simple shapes and often diamond grinding is required in order for parts to achieve the necessary finished tolerances.[31]

Hot isostatic pressing (HIP), where the powder compact is sintered at a high temperature in a pressurized gas atmosphere, is another pressing technique.[48] Compacts used in this method either have to be impermeable to the pressurizing gas or be put in a gas-tight container. With an impermeable compact, sintering is performed before pressing in order to get rid of surface connected porosity. A benefit of HIP is that it leads to increased density and strength in parts made out of Technox zirconias.[31]

It is clear that there are several limitations with non-additive ceramic forming methods. Many of these methods are limited in the geometric shapes they can produce. For instance, although methods that require molds or dies are capable of producing complex geometries, a mold or a die can only produce parts with the same geometry. In order to make parts of varying geometry, multiple molds/dies are required to do so, which can significantly increase the fabrication cost. Therefore, the need for methods to reduce this cost was apparent. Additive techniques tackled this problem head on by being able to produce a wide variety of shapes quite easily.

1.2.2 Additive Ceramic Manufacturing Techniques

Over the past few decades, many of the additive manufacturing techniques discussed earlier[32-37] as well as a few others[39] have been modified/used in order to fabricate ceramic parts.

One of these techniques is 3D inkjet printing. In order to produce ceramic parts, binder is inkjet printed onto a ceramic powder bed in a layer-by-layer process. Once completed, the excess powder is removed and the part is sintered. Although 3D inkjet printing can easily produce parts of geometric complexity, the quality of these parts is usually poor due to the fact that coarse powder particles must be used in order to roll out the powder bed. To avoid this problem, one must first inkjet fine ceramic particles to fabricate a uniform layer of powder that serves as the powder bed. Then, the binder material needs to be inkjet printed onto the powder layer.[49] A drawback of this is that printing has to be manipulated so as to make sure that there is uniform powder diffusion within the powder layer to avoid density variations.[34]

A variation of 3D inkjet printing that has been implemented to produce ceramics is direct inkjet printing. This method consists of a suspension of ceramic particles mixed with binder and solvent that is printed into a desired pattern.[50-53] Once printed, the suspension is dried, burnt out, and sintered into the finished part. The main problem with this method is that low viscosity of the suspension is required for inkjet printing. This significantly lowers the amount of ceramic particles that can be added and also requires that these particles be well dispersed within the solution. The low ceramic content causes the material to be weak, therefore eliminating the ability to produce functional ceramic parts with this method.[34]

Another one of the main additive methods for ceramics is SLS. There are several parameters that affect the SLS process. These include the material choice, optical beam guidance system, powder delivery system, and laser irradiation strategies. Post-processing techniques such as post-sintering, infiltration, and bead blasting can also have an effect on the outcome. The disadvantage of the SLS method is that parts are prone to shrinkage, porosity, thermal instability, and mechanical instability.[36]

As stated prior, one of the most popular additive techniques is FDM. Although FDM typically makes parts out of plastic materials, especially ABS plastic, researchers have shown the capability of applying this process to ceramic materials.[32, 33, 35, 37] When applied to ceramics, FDM usually uses a mixture of ceramic particles dispersed in thermoplastic binder as the build material. As when applied to other material systems, this mixture can be formed into a solid flexible filament. Once the filament is fed through the printhead, the filament is heated to a flowable fluid state and deposited out of a nozzle attached to the printhead onto a stage. Typically, as the printhead deposits the filament, it moves in the x- and y-directions in order to trace out the 2D cross-section. This process is repeated layer-by-layer until the entire part has been made. Afterwards, the part goes through binder burnout and sintering to obtain the final product.

There are several disadvantages associated with FDM of ceramics. Since FDM uses a layer-by-layer technique, part integrity is impacted by void formation and insufficient inter-layer bonding, which cause cracks to occur.[54] Another disadvantage is that the inherent exposure to high-temperature thermal cycles results in poor mechanical performance.[55] Since the performance of a product depends on the feedstock material, FDM should be able to integrate several materials.[33] The main problem for tailoring the

FDM system for new materials with specific characteristics typically comes from using filament material. The advantage of using filament is counteracted by problems with its preparation and fabrication.[56] During deposition of the filament, buckling failure halts the fabrication process and requires user intervention to cool down and warm up filament so the process can continue.[56] Also, backpressure during deposition limits the volume fraction of ceramic powder within the filament, lowering the chance of successful sintering.[57]

1.3 Strengthening and Toughening Mechanisms

1.3.1 Strengthening Mechanisms

In order to increase the strength and the toughness of ceramic materials, one can employ strengthening and toughening mechanisms. To increase the strength of ceramic materials, there are two main methods. One of these is to reduce the number of cracks. By making the structure less flawed, a part has a lower chance of failure. The second method is to reduce the crack size. According to Griffith criterion, the part fails due to the size of the longest crack.[58] Since the fracture strength and the critical crack size are inversely related, smaller crack sizes will increase the fracture strength of the structure. By looking at these two methods, it is evident that they both help to increase the strength of ceramics.

1.3.2 Toughening Mechanisms

Unlike with strengthening mechanisms, there are several different toughening mechanisms.[59] These mechanisms can be split into two different categories: intrinsic

toughening and extrinsic toughening. In intrinsic toughening mechanisms, creating more stable microstructures and increasing precipitate particle spacing fundamentally change the material properties of the material to make a stronger, tougher ceramic.[60] Extrinsic toughening mechanisms, on the other hand, take place during crack propagation at the location of the crack.[60] Extrinsic toughening can be separated into two different categories: zone shielding and contact shielding. Zone shielding mechanisms take place on the crack tip whereas contact shielding mechanisms take place behind the crack. Examples of zone shielding are transformation toughening, microcrack toughening, and crack field void formation. Examples of contact shielding are crack bridging and crack sliding.[61]

Transformation toughening is one of the most popular methods and is typically done with the use of zirconia particles.[62] In this mechanism, a stress field located ahead of the crack induces a phase transformation of tetragonal particles to the monoclinic phase. The location of the transformation is called the process zone and it is located behind the crack.[63] In zirconia, transformation from the tetragonal to monoclinic phase causes a volume increase that applies a closing force on the crack. This volume increase also serves to provide resistance to crack propagation.[63] The reason why this mechanism is so popular is that it causes the ceramic to show similar behavior to that of steel when in the presence of an applied stress field ahead of the crack.[64] Although implementation of this mechanism greatly increases the strength and fracture toughness, there are several disadvantages that can cause this method to be undesirable in certain situations. First of all, in order for this method to work, the tetragonal phase has to be stable at room temperature. This requires the use of very fine (< 1 μm) particles, which could be very

expensive.[63] Secondly, increased temperatures counteract the benefits of transformation toughening. As the temperature of the material is increased, the driving force for the phase transformation is lowered. If the temperature is further increased, there will eventually be no driving force for the transformation, which means that the particles will remain in the tetragonal phase and no toughening will occur.[63] Whiskers or fibers in ceramic matrix composites are prone to high-temperature oxidation, which counteracts toughening as well.[63]

In transformation toughening, it is clear that the addition of ceramic particles into the ceramic matrix could increase strength and toughness. Research has shown that the addition of metal particles into the matrix could serve the same purpose.[65] The addition of metal particles within the matrix causes macroscopic cracks to leave behind metal particles or ligaments. When this happens, the metal particles/ligaments bridge the crack surface just behind the crack, therefore restraining the opening of the crack. This process is called crack bridging and can also be applied to non-metal material systems. This makes it more difficult for the crack to propagate, which means that a larger stress must be applied in order to cause failure. As with almost all methods, there are some situations that could occur as a result of using this method that would negatively affect the performance of toughening. If the metal particles are not well bonded to the matrix and the advancing crack tip is not attracted to the particles so as to leave bridges behind, this method will not be successful.

Another toughening mechanism is crack deflection toughening. Since the grain boundary toughness is a lot less than the lowest cleavage toughness of the crystal in many polycrystalline ceramics, macroscopic cracks propagate along the grain boundaries. Also,

since these grain boundaries have several different orientations and residual stress lies within the material, the crack will propagate in a tortuous manner, deflecting along grain boundaries as they shift orientation.[65] Crack deflection therefore slows down the movement of the crack, thus increasing the fracture toughness of the material.

Other extrinsic toughening mechanisms include microcrack toughening, macrocrack bridging, and crack sliding. In microcrack toughening, stable grain boundary microcracks are nucleated by high stress near the macroscopic crack tip. These microcracks function as a shield against the applied stress, thus lowering the stress felt by the crack tip.[65] Macrocrack bridging, a subtype of crack bridging, consists of uncracked grains serving as bridging elements that shield the crack tip. This lowers the stress intensity at the crack tip and slows down and/or stops crack propagation.[65] Crack sliding is similar to crack bridging in the way that is slows down/stops crack propagation. The difference is that in crack sliding, the two crack surfaces slide against one another at the crack surface interface to inhibit crack movement.[61]

1.4 Fabrication of Ultra-Tough Ceramics

Previous work on the fracture mechanics of heterogeneous material systems[66-68] shows the feasibility to produce ultra-tough ceramics. Specifically, one class of materials, pre-ceramic polymers (PCPs), provides promising properties that when tailored appropriately, could lead to the production of ultra-tough ceramic materials.[69] PCP materials, when pyrolyzed at ~1000^{o}C go through a polymer-to-ceramic transition, with sometimes as high as an 85wt% ceramic yield.[70]

One of the main reasons why PCPs are attractive as build materials in fabricating ceramics is that with the addition of nano-sized filler particles, one can produce crack-

free, dense, near-net-shape ceramic parts in just a single ceramization step.[69, 71-77] There are two types of fillers that can be used: inert and active. Inert fillers are ceramic powders that do not react with the ceramic residue, decomposition gas, or heating atmosphere.[78] Essentially, the addition of inert filler material dilutes the PCP, which decreases the amount of gas produced during pyrolysis. This reduces the amount of volume shrinkage that occurs during the polymer-to-ceramic conversion, thus reducing the likelihood of cracking.

Active fillers, on the other hand, are typically metallic or intermetallic powders that react with the ceramic residue, decomposition gases, and heating atmosphere.[72, 79] During pyrolysis, active fillers go through a metal-to-ceramic conversion, which causes volume expansion of the filler due to the large density increase of the filler that occurs during this process. This volume expansion counteracts the volume shrinkage associated with the PCP.[72] A schematic of the effect that active fillers have on the volume shrinkage experienced by the PCP during pyrolysis is shown in Figure 1. An observation of Figure 1 makes it evident that active fillers not only help the PCP maintain its geometry throughout pyrolysis but also help negate the porosity effect of pyrolysis. As with inert fillers, by just the addition of filler material alone, active fillers lower the amount of gas production during pyrolysis, which therefore lowers the amount of volume shrinkage that takes place. Also, the *in situ* reaction of the active filler with PCP lowers the local gas pressure.[72] The benefit of active fillers over inert fillers is that the reaction of active fillers with their surrounding environment allows for the possible fabrication of near-net-shape, uncracked, bulk ceramic parts, which correlates with the behavior shown in Figure 1.[69]

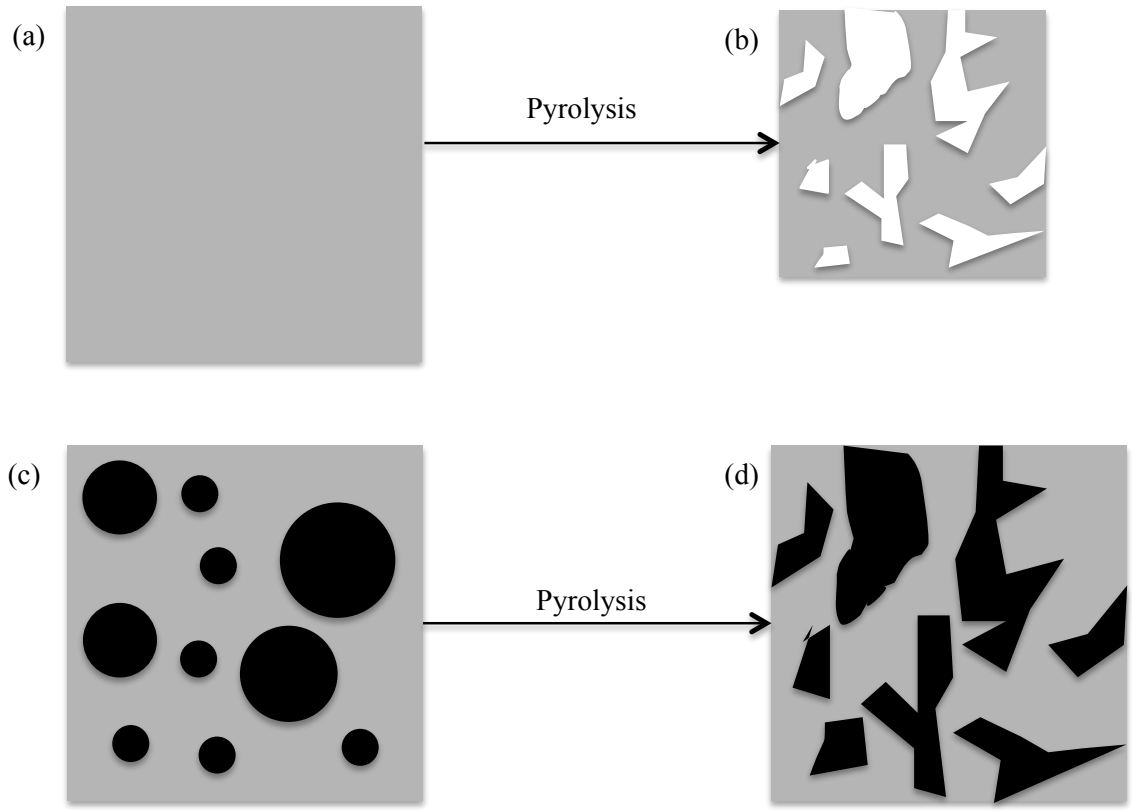

Figure 1: Effect of active fillers on the pyrolysis of PCPs, where (a) and (b) represent a PCP without any filler before and after pyrolysis, respectively and (c) and (d) represent a PCP with active filler before and after pyrolysis, respectively.

Another way to understand the impact of active fillers is to look at the chemical reactions that occur during pyrolysis with a PCP with and without the addition of active filler. Without the addition of active filler to the PCP, the PCP goes through the following chemical reaction as a result of pyrolysis:

$$P(s,l) \rightarrow C(s) + G(g) \quad (1)$$

Here, P represents the PCP, C represents the produced condensed ceramic, and G represents the gaseous reaction products.[72] When active filler is added to the PCP, the reaction experienced by the mixture during pyrolysis is as follows:

$$P(s,l) + T(s) \rightarrow K(s) + M(s) + G(g) \quad (2)$$

Here, the active filler phase (T) is able to react with the solid (K) or gaseous (G) decomposition products of the PCP in order to create a new solid phase (M) into the final ceramic.[72] If the specific volume of this new solid phase (M) is larger than the sum of the corresponding volumes of the active filler phase (T) and the solid decomposition product (K), then the solid phase (M) serves to counteract the shrinkage associated with the pyrolysis of the PCP in order to produce a near-net-shape ceramic.[76]

In order to maximize the benefits of using PCPs with active fillers to make ceramic parts, the filler material needs to be well-dispersed within the PCP to avoid pore formation in the ceramic phase. Researchers have shown that a general procedure can be employed to achieve this.[69] PCP dissolved in a suitable solvent, such as isopropyl alcohol[80] or acetone[70, 81] is combined with filler. To homogeneously disperse the filler particles within the solution, the mixture is magnetically stirred and ultrasonicated. The solvent evaporates and shaping methods are applied in order to get the part ready for pyrolysis. Once the part has been shaped, it is pyrolyzed into the desired ceramic.

Another reason why PCPs are good for ceramic fabrication is that they are usually dissolvable in organic solvents, which allows nano-sized fillers to be homogeneously dispersed. Side groups of PCPs such as –OH also make them attractive for ceramic fabrication; the reason being that these side groups easily react to the active metal filler particles, thus leading to the formation of metal-modified polymers.[69]

With using PCPs for ceramic part fabrication, research has indicated that there are still a lot of things that need to be improved in the manufacturing process in order for the ability to make parts for high-temperature and functional applications to come to fruition.

First of all, the processing environment plays a very significant role in the production of these parts. This makes replication of parts very difficult, which means products need to be made very carefully, being sure to keep the processing environment in mind. Also, bi-phasic and metal-modified polymers could have lower flowability compared to their pure counterparts, which means that processing conditions as well as additives must be selected carefully.[69]

1.5 Proposed Method

In order to create complex geometric parts, a new additive manufacturing technique must be developed. The system proposed here uses active filler mixed with PCP as build material. This build material is deposited via droplet-on-demand (DOD) or FDM to form the first layer of the desired part onto a heating stage that pre-cures the material. Once the first layer has pre-cured, a second layer is deposited on top of the first using the same procedure. This process is repeated layer-by-layer until the desired part has been completely fabricated.

CHAPTER 2

ADDITIVE MANUFACTURING

2.1 Prototype System

A prototype system was developed for the proposed additive manufacturing method. The prototype system proposed is a 3D printing system that operates using G-Code. Two versions of the prototype system have been implemented to introduce multi-functionality. These two versions consist of a droplet-on-demand (DOD) approach and a fused deposition modeling (FDM) approach, respectively.

2.1.1 Droplet-On-Demand (DOD) Setup

A picture and schematic of the droplet-on-demand (DOD) setup is shown in Figure 2. The system consists of a 2D-stage, a heating stage with a Teflon-covered aluminum foil sheet, a z-stage, a metal syringe, a pressure controller, a probe sonicator, a control box, and a camera. The DOD system is able to fabricate parts by having the metal syringe deposit droplets of material onto the heating stage while the 2D-stage moves in a given pattern that is determined by the G-Code commands sent to the system.

The 2D-stage is a 2D-linear stage consisting of an x-stage and y-stage that can move in the x- and y-directions, respectively. The movements that the x- and y-stages make are controlled by attached stepper drives (Parker Hannifin Corp., Rohnert, CA, USA). Both stepper drives are set to 1000 steps/mm, which allows for movement in both directions to have 1 μm precision. Connected to the 2D-stage is the heating stage, which has a built-in heater that is used to pre-cure the build material shortly after it is deposited. This minimizes the flow of the build material once it is deposited so that fabricated parts

(a)

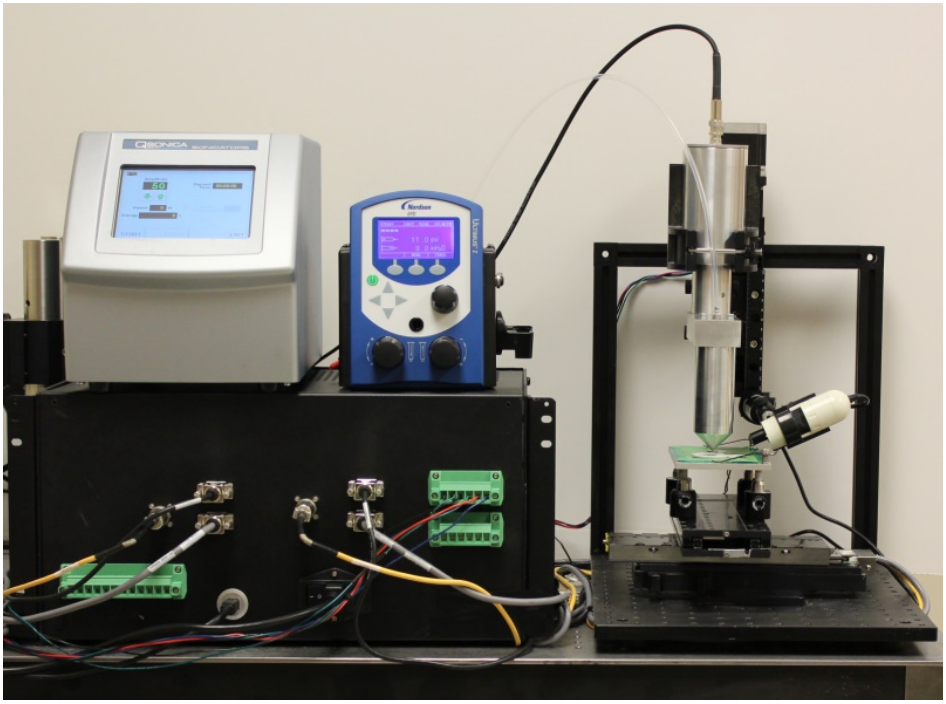

(b)

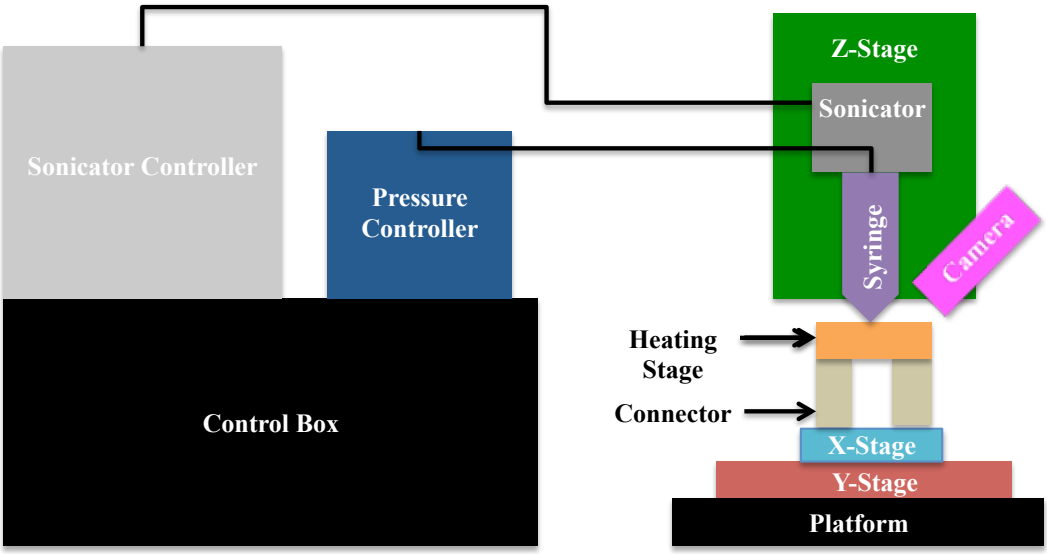

Figure 2: An actual (a) and schematic (b) representation of the droplet-on-demand (DOD) setup of the prototype system.

can better maintain their desired geometry. A Teflon-covered aluminum foil sheet (3M, Maplewood, MN, USA) is taped to the surface of the heating stage with heat-resistant tape. This sheet allows for easy removal of parts from the system since the Teflon creates a non-stick surface for build material to be deposited on. Therefore, when parts have been completely pre-cured, one can easily remove parts from the heating stage by hand.

The metal syringe is what dispenses the build material. The top part of the syringe resembles a hollow cylinder. This is the part of the syringe that stores the build material while the prototype system is in operation. As seen in Figure 2, the syringe eventually tapers off to a point. At the end of this point, there is a 0.203 mm-diameter hole where the build material eventually comes out. It should be noted that the size of the hole was chosen since it was the minimum size that allows for consistent material deposition during operation. Utilizing a minimally-sized hole minimizes the droplet size of the material, which improves the tolerance fabricated parts can achieve. This, in turn, minimizes pore formation and helps to maximize near-net-shape capabilities.

The metal syringe along with a video camera is attached to the z-stage. This allows for layer-by-layer deposition of the build material. By being connected to the z-stage, the metal syringe can be elevated by a distance equivalent to the layer thickness and material can be deposited directly on top of the previous layer. This also ensures that the final deposited part will have layers of equal thickness throughout. It is important to note that the reason a video camera is attached to the z-stage is that it enables video imaging of material deposition to be used for accurate measurement of the layer thickness. The movement of the z-stage is controlled by a microstep driver (Microstep Driver ST-M5045) that is set to 1008 steps/mm.

In order to dispense build material in a controlled manner, a pressure controller (Nordson EFD LLC, East Providence, RI, USA) is attached to the syringe via a plastic tube as shown in Figure 2(a). This provides the system with a controlled pressure input so that build material is deposited with equivalent droplet size throughout its entire operation. In order to obtain the desired droplet size, a pressure input is applied for a specified time interval. Additionally, a negative pressure is typically applied concurrently so as to eliminate excess dripping of the build material.

A probe sonicator (QSonica LLC, Newtown, CT, USA) is attached to the top of the metal syringe in the configuration shown in Figure 2. This allows for build material to be resonicated within the metal syringe during quick breaks in operation of the prototype system. This is a necessary step that is executed to keep good dispersion of the active filler particles within the build material. Without resonication from time to time during operation, particles will conglomerate and cause clogging of the nozzle, which requires an extended break in operation in order to fix. In order to ensure that the probe sonicator would be able to properly sonicate the solution, a finite-element analysis (FEA) analysis of the sonicator-syringe assembly was executed as seen in Figure 3(b). From Figure 3(b), it is evident that the entire assembly experiences some displacement during sonication. This corresponds to vibration of the entire assembly, even in the area around the hole at the bottom tip of the syringe where the majority of the build material is typically located during operation. This proves that sonication is able to vibrate the build material solution within the syringe, thus allowing there to always be a good dispersion of particles within the build solution during operation of the DOD setup. But, it should be noted that this resonication process comes with a consequence. Resonication makes the build material

solution prone to air bubble formation, which causing porosity within the final ceramic, thus causing it to lose its structural integrity.

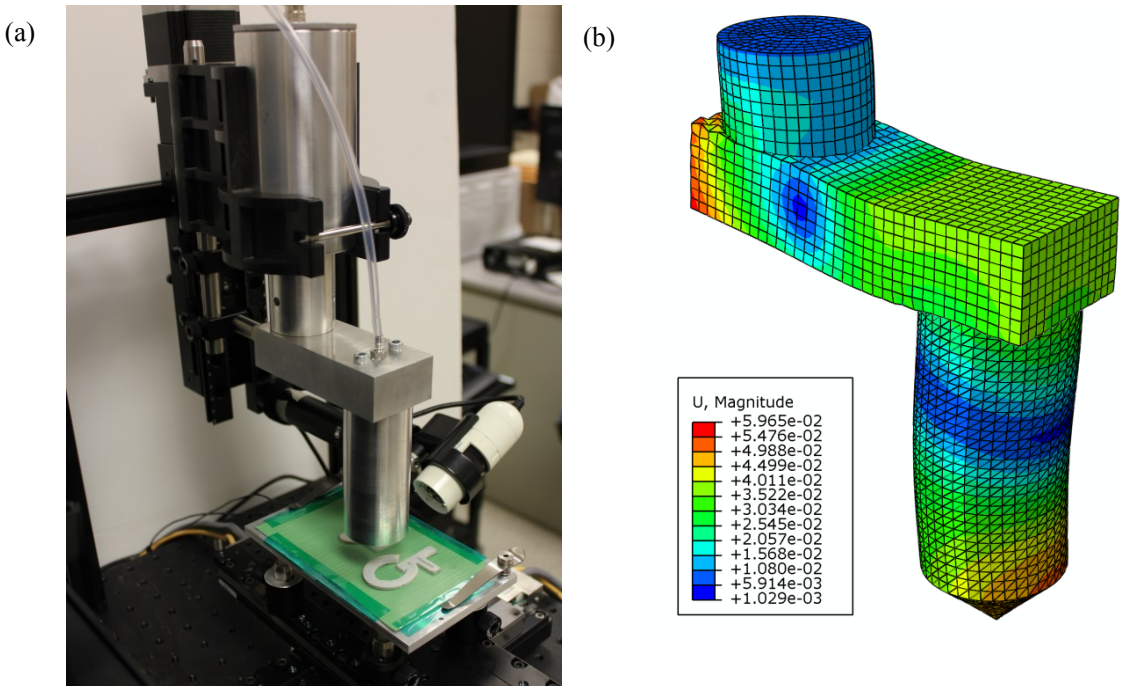

Figure 3: An actual (a) and FEA (b) representation of the syringe-sonicator assembly within the DOD setup.

An Arduino Uno board (Mouser Electronics Inc., Mansfield, TX, USA) is connected to the stepper drives that control the movement of each of the directional stages (x, y, and z). A GRBL program consisting of G-Code statements that instruct the 2D-linear stage and z-stage how to move has been uploaded to the Arduino board. The stepper drives are attached to the Arduino board so that they can receive the information from the sent G-Code statements and allow for desired movements to take place in all three directions. It is important to note that the pressure controller is also attached to the

Arduino board. This is to enable the prototype system to have G-Code controlled material deposition.

GRBL is an open-source software program that allows the prototype system to perform its desired functions using G-Code.[82] The original GRBL software only consisted of code designed for making the desired movements in the x-, y-, and z-directions. Therefore, code was added to create a new G-Code command that initiates DOD inkjet printing of the build material.

In order to make the system easy to use, the prototype system interacts with Universal G-Code Sender[83]; a graphical user interface (GUI) java program that is able to interpret the G-Code commands from GRBL and send them to the Arduino board via a Universal Serial Bus (USB) connection. With the Universal G-Code Sender, one can either write G-Code commands and send them line-by-line or can send an entire file of G-Code statements (Figure 4). To facilitate quick fabrication of parts, it is recommended that one sends a file of G-Code that when completely executed, will produce the entire part as opposed to sending line-by-line statements.

To write the file that consists of all the G-Code statements necessary to fabricate an entire part, a MatLab program can typically be used. When the program runs, a text file is generated with G-Code statements that when executed, will produce the desired part. This text file can then be uploaded and sent to the prototype system using Universal G-Code Sender.

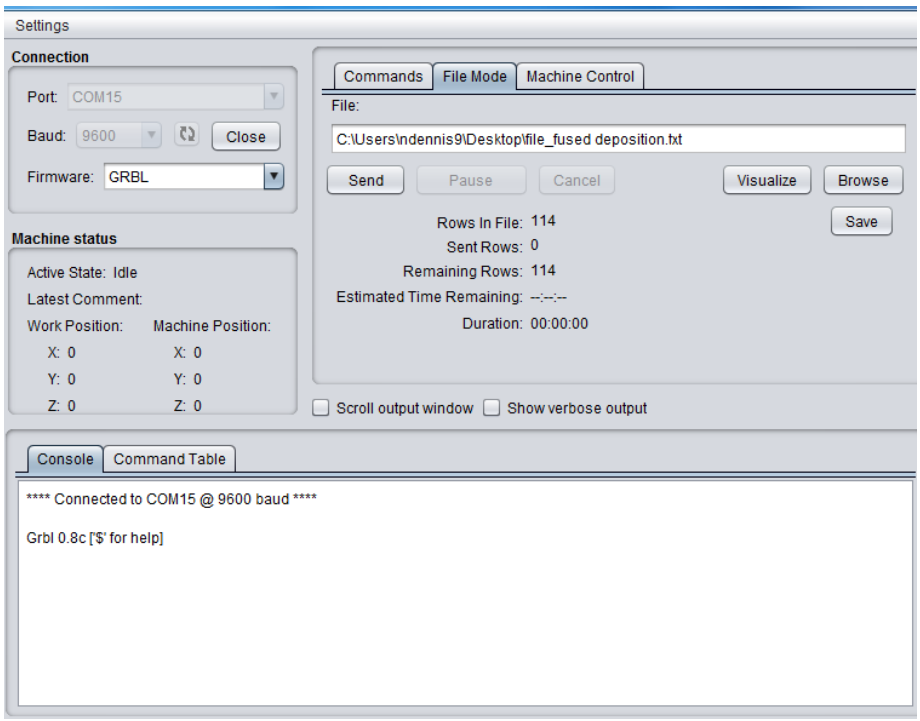

Figure 4: Representation of the Universal G-Code Sender GUI.

2.1.2 Fused Deposition Modeling (FDM) Setup

To deposit more viscous materials, the DOD technique becomes futile because the pressure that is required to force each droplet out of the syringe is too high for the prototype system to handle. Therefore, fused deposition modeling (FDM) was integrated into the prototype system. Figure 5 represents an actual and schematic representation of the FDM setup. A comparison of the DOD and FDM setups only shows a few differences. The main difference is that the sonicator-syringe assembly has been replaced with a plastic syringe with a detachable nozzle that is connected to the pressure controller via a plastic tube.

(a)

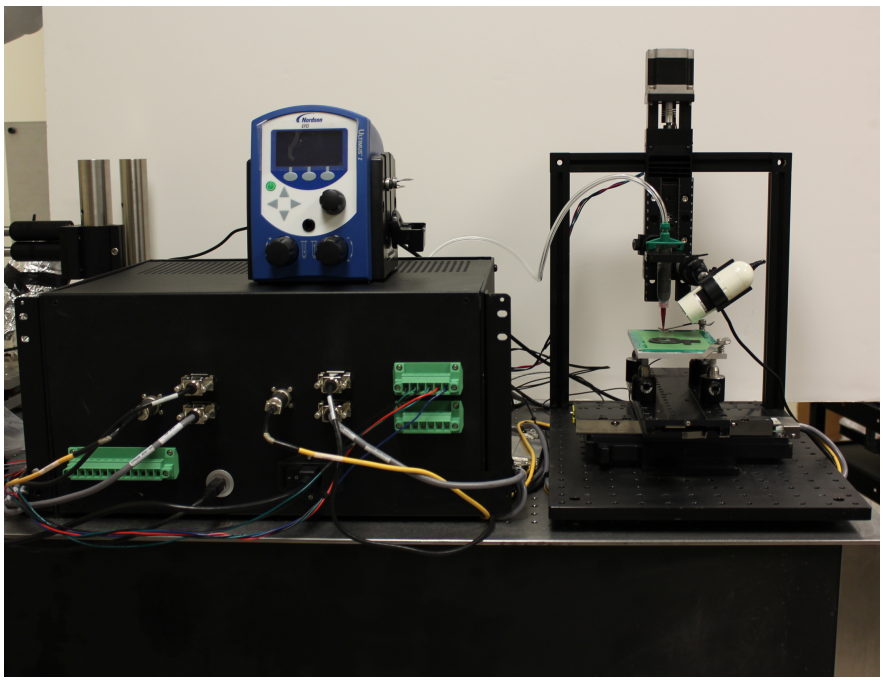

(b)

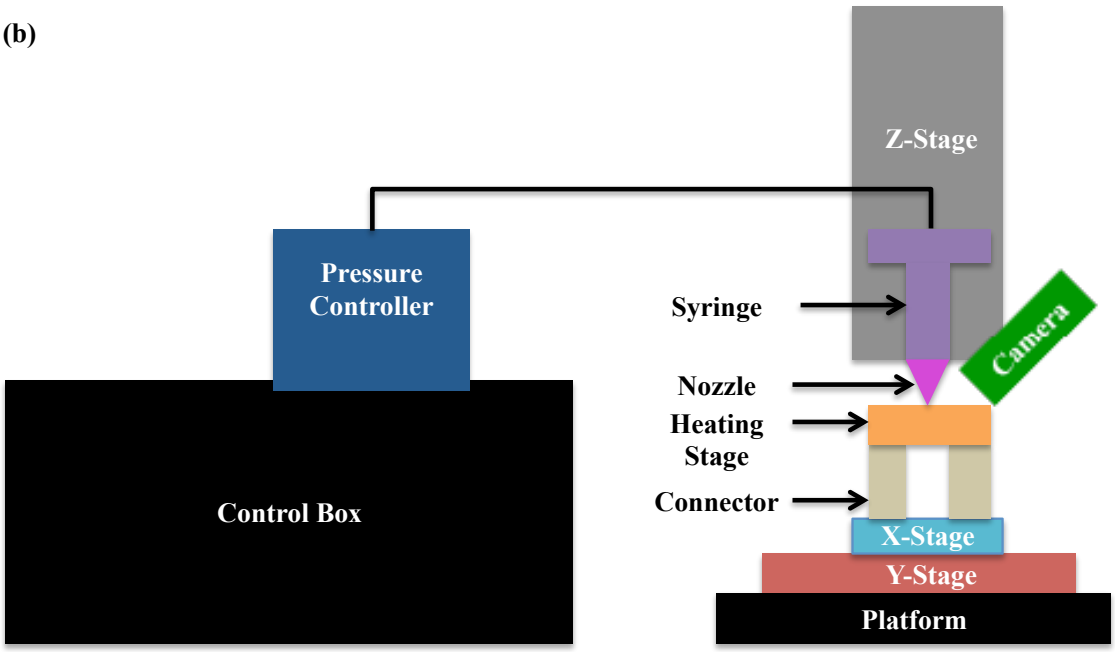

Figure 5: An actual (a) and schematic (b) representation of the fused deposition modeling (FDM) setup of the prototype system.

Another change from the DOD setup that is required to make when transitioning to the FDM setup is giving the system a constant flow of pressure input as opposed to a pressure input that is limited by the droplet deposition time, which can be done by enabling the steady mode function of the pressure controller. With a constant flow of input pressure, the system deposits a smooth stream of build material with an associated line width that is determined by the nozzle size. This makes having a detachable nozzle beneficial because it allows the user to change the line width by just replacing the nozzle. Since the line width is also directly correlated to tolerance, the user has the ability to control the tolerance of fabricated parts, which could prove useful for many applications.

As with the DOD setup, the heating stage is moved as build material is deposited to create the desired geometry and parts are fabricated in a layer-by-layer process. To control when material is deposited, the G-Code commands E (for enable) and C (for close) were created and added to the GRBL source code. When the E command is called, the pressure input is enabled and the system experiences a constant flow of pressure until the C command is called, which closes off the pressure input from the rest of the system, cutting off the flow of pressure to the syringe. The benefit of adding these two commands is that the prototype system consists of an on-off switch that controls the pressure input to the system, ensuring the material is only deposited when desired.

2.2 Build Material Development

The build material for our system consisted of a liquid PCP, active filler, and catalyst. The PCP used was the polycarbosiloxane CSO^{TM}116 (EEMS®, Saratoga Springs, NY, USA), the active filler used was titanium diboride (TiB_2) microparticles

(Sigma Aldrich Inc, St. Louis, MO, USA), and the catalyst solution used was CLC-PB055 (EEMS®, Saratoga Springs, NY, USA). It is important to note that TiB_2 was chosen as the active filler because research shows it experiences a large expansion during pyrolysis within the heating atmosphere used in the present work compared to that of other active fillers.[76] This will serve to minimize the volume fraction of TiB_2 that is necessary to produce parts that experience zero shrinkage during pyrolysis. This is important because if the volume fraction of active filler is too high, enhanced porosity will take effect and the final ceramic will start to lose its structural integrity.[75] Also, the addition of the catalyst solution was used to expedite the curing of the PCP, allowing it to pre-cure at only a temperature range of 80 – 100 °C.

2.2.1 Build Material Chemistry

To determine the concentration ratio between the TiB_2 active filler and the liquid PCP the following relationship was used:

$$\Psi_{total} = \left(1 - V_f / V_f^{\max}\right)\left(\Psi_{poly} - 1\right) + V_f\left(\Psi_f - 1\right) \tag{3}$$

Here, Ψ_{total} is the total volume change from pyrolysis, V_f is the volume fraction of active filler in the starting polymer-filler mixture, V_f^{max} is the maximum packing density of active filler powder, Ψ_{poly} is the specific volume change of the PCP caused by pyrolysis, and Ψ_f is the specific volume change of the active filler phase caused by pyrolysis.[75] To determine the amount of active filler to use in order to achieve zero shrinkage, Ψ_{total} is set to zero and equation (3) is rearranged to solve for V_f as shown by the equation,

$$V_f = \frac{\Psi_{poly} - 1}{\frac{\Psi_{poly} - 1}{V_f^{\max}} - \left(\Psi_f - 1\right)} \tag{4}$$

Before one can obtain a value for V_f in equation (4), values for V_f^{max}, Ψ_{poly}, and Ψ_f must be determined. Assuming that the TiB_2 filler particles are spherical and have the closest packing within the starting PCP solution, V_f^{max} has a value of 0.74.[76] Ψ_{poly} can be determined using the relationship,

$$\Psi_{poly} = \alpha\beta \tag{5}$$

where α represents the ceramic yield of the PCP and β represents the density ratio of the PCP in its polymeric state to that in its ceramic state.[76] For the liquid PCP, it is known that the ceramic yield α is 84%. It was assumed that the liquid PCP has a polymeric density of 1 g/cm^3 and a density of 2.65 g/cm^3 as a ceramic. This gives a β value of 0.377, which in turn, gives Ψ_{poly} a value of 0.317. Ψ_f can be determined using the relationship,

$$\Psi_f = \alpha_{TM}\beta_{TM} \tag{6}$$

where α_{TM} is the weight change of the active filler phase during pyrolysis and β_{TM} is the density ratio of active filler to filler reaction product.[76] From a table of values of $\alpha_{TM}\beta_{TM}$ for different active fillers shown by Greil[76], it is given that $\alpha_{TM}\beta_{TM}$ is 2.14 when the active filler is TiB_2 and pyrolysis takes place in an nitrogen (N_2) atmosphere. By plugging in the values of V_f^{max}, Ψ_{poly}, and Ψ_f into equation (4), the appropriate volume fraction V_f of TiB_2 within the starting polymer-filler solution becomes 0.331. To determine the weight percentage (wt%) of active filler within the solution, the equation,

$$W_f = \frac{V_f\rho_f}{V_f\rho_f + (1 - V_f)\rho_p} \tag{7}$$

was used. Here, W_f represents the weight percentage of active filler within the starting solution, ρ_f represents the density of the active filler, and ρ_p represents the density of the

PCP. Since the density of TiB_2 is 4.52 g/cm^3, W_f ends up being 0.691. Knowing the weight percentage of TiB_2 within the starting polymer-filler mixture, the equation,

$$Ratio = \frac{W_f}{1 - W_f} \tag{8}$$

can be used to obtain the ratio of TiB_2 to liquid PCP in the solution. By plugging in 0.691 for W_f, one obtains that the starting polymer-filler solution should have an active filler-to-PCP weight ratio of 2.236:1.

2.2.2 Build Material Production

2.2.2.1 Samples Fabricated Using the DOD Setup

In order to create the build material solution to be used within the DOD setup, the following procedure was executed. First, 22.36 g of TiB_2 microparticles were added to 10 g of liquid PCP and were mixed with a wooden stick for a few minutes. Then, the solution was sonicated for 6 minutes with a power of 11 – 12 W using a probe sonicator (QSonica LLC, Newtown, CT, USA) to ensure good dispersion of the TiB_2 microparticles within the mixture. After the solution was sonicated, 0.100 g of catalyst (equivalent to 1wt% of the PCP) was added to the mixture to facilitate pre-curing of the build material once it is deposited onto the heating stage.

2.2.2.2 Samples Fabricated Using the FDM Setup

Reducing the active filler particle size is highly attractive because a smaller particle size increases the viscosity of the material. With increased viscosity, the flow of the build material solution is reduced and use of the DOD setup is no longer viable. Therefore, the FDM setup must now be used in order to fabricate parts. The reduction in

flow is beneficial because it improves the tolerance of fabricated parts as well as increases their formability. This means it is expected that samples will better maintain their desired geometry throughout the entirety of the fabrication process than do the samples made with the DOD setup, which use a build material solution that has larger particle size and is therefore less viscous when in solution. Thus, the route of using smaller-sized TiB_2 particles was pursued. Since build material production is difficult using smaller-sized TiB_2 particles directly, the build material solution is ball-milled in order to break up the microparticles into smaller sizes. An additional benefit of ball milling is that as the filler particles are broken up, they are being well dispersed, which makes probe sonication obsolete with this variation of the build material. This allows for the following procedure to be executed.

In order to increase the viscosity to a point at which the build material was suitable for FDM, the build material solution was ball-milled for 4 hours. One drawback of ball milling for several hours is that if the concentration of liquid PCP is the same as it was for the build material used in the DOD setup, the build material will dry out during ball milling, therefore prohibiting the use of FDM. This meant that the concentration of liquid PCP was increased to ensure that the solution would not dry out during the ball milling process. This variant of the build material consisted of 12 g of PCP as opposed to the 10 g that were used in the DOD setup. The amount of TiB_2 particles added to the solution remained at 22.36 g and the amount of catalyst added stays at a concentration of 1wt% of the PCP (0.120 g). This results in a TiB_2 volume fraction of 0.292. It should be noted here that the volume fraction was determined only considering the PCP and the TiB_2 particles. Since the concentration of catalyst within the overall solution is very small

(< 1wt%), the error in the value of volume fraction of TiB_2 is negligible. This applies to all variants of the build material solution unless otherwise stated. Ball milling took place within a Zirconium (Zr) container using Zr balls. After the solution was ball-milled, it was put into a vacuum chamber for approximately 30 minutes. This degasses the build material to get rid of any air bubbles that might exist within the solution. All other parts of the procedure to produce the build material solution are consistent with the procedure used for the DOD setup.

Another variant of build material solution consisted of 18 g of PCP, 22.36 g of TiB_2, and 0.180g of catalyst, which corresponds to a TiB_2 volume fraction of 0.216. The solution was ball-milled for 12 hours. All other parts of the procedure required to make the build material are consistent with that of the solution made with a TiB_2 volume fraction of 0.292.

An additional variant of the build material solution consisted of 7 g of PCP, 22.36 g of TiB_2, and 0.070g of catalyst, which corresponds to a TiB_2 volume fraction of 0.414. The solution was ball-milled for 45 minutes. All other parts of the procedure required to make the build material are consistent with that of the solutions made with a TiB_2 volume fraction of 0.216 and 0.292.

2.3 Fabrication Technique

2.3.1 Green Part Fabrication

Once one layer of the build material has been deposited and fully pre-cured, the dispensing syringe is elevated a distance equivalent to the layer thickness and a second layer is deposited on top of the first. This layer-by-layer process is repeated until the

complete desired part has been fabricated. Once the top layer has pre-cured, the part is carefully removed from the stage by hand.

2.3.2 Ceramic Fabrication

To perform pyrolysis, the part is heated and then cooled within a Nitrogen (N_2) atmosphere within a kiln (Clay-King, Spartanburg, SC, USA) using the temperature-time curve shown in Figure 6. It is important to note some key observations associated with Figure 6. First, the part is heated at a rate of 600 °C/hr until the temperature of the kiln reaches 300 °C. The kiln is held at this temperature for 30 minutes. After this step, the kiln heats up again at a rate of 600 °C/hr until the temperature reaches 1100 °C, where it is held at this temperature for 1 hour. Then, the kiln cools down to 300 °C at a rate of 600 °C/hr, where it is held at that temperature for 10 minutes. Then, the N_2 gas is turned off and the kiln is cooled down at a programmed rate of 600 °C/hr until it reaches a temperature of 50 °C.

The reason the maximum temperature that the kiln reaches was chosen to be 1100 °C is that a maximum temperature of 1100 °C ensures that fabricated parts will fully go through the polymeric-to-ceramic conversion process. The reason that the kiln is first held at 300 °C during the heating process is that heating the part at this temperature for an extended period of time will allow the part to "Hard Cure" before it goes through the polymeric-to-ceramic conversion. This minimizes shrinkage within the part during pyrolysis. The heating rate being always 600 °C/hr came from what was suggested by Bernardo et. al[84]. The cooling part of the temperature-time curve was chosen so as to mirror the heating part.

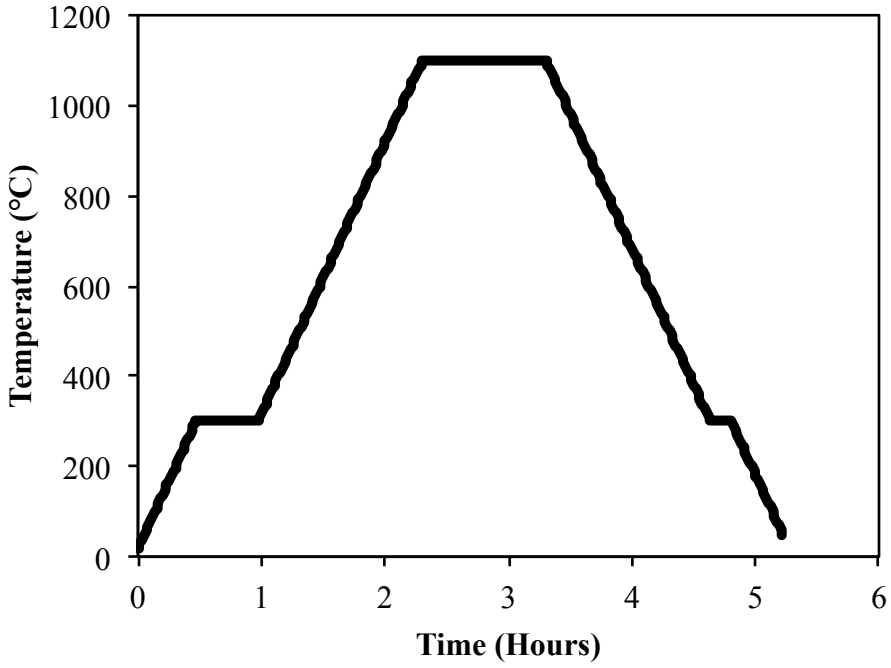

Figure 6: Plot of the Temperature-Time Curve that was executed during pyrolysis.

CHAPTER 3

MICROSTRUCTURE AND MECHANICAL PROPERTY CHARACTERIZATIONS

3.1 Near-Net-Shape Characterization

3.1.1 Samples Having a TiB_2 Volume Fraction of 0.331

Using the DOD setup, four rectangular samples were fabricated using the build material solution with a TiB_2 volume fraction of 0.331. The following parameters were used when fabricating these samples: a droplet size of 2 mm, a droplet time of 4.0 ms, an input pressure of 49.0 psi, and a negative pressure of 4.9 in H_2O. Each sample was made with a desired geometry of 11.000 mm x 17.000 mm. Samples were pyrolyzed in the kiln using the temperature-time curve shown in Figure 6.

Figure 7(a) and Figure 7(b) represent images of the fabricated samples that were taken before and after pyrolysis, respectively. From Figure 7(a), one can see that the samples printed using this build material solution are not very rectangular before pyrolysis, with material expanding outside of the rectangular region of the sample. This can be attributed to the flow of the solution being too high, which causes droplets to expand once they are printed. This causes the fabricated parts to deviate away from the desired geometry.

The length and width before and after pyrolysis for each sample was measured and is presented in Table 1 along with the percent shrinkage in length and width experience by each sample during pyrolysis.

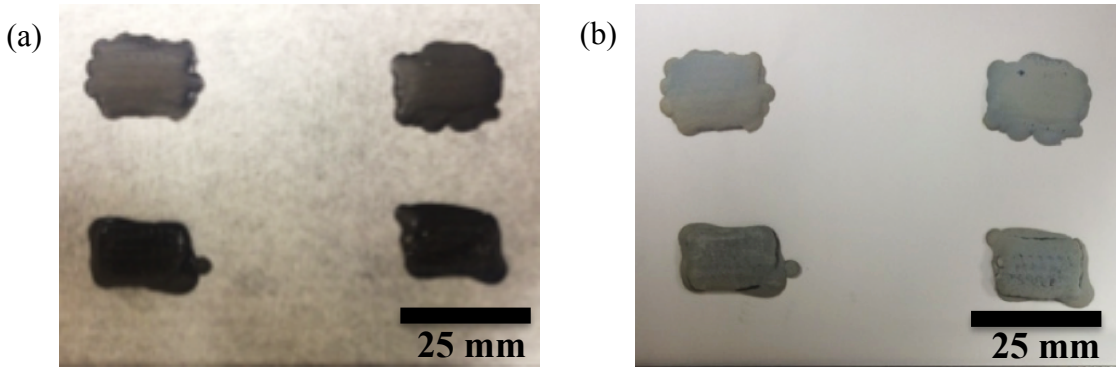

Figure 7: Pictures of samples fabricated using a build material solution that has a TiB_2 volume fraction of 0.331 taken (a) before and (b) after pyrolysis.

For each sample, the percent shrinkage in length and width were averaged together to obtain an average linear shrinkage. By knowing the average linear shrinkage, one can obtain an estimate of the volume shrinkage by using the equation,

$$\varepsilon_V = \left(1+\varepsilon_L\right)^3 - 1 \tag{9}$$

where ε_V represents the volume shrinkage and ε_L represents the linear shrinkage. For ε_L<<1, equation (9) can be reduced to the following:

$$\varepsilon_V = 1 + 3\varepsilon_L - 1 = 3\varepsilon_L \tag{10}$$

By allowing the average linear shrinkage to be ε_L, the volume shrinkage ε_V for each sample can be calculated. Once the volume shrinkage for each sample was calculated, the values determined were averaged to obtain the average volume shrinkage for the entire set. This average volume shrinkage was 6.51 ± 3.24%. It should be noted here that unless otherwise stated, the average volume shrinkage was calculated using this procedure. This result shows that although zero volume shrinkage is not quite achieved, the addition of active fillers into the starting PCP matrix has enabled these parts to experience significantly reduced volume shrinkage during pyrolysis, to the point where these parts

essentially achieve near-net-shape capability. This reduction in volume shrinkage can only benefit this material system as it improves the final ceramic's mechanical properties.

To compare the desired geometry to the measured length and width after pyrolysis the percent error equation,

$$\%error = \frac{|Theoretical - Experimental|}{Theoretical} \times 100 \tag{11}$$

where Theoretical is the desired value and Experimental is the measured value, was used. The percent error in length and width for each sample is shown in Table 1. For each sample, the percent error in length and width were averaged together to obtain the average linear dimensional error. The value for average linear dimensional error for each sample was averaged together to obtain the average linear error for the entire set. This error ended up being 29.12 ± 11.03%. It should be noted here that unless otherwise stated, the average linear error is calculated in this way.

Table 1: Dimensional Measurements of Samples Before and After Pyrolysis With A TiB_2 Volume Fraction of 0.331

Dimension ID	Pre-Pyrolyzed Sample (mm)	Pyrolyzed Sample (mm)	Percent Shrinkage (%)	Percent Error After Pyrolysis (%)
Sample 1 Width	22.76	22.28	2.13	31.05
Sample 1 Length	16.18	16.16	0.17	46.88
Sample 2 Width	21.97	21.26	3.25	25.05
Sample 2 Length	16.58	16.67	-0.53	51.52
Sample 3 Width	20.66	20.24	2.03	19.05
Sample 3 Length	13.55	12.93	4.63	17.50
Sample 4 Width	19.74	19.05	3.49	12.04
Sample 4 Length	14.61	14.29	2.19	29.87

3.1.2 Samples With a TiB_2 Volume Fraction of 0.292

Using the FDM setup, four rectangular samples were fabricated using the build material solution that had a TiB_2 volume fraction of 0.292. The following parameters were used when fabricating these samples: a line width of 0.75 mm, an input pressure of 58.0 psi, a negative pressure of 9.4 in H_2O, and a nozzle diameter of 0.406 mm. Each sample had a desired geometry of 11.625 mm x 15.375 mm. Samples were pyrolyzed in the kiln using the temperature-time curve shown in Figure 6.

Figure 8 represents pictures of the samples taken before and after pyrolysis. An observation of Figure 8 shows that these samples have the desired rectangular shape. Also, it is evident that samples 1 and 3 have each developed a large bubble. This is probably due to the presence of air bubbles within the build material, which means that the solution should have been kept in vacuum for longer than 30 minutes to ensure that absolutely no air bubbles were present.

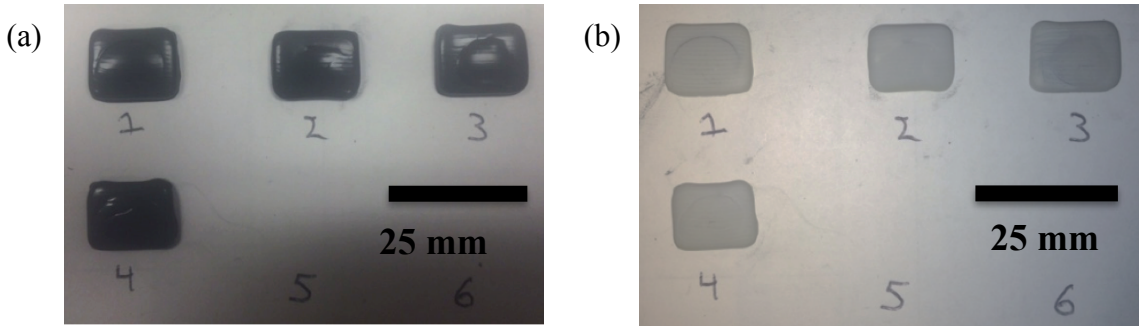

Figure 8: Pictures of samples fabricated using a build material solution that has a TiB_2 volume fraction of 0.292 taken (a) before and (b) after pyrolysis.

The length and width of each sample before and after pyrolysis were measured and are presented in Table 2 along with the percent shrinkage and percent error in length

and width for each sample. Using this data, it was determined that the average volume shrinkage and average linear dimensional error for the entire set were 24.39 ± 3.48% and 3.94 ± 2.17%, respectively.

Table 2: Dimensional Measurements of Samples Before and After Pyrolysis With A TiB_2 Volume Fraction of 0.292

Dimension ID	Pre-Pyrolyzed Sample (mm)	Pyrolyzed Sample (mm)	Percent Shrinkage (%)	Percent Error After Pyrolysis (%)
Sample 1 Width	17.17	15.57	9.31	1.25
Sample 1 Length	13.80	12.88	6.71	10.76
Sample 2 Width	16.59	15.33	7.55	0.27
Sample 2 Length	12.87	11.94	7.26	2.70
Sample 3 Width	17.51	16.04	8.44	4.30
Sample 3 Length	13.22	12.41	6.16	6.73
Sample 4 Width	16.35	14.63	10.53	4.84
Sample 4 Length	12.87	11.71	9.08	0.69

3.1.3 Samples With a TiB_2 Volume Fraction of 0.216

Once the build material solution was prepared, three rectangular samples were fabricated using the FDM setup. Each sample was designed with the following parameters: a line width of 0.75 mm, a desired geometry of 11.625 mm x 15.375 mm, an input pressure of 23.5 psi, a negative pressure of 33.0 in H_2O, and a nozzle diameter of 150 μm. The samples were pyrolyzed in the kiln using the temperature-time profile presented in Figure 6.

To measure the amount of shrinkage these samples experienced during pyrolysis, images of the samples were taken before and after pyrolysis as shown in Figure 9. An observation of Figure 9(b) indicates that although these samples maintained the desired rectangular shape, there is the presence of cracks. This is due to the decrease in the

volume fraction of TiB_2 within the starting solution (0.216 compared to 0.292 and 0.331), which corresponds to an increased concentration of PCP. As the concentration of the PCP in the starting solution is increased, so too does the shrinkage that the samples will experience during pyrolysis. This, in turn, increases the amount of residual stress within the samples during pyrolysis, which when increased to a certain point, will cause cracking to occur. The presence of cracks is certainly a drawback in this scenario because it lowers the structural integrity of the pyrolyzed samples, making them prone to brittle failure.

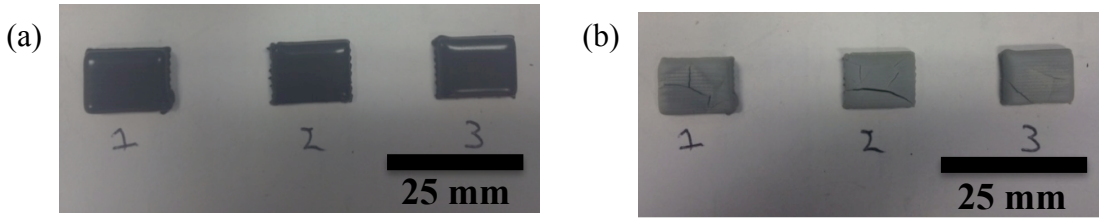

Figure 9: Pictures of samples fabricated using a build material solution that has a TiB_2 volume fraction of 0.216 taken (a) before and (b) after pyrolysis.

The length and width measured for each sample along with the associated shrinkage and error experienced during pyrolysis for each measurement are presented in Table 3. Using this data, it was determined that the average volume shrinkage and average linear dimensional error for the entire set were 34.99 ± 4.22% and 8.74 ± 3.45%, respectively.

Table 3: Dimensional Measurements of Samples Before and After Pyrolysis With A TiB_2 Volume Fraction of 0.216

Dimension ID	Pre-Pyrolyzed Sample (mm)	Pyrolyzed Sample (mm)	Percent Yield (%)	Percent Error After Pyrolysis (%)
Sample 1 Width	16.58	14.59	12.01	5.12
Sample 1 Length	12.12	10.91	9.91	6.11
Sample 2 Width	16.05	14.08	12.28	8.44
Sample 2 Length	11.80	10.71	9.20	7.86
Sample 3 Width	15.73	13.57	13.74	11.76
Sample 3 Length	11.58	10.10	12.82	13.13

3.1.4 Samples With a TiB_2 Volume Fraction of 0.414

Three rectangular samples with a TiB_2 volume fraction of 0.414 were fabricated using the FDM setup with the following parameters: a line width of 0.75mm, a desired geometry of 11.625 mm x 15.375 mm, a nozzle diameter of 0.254 mm, an input pressure of 11 – 12 psi, and no negative pressure. The samples were pyrolyzed in the kiln using the temperature-time profile presented in Figure 6.

To measure the amount of shrinkage these samples experienced during pyrolysis, images of the samples were taken before and after pyrolysis as shown in Figure 10. An observation of Figure 10 indicates that for the most part, the samples tend to keep their desired rectangular shape throughout pyrolysis. Also, it evident that bubbles have formed on the surface of some of these samples. This is caused by air bubbles within the build solution, which can be avoided by using a longer degassing time than what was used in the production of this variant of the build material.

(a) (b)

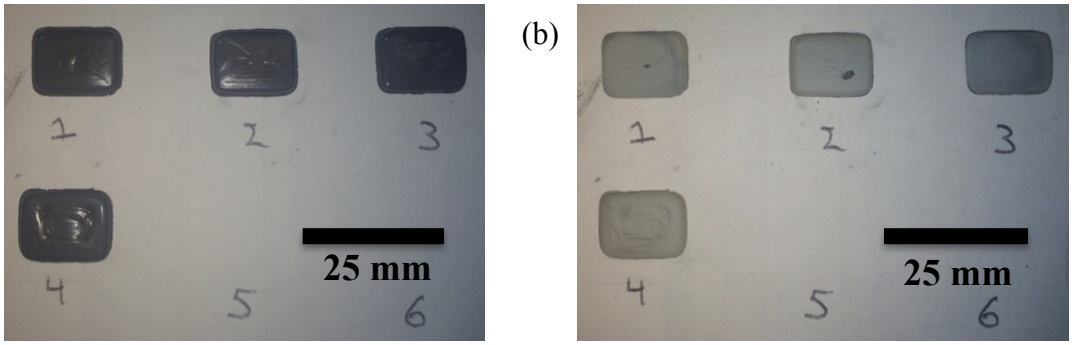

Figure 10: Pictures of samples fabricated using a build material solution that has a TiB_2 volume fraction of 0.414 taken (a) before and (b) after pyrolysis.

The length and width measured for each sample along with the associated shrinkage and error experienced during pyrolysis for each measurement are presented in Table 4. Using this data, it was determined that the average volume shrinkage and average linear dimensional error for the entire set were 16.07 ± 2.65% and 2.21 ± 1.11%, respectively.

Table 4: Dimensional Measurements of Samples Before and After Pyrolysis With A TiB_2 Volume Fraction of 0.414

Dimension ID	Pre-Pyrolyzed Sample (mm)	Pyrolyzed Sample (mm)	Percent Shrinkage (%)	Percent Error After Pyrolysis (%)
Sample 1 Width	16.36	15.47	5.43	0.63
Sample 1 Length	12.47	11.86	4.89	2.04
Sample 2 Width	15.79	14.83	6.09	3.56
Sample 2 Length	12.13	11.48	5.38	1.29
Sample 3 Width	16.25	15.60	3.98	1.47
Sample 3 Length	12.01	11.48	4.48	1.29
Sample 4 Width	16.93	15.86	6.35	3.15
Sample 4 Length	12.93	12.12	6.26	4.26

3.1.5 Design Map for 3D Ceramic Printing

Using the information obtained from the pictures taken of the samples before and after pyrolysis, enough knowledge was gained to determine when each setup should be used. Factors that determine this are the particle size and volume fraction of TiB_2 within the starting solution. Figure 11 represents a plot that shows when the two setups should be used. From this plot, it is clear that neither setup should be used for fabricating parts if the volume fraction of TiB_2 is below 0.220. This is because with volume fractions below 0.220, the expansion of the TiB_2 particles is no longer enough to counteract the effects of the shrinkage associated with the PCP during pyrolysis. At volume fractions below this point, the amount of shrinkage experienced by parts during pyrolysis is enough to cause the residual stress within the part to become high enough to induce cracking as was seen with the samples that had a TiB_2 volume fraction of 0.216. Also, both setups will not work if the particle size is too high. As particle size increases, it becomes easier for particles to conglomerate. This causes clogging of the build material to occur, thus prohibiting material deposition in both setups.

As stated in chapter 2, particle size and viscosity are inversely proportional, that is, as the particle size increases, the viscosity of the build material decreases and vice versa. If the particle size keeps decreasing, the viscosity of the build material will be so high that the build material will become completely solid, which makes material deposition using either the DOD or FDM setup impossible. Additionally, as the volume fraction of TiB_2 increases, the solid portion of the build material also increases, which in turn, will increase the viscosity. These two behaviors are reflected in the plot shown in Figure 11.

From Figure 11, it is observed that if the build material has a low volume fraction of TiB_2 (still above 0.220) and large particle size, the build material will be fluid, which means that the DOD setup should be used. Then, as the particle size is decreased and/or the volume fraction is increased, the build material solution will become semi-solid, having a viscosity similar to that of most commercial creams. At this point, the DOD setup will no longer work and the FDM setup becomes the best option. But, if the particle size is further decreased and/or the volume fraction is further increased, the build material will become completely solid and neither setup will work anymore.

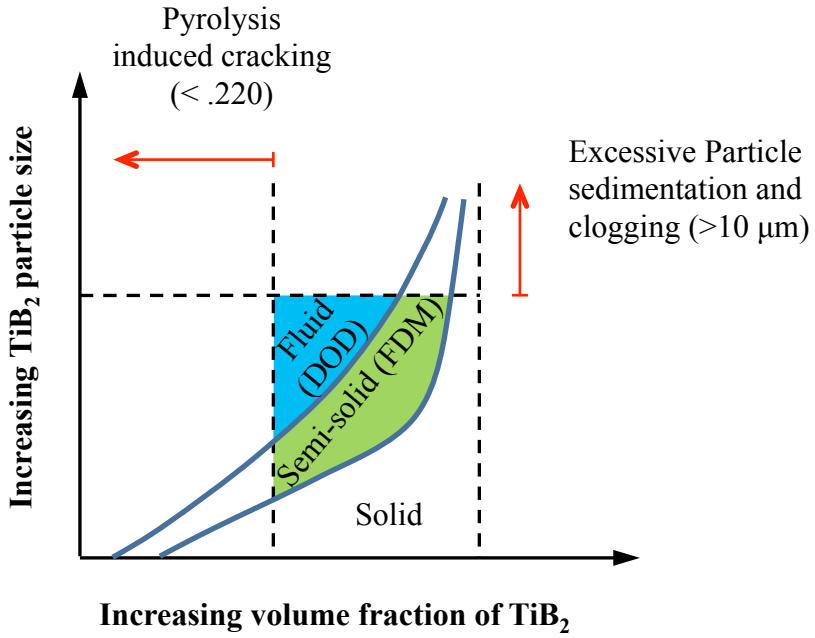

Figure 11: A design map for 3D printing of near-net-shape ceramic parts.

In addition to knowing when to use what setup, it is important to know that the prototype system is capable of producing parts with complex geometries. This is because for real-life applications, parts will need to be fabricated with complex geometries in order to properly serve their intended purpose. Therefore, two parts of complex

geometry, a heart and a simplified version of the Georgia Tech logo, were fabricated as shown in Figure 12. An observation of Figure 12 proves that the prototype system is capable of producing parts of complex geometries with desired shape as well as no visible cracks.

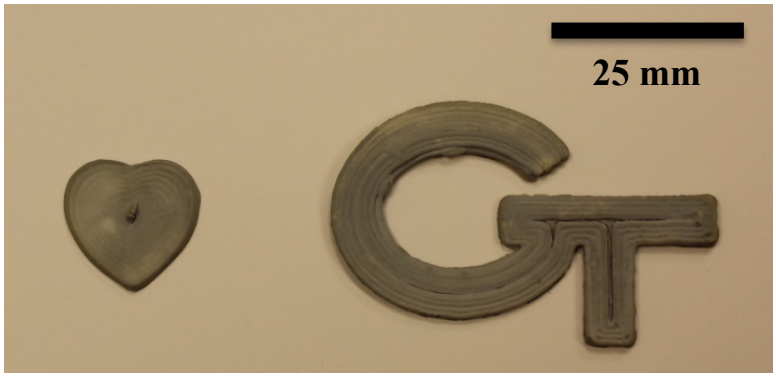

Figure 12: Images of fabricated ceramic parts made using complex geometries.

3.1.6 Volume Shrinkage Experienced during Pyrolysis

Using the volume shrinkage data, a plot was made of the average volume shrinkage as a function of the volume fraction of TiB_2 within the starting build material solution (Figure 13). From Figure 13, it is evident that as the volume fraction of TiB_2 increases from 0.216 to 0.331, the volume shrinkage experienced during pyrolysis decreases. This is expected behavior because the diminished presence of TiB_2 will not be enough to counteract the shrinkage inherent to the PCP during pyrolysis. Therefore, as the volume fraction of TiB_2 is decreased, the shrinkage associated with the PCP experiences less counteraction from the expansion of the TiB_2 particles during pyrolysis, thus causing the overall shrinkage to increase.

As the volume fraction of TiB_2 is further increased to 0.414, the volume shrinkage increases. This goes against the logic used previously as well as the equation used in order to determine the TiB_2 volume fraction that will experience theoretical zero volume shrinkage during pyrolysis (equation (3)). A reason for this behavior is that the samples made at this volume fraction could represent an outlier within the data set. In order to ensure that this is the case, samples should be made with volume fractions greater than 0.331 to see whether the volume shrinkage steadily increases to the value seen at a volume fraction of 0.414 or further decreases like it should.

Although the samples fabricated using a TiB_2 volume fraction of 0.292 and 0.331 experience an average volume shrinkage of 24.39 ± 3.48% and 34.99 ± 4.22%, respectively, which is a significant amount, the volume shrinkage experienced at these volume fractions is considerably less than it would be for a sample fabricated using a build material solution with no filler.

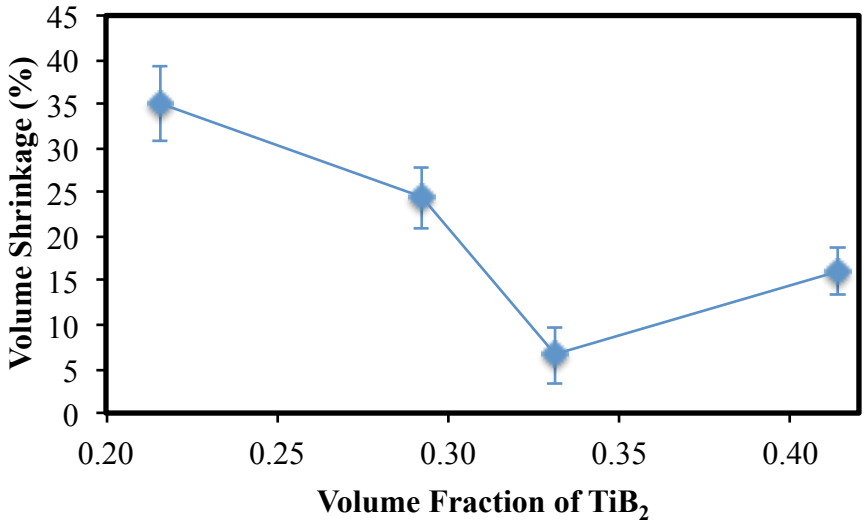

Figure 13: Plot of the average volume shrinkage experienced by the samples during pyrolysis as a function of the volume fraction of TiB_2 within the starting build material solution.

By setting the volume fraction V_f in equation (3) to zero, it is possible to determine the total volume change Ψ_{total} samples would experience if no filler had been added to the build material solution. This causes equation (3) to reduce to

$$\Psi_{total} = \Psi_{poly} - 1 \tag{12}$$

Using the fact that the PCP has a value of 0.317 for Ψ_{poly}, Ψ_{total} becomes -0.683, which corresponds to a volume shrinkage of 68.30%. This means that the samples fabricated using a TiB_2 volume fraction of 0.292 and 0.331 show an average reduction of 43.91% and 33.31% in the amount of volume shrinkage that occurs during pyrolysis, respectively as compared to the theoretical value of the volume shrinkage associated with pyrolysis of the PCP without the presence of filler material.

Additionally, compared to other recent work on the additive manufacturing of ceramics[85, 86], the samples here experience significantly less shrinkage during pyrolysis. In the work of Shahzad et al.[86], zirconia parts were fabricated using an indirect SLS approach. The linear shrinkage experienced by these parts after sintering was seen to be no lower than 30%, which if set to ε_L in equation (10), corresponds to a volume shrinkage of 90%. In the work of Gaytan et al.[85], which involves the fabrication of barium titanate using a binder jetting approach in conjunction with sintering, they were able to achieve samples with a linear shrinkage in the x-, y-, and z-directions of approximately 20 – 30% after sintering, which corresponds to a volume shrinkage of approximately 60 – 90%.

In both cases, the volume shrinkage experienced by the final ceramic is far greater than that experienced with any of the samples fabricated with the prototype system. This shows that the prototype system is capable of fabricating parts that better maintain their

desired geometry and have better near-net-shape capabilities than do similar recently developed additive manufacturing methods.

3.1.7 Dimensional Error

Figure 14 represents a plot of the average linear dimensional error as a function of the TiB_2 volume fraction within the starting build material solution. From the plot, it is clear that the samples that were made with a TiB_2 volume fraction of 0.331 have a significantly higher dimensional error than do the samples made with any of the other build material variants. This is as expected since this build material variant was the least viscous and the only one for which flow of the material was observed during printing. As material flows as it is deposited, it causes expansion of the part geometry, which will cause the part to deviate from its desired geometry. Therefore, it makes sense that samples that experience flow would end up having significantly higher dimensional error than did samples that did not experience flow. Another reason for this significant dimensional error has to do with the type of printing setup that was used to make these samples. The samples that have a TiB_2 volume fraction of 0.331 were fabricated using the DOD setup whereas the samples that have a TiB_2 volume fraction of 0.216, 0.292, and 0.414 were made using the FDM setup. Since the droplet size that can be achieved with the DOD setup (2 mm) is greater than the line width that can be achieved with the FDM setup (0.75 mm), samples made with the DOD setup will have a lower dimensional tolerance than do samples made with the FDM setup. By paying attention to just the data corresponding to the FDM setup (volume fractions of 0.216, 0.292, and 0.414) in Figure 14, one sees that as the volume fraction of TiB_2 is increased, the average linear dimensional error decreases. It is likely that this behavior is attributed to the viscosity of

the build material solution. As a solution becomes more viscous, it experiences less flow. This means that as the viscosity of the build material solution increases, the flow of the deposited build material should decrease and therefore, have a line width that approaches the desired 0.75 mm. This should cause the dimensional error within fabricated parts to decrease with increased build material viscosity. Since the PCP is liquid and the TiB_2 fillers are solid particles, the viscosity of the build material solution should increase as the volume fraction of TiB_2 increases. Therefore, parts fabricated with increased TiB_2 volume fraction should experience less dimensional error, which is expressed in Figure 14.

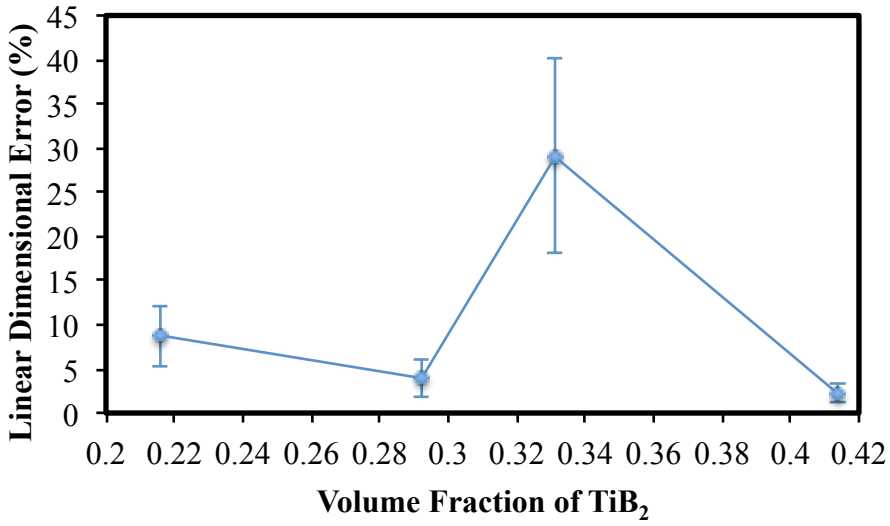

Figure 14: Plot of the average linear dimensional error experienced by the samples during pyrolysis as a function of the volume fraction of TiB_2 within the starting build material solution.

3.2 Microstructural Characterization

3.2.1 Samples Having a TiB_2 Volume Fraction of 0.331

In order to look at the microstructure of fabricated parts, scanning electron microscope (SEM) images were taken of fabricated pyrolyzed parts. Before taking SEM images, samples were cut using a diamond saw to expose the cross-section. The cross-section was polished to get a fine finish, making it clear to see the microstructure when samples were observed under the SEM. For the pyrolyzed samples, the cross-section was hand polished on a spinning plate using the following procedure. First, the samples were polished with 600 grit and 1200 grit sand paper. Then, polishing cloth in conjunction with 50-nm colloidal silica was used to polish the cross-section to a 50-nm finish.

3.2.1.1 SEM Imaging

An SEM image of the polished cross-section of a pyrolyzed part is presented in Figure 15. There are a couple of important observations can be taken away from this image. First of all, it is evident that no pores have developed, indicating that the final part is near-net-shaped. Secondly, it seems that the microstructure consists of inclusions within a matrix material.

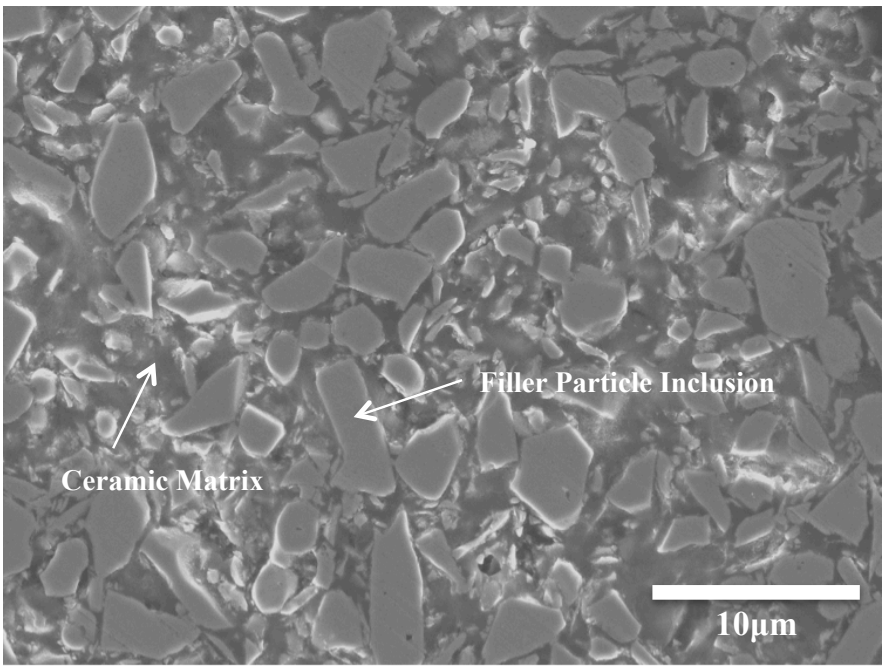

Figure 15: SEM image of a polished cross-section of a sample with a TiB_2 volume fraction of 0.331. The site shown here represents the location where the EDS analysis was executed.

3.2.1.2 EDS Analysis

In order to gain a sense of what reactions took place during pyrolysis, energy-dispersive x-ray spectroscopy (EDS) analyses were executed at different sites of pyrolyzed samples. The elements chosen for EDS anlyses were Ti, B, O, N, Si, and C for the following reasons. The elements Ti and B were chosen since those are the elements that make up the active filler microparticles. The elements Si, O, and C were chosen because the PCP is a polycarbosiloxane. Lastly, the element N was chosen because the samples were pyrolyzed in a N_2 atmosphere. Figure 15 represents a site used for EDS analysis and the resulting EDS mappings from that analysis for all six elements analyzed is shown in Figure 16. A comparison between Figure 15 and Figure 16 provides insight on the reactions that take place during pyrolysis. It is evident that the inclusions match up with the Ti, B, and N EDS mappings and that the matrix matches up with the Si, O, and C

EDS mappings. Therefore, the inclusions consist of material made up of the elements Ti, B, and N and the matrix material consists of Si, O, and C. This indicates that the TiB_2 microparticles successfully reacted with the N_2 atmosphere within the kiln and have expanded in order to counteract the shrinkage and pore formation that is associated with the pyrolyzation of PCPs without the presence of active fillers.

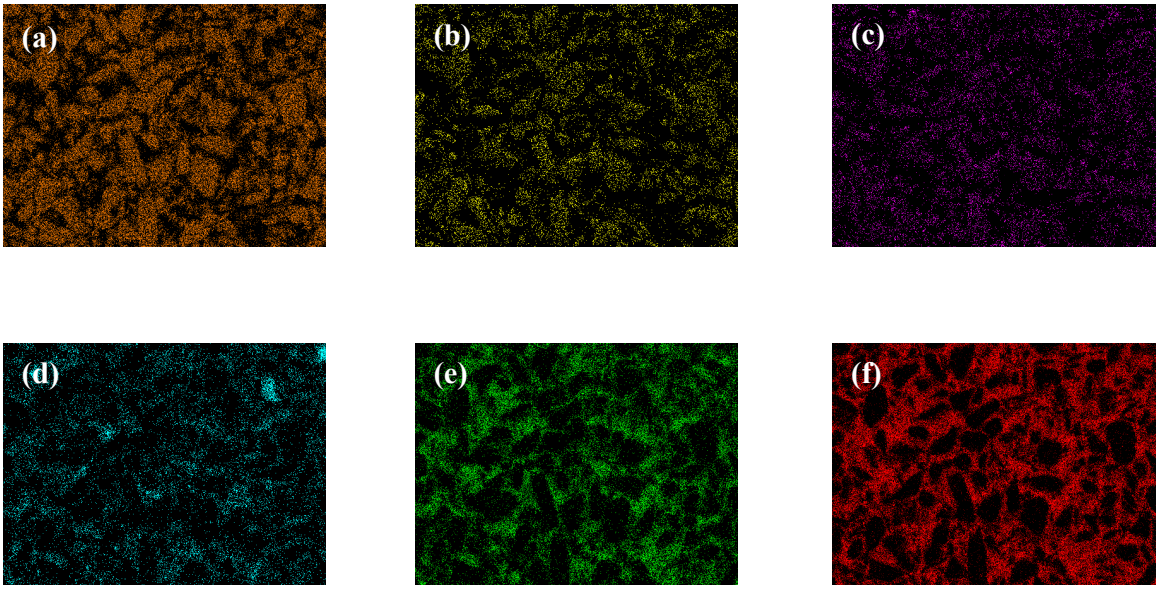

Figure 16: EDS mappings resulting from the EDS analysis done on the area shown in Figure 15. The elements shown in the EDS mappings are (a) Ti, (b) B, (c) N, (d) C, (e) O, and (f) Si.

3.2.2 Samples Having a TiB_2 Fraction of 0.292

Once the specimens were pyrolyzed, they were cut and polished. It should be noted that samples were polished on 120 grit, 400 grit, and 600 grit paper as well as on polishing cloth in conjunction with 50-nm colloidal silica. SEM imaging and EDS were executed on the polished surface to analyze the microstructure of the specimens. Unless otherwise stated, this is how samples were prepared for SEM imaging and EDS.

3.2.2.1 SEM Imaging

Figure 17 represents an SEM image of the polished cross-section. An observation of Figure 17 indicates a similar microstructure to that of pyrolyzed samples made with a TiB_2 volume fraction of 0.331 (Figure 15) in that the microstructure consists of inclusions with within a matrix material.

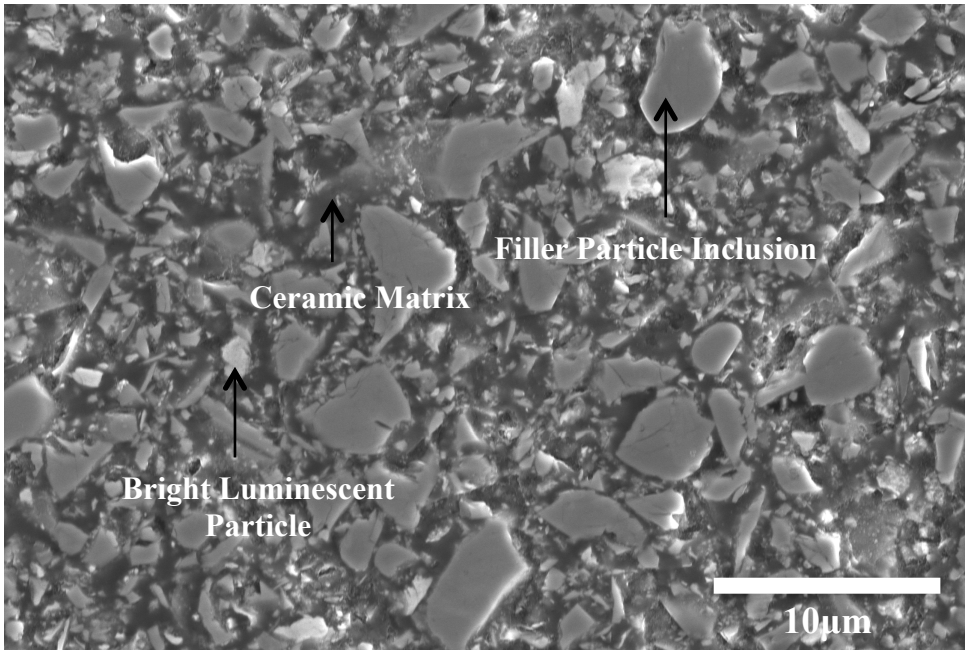

Figure 17: SEM image of a sample with a TiB_2 volume fraction of 0.292. The location of the SEM image shown also serves as the site used for EDS analysis.

It is evident here that there seems to be two distinct sets of inclusions with different sizes; one consisting of inclusions with a size equivalent to the size of the inclusions seen in the microstructure of a 0.331 TiB_2 volume fraction pyrolyzed sample (Figure 15) and one consisting of noticeably smaller-sized inclusions. This behavior is expected because the build material solution used to fabricate the 0.292 TiB_2 volume fraction samples were ball-milled whereas the solution used to fabricate the 0.331 TiB_2 volume fraction samples

were not ball-milled. Since the purpose of ball milling the build material solution is to decrease the particle size, ball-milled samples should have a higher concentration of smaller-sized particles than do samples that were not ball-milled. This would lead to a higher concentration of smaller-sized inclusions within the pyrolyzed ball-milled samples than there would be within the pyrolyzed samples that were not ball-milled, like what is seen with the comparison between Figure 15 and Figure 17.

3.2.2.2 EDS Analysis

Figure 18 provides a representative result for the EDS analysis of the polished cross-section. By comparing Figure 18 to Figure 17, it is evident that the inclusions within the microstructure contain Ti and the matrix material contains O and Si. From observations of the EDS mappings of B, N, and C in Figure 18, it is hard to gain much information about what parts of the microstructure contain those elements. This is due to the fact that at the location at which the EDS analysis was executed, the concentration of those elements is low, making it difficult for the EDS analysis to properly track the presence of those elements. Fortunately, since it has been shown that the microstructure of this sample is very similar to that of the pyrolyzed 0.331 TiB_2 volume fraction sample, it is safe to assume that the inclusions represent the expanded TiB_2 active filler and the matrix material represents the pyrolyzed version of the starting PCP, consisting of elements Si, O, and C. An observation of Figure 18(g) indicates that there is a significant presence of Zr contamination. This corresponds to the bright luminescent particles seen within the SEM image shown in Figure 17. This can be attributed to Zr particles

detaching from the balls and container during the ball milling process and getting infused into the build material solution.

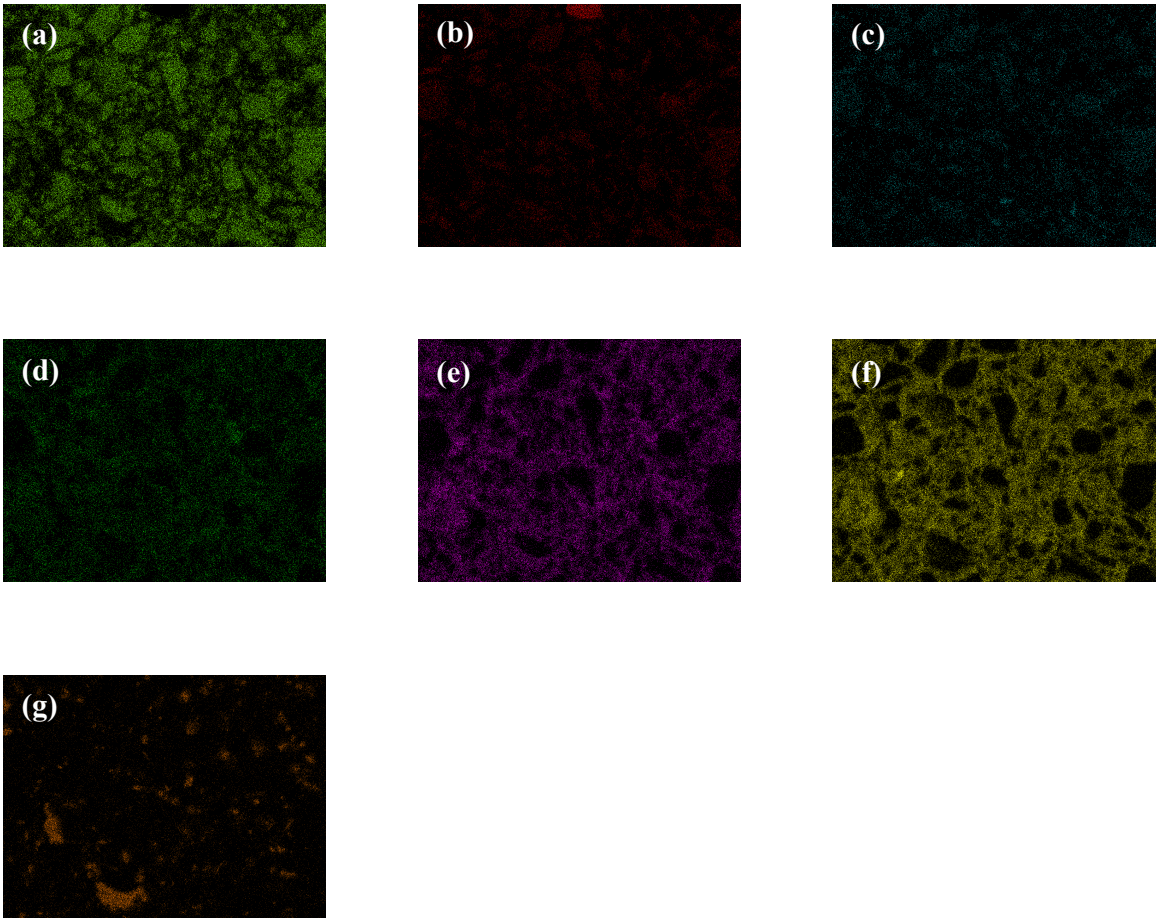

Figure 18: EDS mappings resulting from the EDS analysis done on the area shown in Figure 17. The elements shown in the EDS mappings are (a) Ti, (b) B, (c) N, (d) C, (e) O, (f) Si, and (g) Zr.

3.2.3 Samples Having a TiB_2 Volume Fraction of 0.216

Once the specimens were pyrolyzed, they were cut and polished in order to analyze the microstructure via SEM imaging and EDS.

3.2.3.1 SEM Imaging

Figure 19 represents an SEM image of the cross-section. An observation of Figure 19 indicates a similar microstructure to previously discussed pyrolyzed versions of the build material in that the microstructure consists of inclusions within a matrix material.

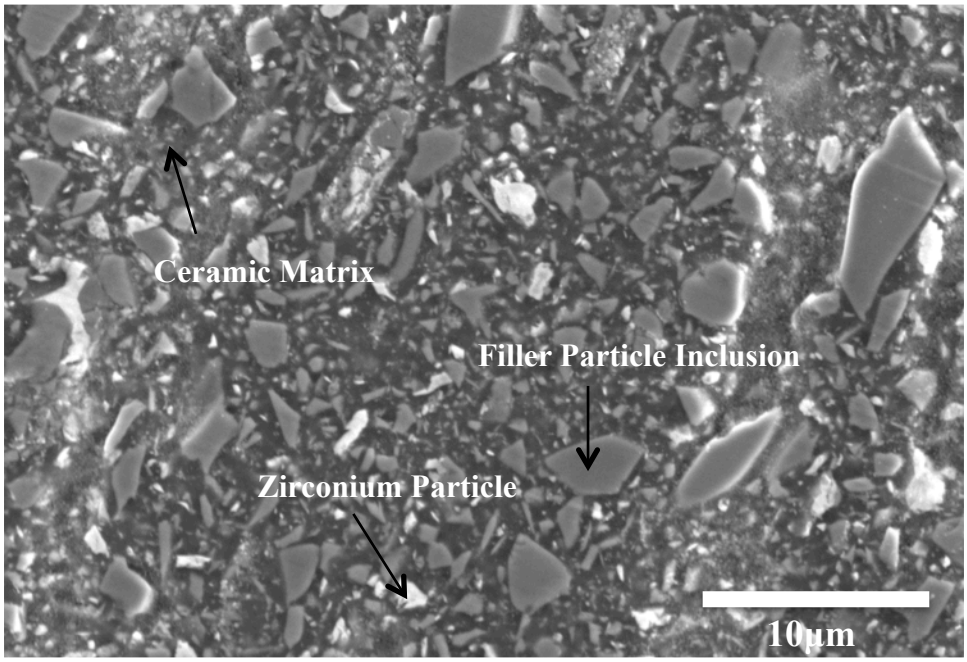

Figure 19: SEM image of a sample with a TiB_2 volume fraction of 0.216. The location of the SEM image shown also serves as the site used for EDS analysis.

It is evident that like what was seen previously with the pyrolyzed samples fabricated using a TiB_2 volume fraction of 0.292, there seem to be two distinct sets of inclusions each with different sizes. A comparison between the SEM image of the cross-section of a pyrolyzed sample with a TiB_2 volume fraction of 0.292 (Figure 17), the SEM image of the cross-section of a pyrolyzed sample with a TiB_2 volume fraction of 0.331(Figure 15), and the SEM image shown in Figure 19, indicates a higher concentration of the smaller-sized inclusions within the microstructure of the 0.216 TiB_2 volume fraction sample than seen with both the 0.292 and 0.331 TiB_2 volume fraction samples. This is expected

because the significant increase in ball milling time (12 hours as compared to 0 hours and 4 hours for 0.331 and 0.292 TiB_2 volume fraction samples, respectively) should produce an increased concentration of the smaller-sized particles within the build material solution, which in turn, should increase the concentration of smaller-sized inclusions within the microstructure of the pyrolyzed product.

3.2.3.2 EDS Analysis

Figure 19 and Figure 20 provide a representative result for the EDS analysis of the cross-section. Figure 19 represents the SEM image used for the EDS analysis whereas Figure 20 represents the different element mappings that were constructed during the EDS analysis.

By comparing Figure 20 to Figure 19, it is evident that the inclusions represent the expanded TiB_2 active filler and the matrix material represents the pyrolyzed version of the starting pre-ceramic polymer, consisting of elements Si, O, and C. Since the EDS mappings for Iron (Fe) and Sodium (Na) show a well-distributed, small concentration of these elements over the entire analysis site and production of the build material did not include the use of either of these elements, it is safe to attribute the formation of the Fe and Na mappings during the EDS analysis to the presence of background noise. The comparison of Figure 19 and Figure 20 also indicates that there is a significant presence of Zr contamination, which is attributed to Zr particles detaching from the balls and the container during ball milling and getting infused into the build material solution. A comparison of the EDS mapping of Zr for the 0.292 TiB_2 volume fraction sample (Figure 18(g)) to that for the 0.216 TiB_2 volume fraction sample (Figure 20(g)) shows an increase in the concentration of Zr particles within the 0.216 TiB_2 volume fraction sample. This is

as expected since it is likely that more Zr particles would get infused into the build material with increased ball milling time (12 hours as opposed to 4 hours).

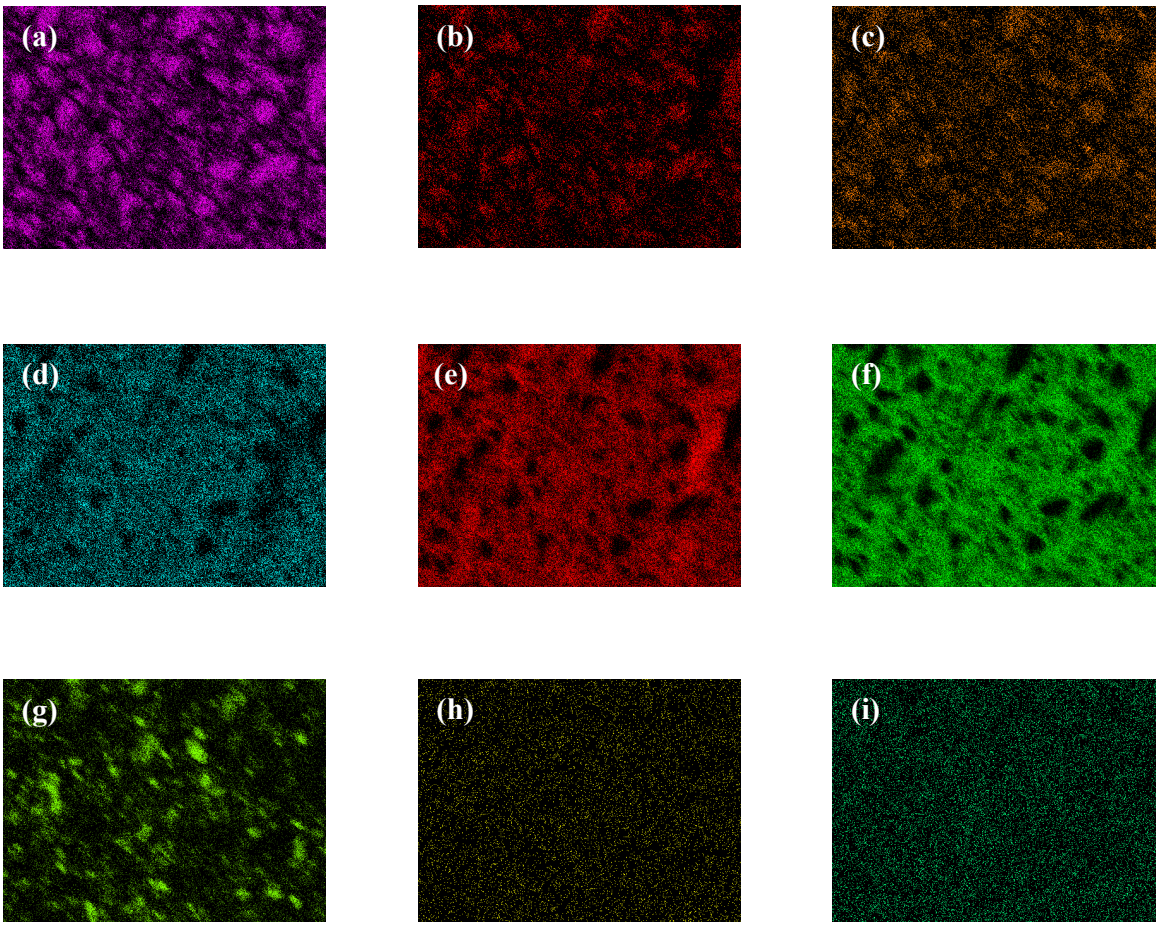

Figure 20: EDS mappings resulting from the EDS analysis done on the area shown in Figure 19. The elements shown in the EDS mappings are (a) Ti, (b) B, (c) N, (d) C, (e) O, (f) Si, (g) Zr, (h) Fe, and (i) Na.

3.2.4 Samples Having a TiB_2 Volume Fraction of 0.414

Once the specimens were pyrolyzed, they were cut and polished using 120, 400, and 600 grit sandpaper. A final polish was executed on polishing cloth in conjunction with 50-nm colloidal silica to achieve a 50-nm finish. SEM imaging and EDS were done on the polished surface to analyze the microstructure of the specimens.

3.2.4.1 SEM Imaging

Figure 21 represents an SEM image of the polished surface of a pyrolyzed sample fabricated with a 0.414 TiB_2 volume fraction. An observation of Figure 21 shows that this sample has a very similar microstructure to that of the samples made with the other build material solution variants. Also, the inclusion size is similar to that of the samples made with a 0.331 TiB_2 volume fraction.

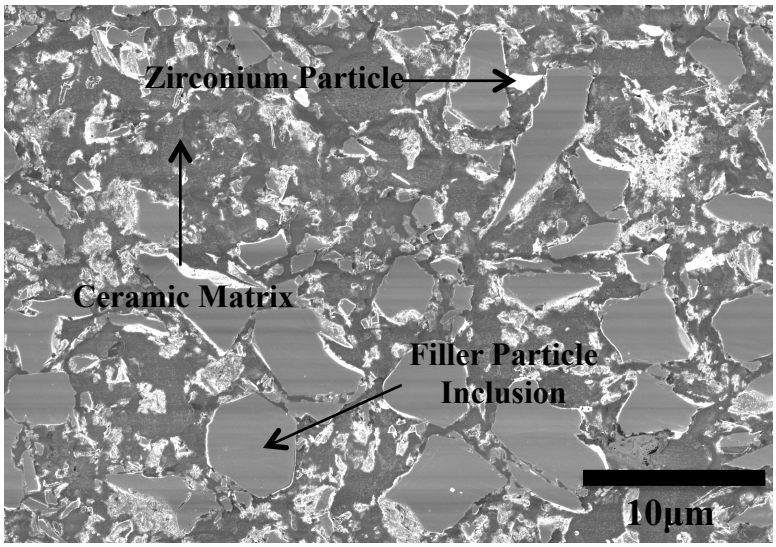

Figure 21: SEM image of a sample with a TiB_2 volume fraction of 0.414.

This is as expected since the ball milling time for these samples was only 45 minutes, which is not enough time to cause a significant decrease in the particle size. Unlike with the other build material solutions, an EDS analysis was not performed on this sample. This was because this was the last sample to go through SEM imaging, which meant that by showing that the microstructure was similar to that of the other samples, the composition of the microstructure could be predicted with high accuracy without the use of EDS. Therefore, it is clear from Figure 21 that like with the other samples, the

inclusions within the microstructure represent the expanded TiB_2 active filler, the matrix material represents the pyrolyzed-version of the starting pre-ceramic polymer, consisting of elements Si, O, and C, and the bright luminescent particles represent Zr particles that are a product of contamination caused by the ball milling process.

3.2.5 Particle Size Analysis

Using the SEM images of the microstructure, the particle size was measured. Figure 22 represents a histogram of the particle size. From observing Figure 22, it is evident that samples made with a longer ball milling time have a higher frequency of smaller-sized particles than do samples made with less ball milling. Also, as the particle size is increased, samples made with less ball milling have a higher frequency of increased-size particles than do samples made with a longer ball milling time. This is as expected because while the solution is ball-milled, particles are being broken up into smaller pieces. Therefore, as the solution continues to be ball-milled, the amount of smaller-sized particles increases whereas the amount of particles with their original size decreases. This is why the samples made with 4 hours of ball milling have a smaller frequency of particles < 1 μm than do the samples made with 12 hours of ball milling.

In addition to creating a histogram of the particle size, a plot was made of the average particle size as a function of the ball milling time as shown in Figure 23. From observation of the plot, it is clear that the average particle size decreases as the ball milling time increases. This is as expected since it agrees with the histogram shown in Figure 22.

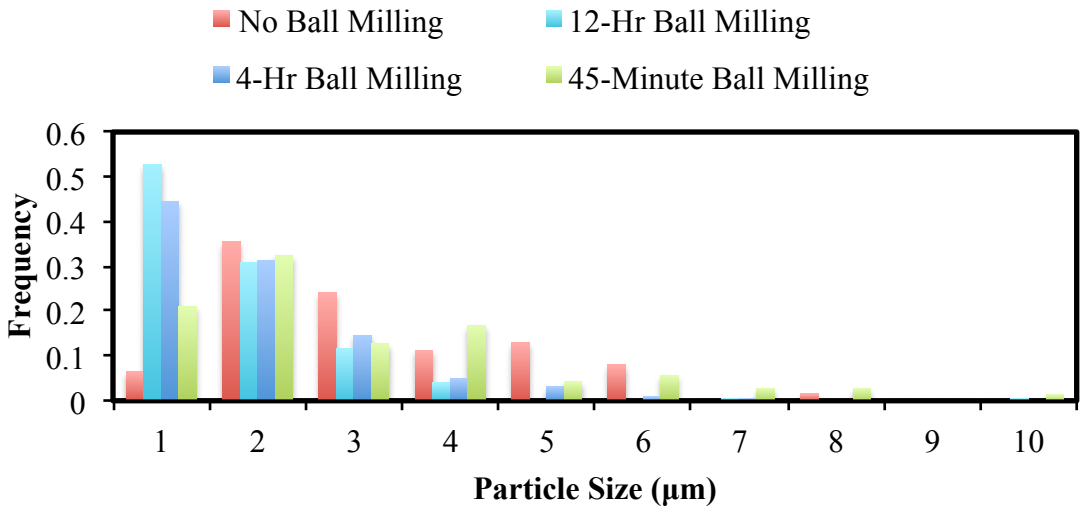

Figure 22: Histogram of the particle size distribution between samples that were ball-milled for either 0 hours, 45 minutes, 4 hours, or 12 hours.

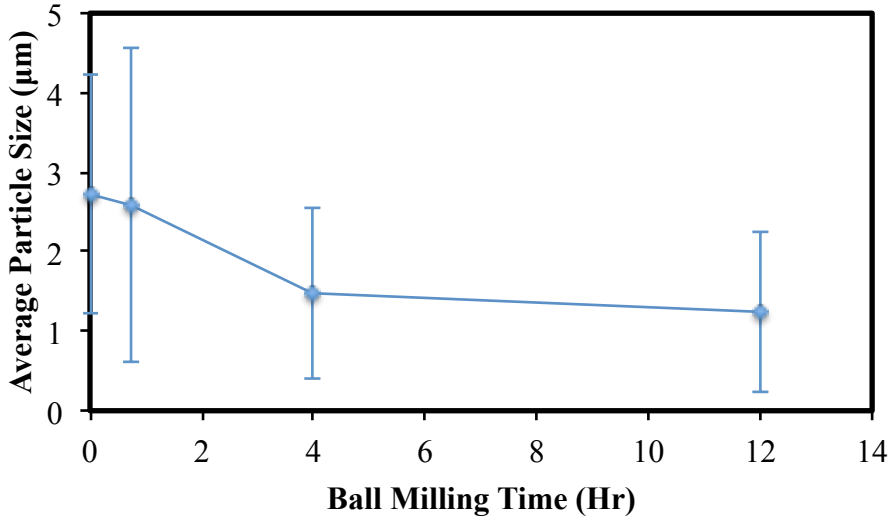

Figure 23: Plot of Average Particle Size vs. Ball Milling Time.

In order to determine whether the TiB_2 particles serve as active fillers or inactive fillers, the average particle size before and after pyrolysis was calculated for a sample with a TiB_2 volume fraction of 0.216 using the SEM images shown in Figure 24 and Figure 19, respectively. This resulted in the sample having an average particle size of 0.867 µm before pyrolysis and 1.238 µm after pyrolysis, which represents a 42.79%

increase in the average particle size during pyrolysis. Since this increase can be considered significant (very large in fact), it is safe to assume that the TiB_2 particles should increase in size during pyrolysis, which means that they must react with the N_2 atmosphere during pyrolysis, thus confirming their status as active fillers. It is important to note that since it is nearly impossible to tell whether the SEM images taken before (Figure 19) and after (Figure 24) pyrolysis represents the same location within the microstructure, it is most likely that these two SEM images do not represent the same location within the microstructure. Therefore, the particle size analysis executed in the present work to confirm the TiB_2 particles' status as active fillers should be viewed more as a qualitative analysis as opposed to a quantitative one. In order to obtain a quantitative analysis of the particle size increase experience during pyrolysis, one should find a way to measure particle size before and after pyrolysis using the same location of the microstructure. This would explain why the particle size experienced during pyrolysis (42.79%) is so large.

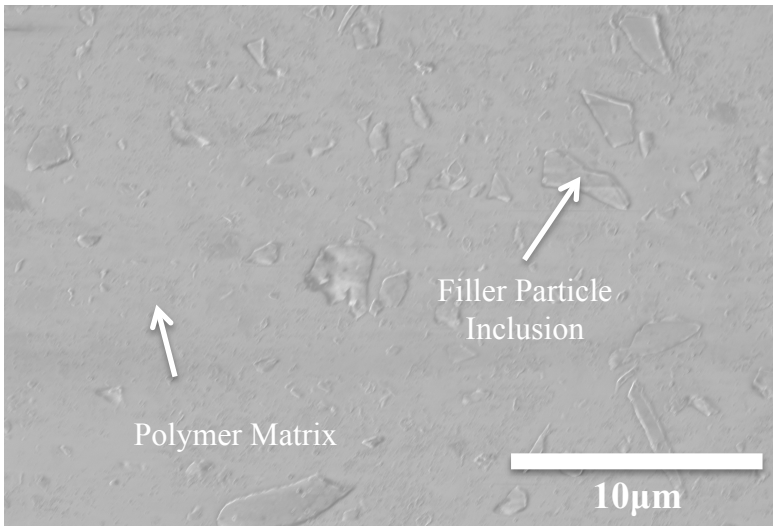

Figure 24: SEM image of a polished cross-section of a pre-pyrolyzed sample with a TiB_2 volume fraction of 0.216 and that was ball milled for 12 hours.

3.2.6 X-Ray Photoelectron Spectroscopy (XPS) Analysis

In order to see what type of bonds make up the microstructure of the final ceramic, x-ray photoelectron spectroscopy (XPS) was executed on a polished and etched surface of a pyrolyzed sample. The resulting plot of counts/s as a function of the binding energy is shown in Figure 25. From previous work from other researchers[87-91] as well as from the XPS results themselves, the peaks within the plot were able to be determined along with their associated elements and bonds, which are listed in Table 5.

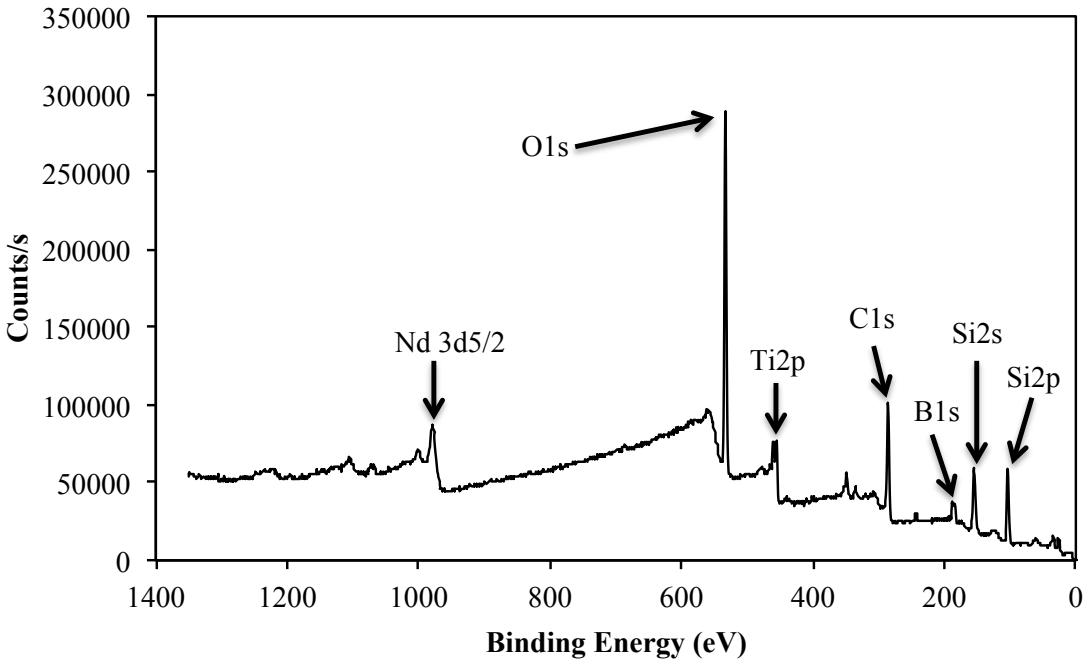

Figure 25: XPS result for a pyrolyzed sample that has a TiB_2 volume fraction of 0.292.

From Table 5, it is clear that the XPS analysis indicates that the bonds that make up the microstructure of the pyrolyzed samples are Nd, SiO_2, TiN, Silicon oxycarbide, graphitic or "adventitious" carbon, and TiB_2. Overall, it makes sense for the microstructure to consist of several of these bonds. From the EDS analyses, it was

Table 5: XPS Peak Assignment for a Pyrolyzed Sample

Element	Peak Position (eV)	Bond
Nd 3d5/2	980.85	Neodymium (Nd)[90]
O1s	533.0	Silica (SiO_2)[91]
Ti2p	455.3	Titanium nitride (TiN)[87]
C1s	284.6	Silicon oxycarbide, graphitic or "adventitious" carbon[91]
B1s	187.5	Titanium diboride (TiB_2)[89]
Si2s	154.6	Silica (SiO_2)[88]
Si2p	101.7	Silicon oxycarbide[91]

determined that the inclusions consisted of the elements Ti, B, and N. Therefore, the presence of TiN is not surprising. In fact, this behavior makes sense because the reaction of the TiB_2 particles with the N_2 atmosphere during pyrolysis should cause TiN bonds to form.[76] Additionally, the presence of TiB_2 bonds also makes sense since the inclusions start off as TiB_2 particles within the starting build material solution. Since the PCP is a polycarbosiloxane, it is known that the pyrolyzed product of the PCP should be a ceramic containing the elements Si, O, and C, which was confirmed by EDS analysis. Therefore, one should expect XPS to find bonds within the microstructure that contain a combination of the elements Si, O, or C. This is seen at the peak locations of 530.0, 284.6, 154.6, and 101.7 eV with the presence of SiO_2, Silicon oxycarbide, or graphitic/adventitious carbon bonds. The only result from this XPS analysis that does not make sense is the peak seen at 980.85 eV, which corresponds to the presence of Nd. A possible reason for this could be due to noise in the XPS data. From Figure 25, it is clear that the peak at 980.85 eV is noticeably smaller than most of the other peaks and the counts/s seem to become relative constant for increased binding energy. Another possible reason for the presence of Nd could be due to contamination associated with preparing

the sample for XPS. This reason is less likely to be true since the sample used for XPS should have never came into contact with anything containing the element Nd.

3.3 Mechanical Property Characterization

3.3.1 Modulus and Hardness Measurements

In order to obtain a measurement of the Young's modulus and hardness for the final ceramic, nanoindentation tests were performed on fabricated pyrolyzed samples. It should be noted that the indenter tip was made out of diamond[92] and had a cubic-corner geometry. Nanoindentation was performed on multiple samples that were fabricated using different variants of the build material solution. Table 6 presents the parameters used for each nanoindentation test done on these samples.

Table 6: Nanoindentation Test Data

Volume Fraction of TiB_2	Number of Points	Grid Size (points x points)	Nanoindentation Size (μm x μm)	Force (μn)
0.331 (Pre-Pyrolyzed Sample)	289	17 X 17	80 x 80	2000
0.331 (Pyrolyzed Sample)	361	19 x 19	54 x 54	2000
0.292	289	17 x 17	48 x 48	2000
0.216	289	17 x 17	48 x 48	2000

For each nanoindentation test performed, the reduced modulus E_r and hardness H were measured at each point. By averaging the values for E_r and H for each point, it is possible to obtain an average E_r and H for the nanoindentation test region. Since the

microstructure is consistent throughout, it is safe to apply the average values for E_r and H to the entire sample.

To obtain a visual representation of the reduced modulus and hardness, color maps were made to provide a visual representation of the reduced modulus and hardness for each data point taken for each test. Figure 26 and Figure 27 serve as a representation of the reduced modulus and hardness for a pre-pyrolyzed sample, respectively whereas Figure 28 and Figure 29 serve as a representation of the reduced modulus and hardness for a pyrolyzed sample, respectively. It is important to note here that although Figures 26 – 29 were made with only the nanoindentation test data from samples with a TiB_2 volume fraction of 0.331 in mind, they represent a trend that was seen throughout. A few key observations of these figures encompass some important results. It is evident that there are concentrated areas of relatively high-valued reduced modulus or hardness within a matrix of relatively low-valued reduced modulus or hardness. Also, a comparison of the reduced modulus and hardness maps shows that points that represent a high level of modulus correspond to points with a high level of hardness and points that represent a low level of modulus correspond to points with a low level of hardness. It can be assumed that the high-valued points (sometimes reaching up to approximately 350 GPa for the pyrolyzed samples) represent a test point that was taken on a TiB_2 filler particle and the low-valued points represent a point taken on the matrix material since TiB_2 has a significantly larger modulus and hardness than does the ceramic matrix material and the SEM/EDS images of the samples indicate the presence of TiB_2 inclusions existing within a matrix material that corresponds to the pyrolyzed PCP.

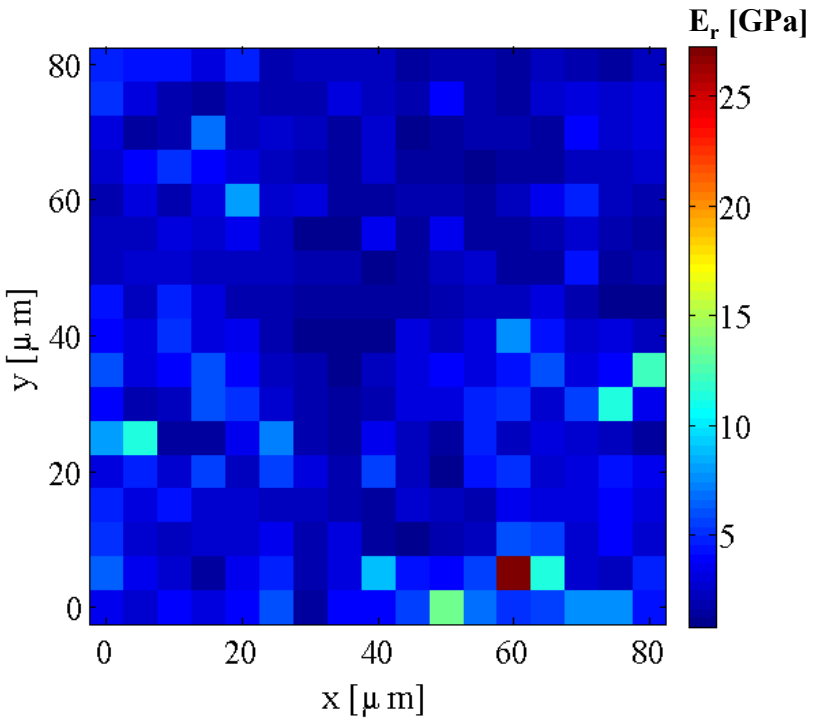

Figure 26: Map of the reduced modulus for a pre-pyrolyzed sample with a TiB_2 volume fraction of 0.331.

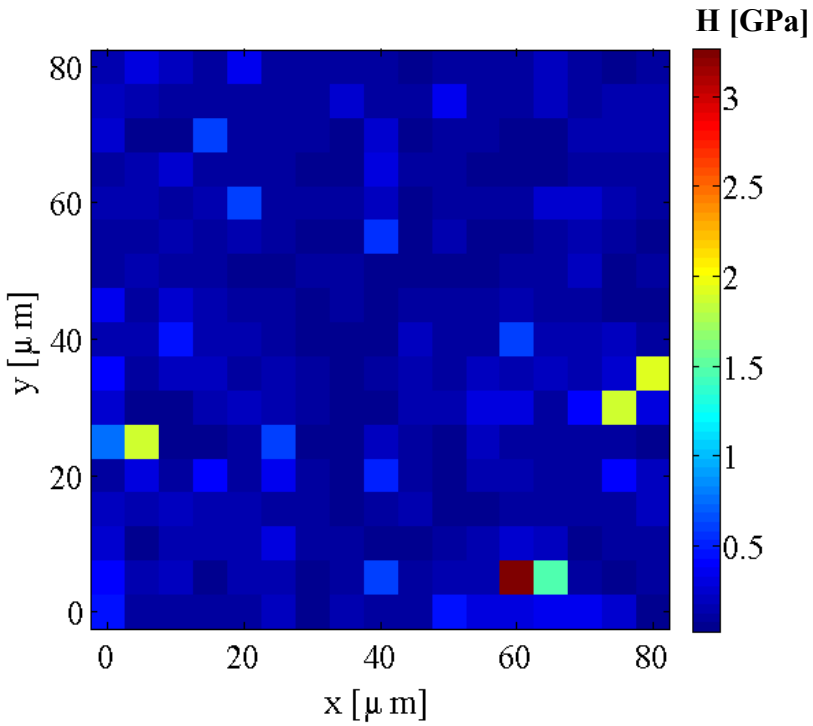

Figure 27: Map of the hardness for a pre-pyrolyzed sample with a TiB_2 volume fraction of 0.331.

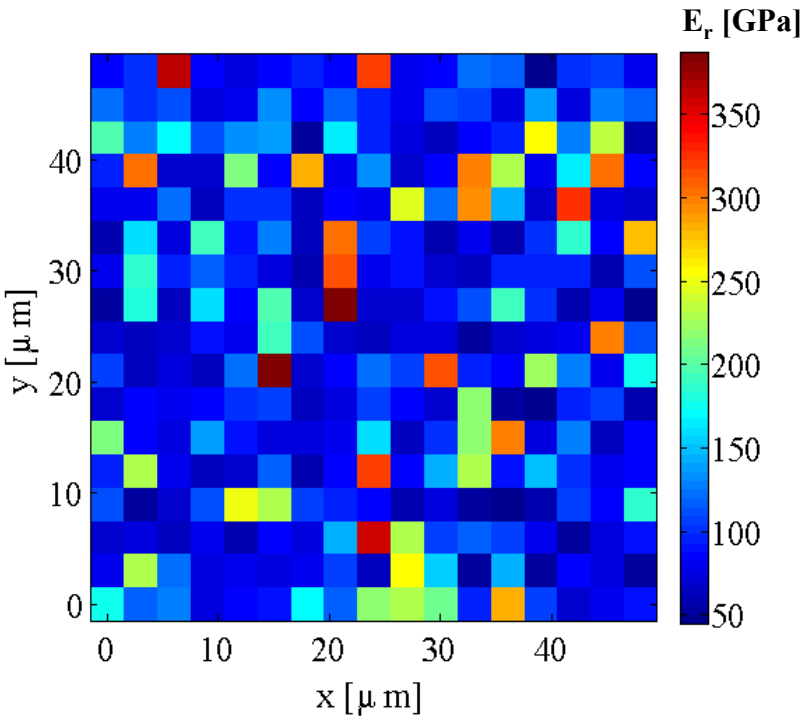

Figure 28: Map of the reduced modulus for a pyrolyzed sample with a TiB_2 volume fraction of 0.331.

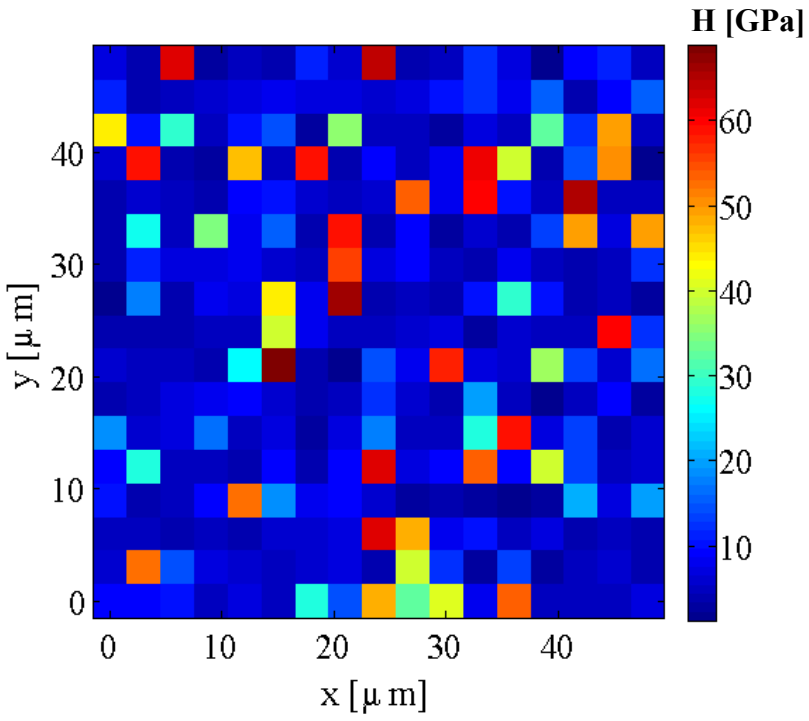

Figure 29: Map of the hardness for a pyrolyzed sample with a TiB_2 volume fraction of 0.331.

A Comparison of the reduced modulus and hardness maps for a pre-pyrolyzed sample (Figure 26 and Figure 27) to the reduced modulus and hardness maps of a pyrolyzed sample (Figure 28 and Figure 29) makes it evident that both the modulus and hardness of the material significantly increase during pyrolysis. This is as expected because pyrolysis transforms the fabricated samples from polymers into ceramics, which inherently have much higher modulus and hardness than do polymers.

Although the nanoindentation test results do not explicitly measure the Young's modulus E, the reduced modulus can be used to derive the Young's modulus using the equation,

$$\frac{1}{E_r} = \frac{1-\nu^2}{E} + \frac{1-\nu_i^2}{E_i} \tag{13}$$

where E is the Young's modulus of the sample, E_r is the reduced modulus, E_i is the Young's modulus of the indenter, ν is the Poisson's ratio of the sample, and ν_i is the Poisson's ratio of the indenter.[93]

Since the indenter tip is made out of diamond E_i and ν_i can be assumed to be 862.5 GPa and 0.20, respectively.[94] Also, since the material we are testing is either a polymer (pre-pyrolyzed) or ceramic (pyrolyzed), it is safe to assume a value of 0.33 for ν for pre-pyrolyzed samples and a value of 0.25 for ν for pyrolyzed samples.[95] By setting E_r to the average reduced modulus and plugging in the values, 862.5, 0.20, and 0.25 for E_i, ν_i, and ν, respectively, the average Young's modulus can be calculated for each nanoindentation test that was executed on a pyrolyzed sample. Figure 30 shows a plot of both the average Young's modulus and hardness as a function of the volume fraction of TiB_2 for each of the pyrolyzed samples that were tested. An observation of this plot indicates that for most part, both the Young's modulus and hardness tend to slightly

decrease as the volume fraction of TiB_2 increases. This is unexpected since it has been shown that within pyrolyzed samples, that TiB_2 has a higher modulus and hardness than does the matrix material as seen in Figure 28 and Figure 29, respectively. Therefore, if the concentration of TiB_2 is increased, which in turn, increases the volume fraction of TiB_2, the modulus and hardness of the material should increase as well. A reason for the slight decrease in Young's modulus and hardness is that it was assumed that the results for each test region could be applied to the entire sample. Since it is impossible to get perfect dispersion of particles, it is possible that the test region used for nanoindentation included less or more particle than what is truly representative of the entire sample, which would lead to an underestimation or overestimation of the modulus and hardness, respectively. Ultimately, the fact that the modulus and hardness of the material maintain relatively constant as the volume fraction increases indicates that the volume fraction of TiB_2 does not have a significant impact on overall modulus and hardness of the final ceramic.

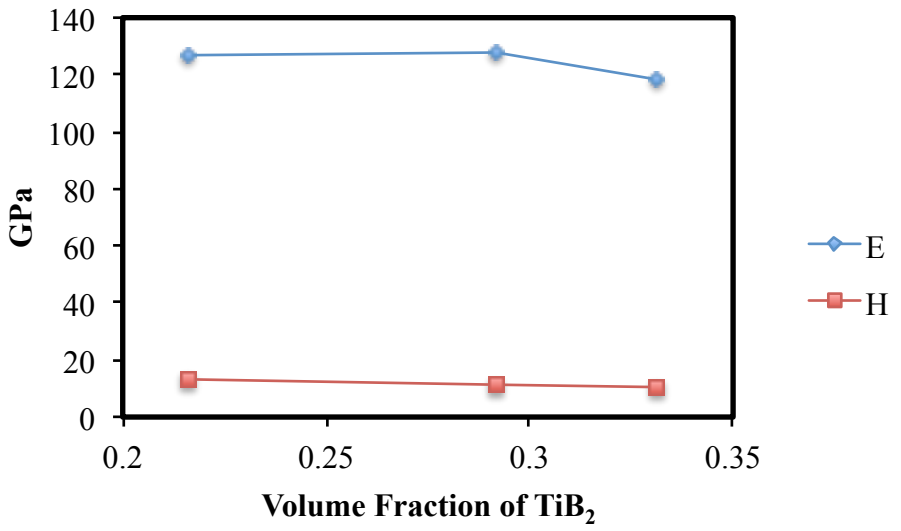

Figure 30: Plot of the modulus and hardness as a function of the volume fraction of TiB_2 within the starting build material solution. This data was obtained from the nanoindentation tests that were performed.

3.3.2 Fracture Toughness Measurement

To determine the fracture toughness of fabricated pyrolyzed samples, indentation was utilized. The indentation setup uses a force gauge with an attached indenter to make an indent into the sample with enough force to initiate a crack. Several indents were made into several pyrolyzed samples made with different volume fractions of TiB_2. It should be noted that for each indent made, a Vickers pyramidal indenter tip was utilized and the peak indentation load was 200 N. Since cracks were difficult to see with either the naked eye or an optical microscope, SEM images of each indent were taken. Figure 31 represents one these SEM images.

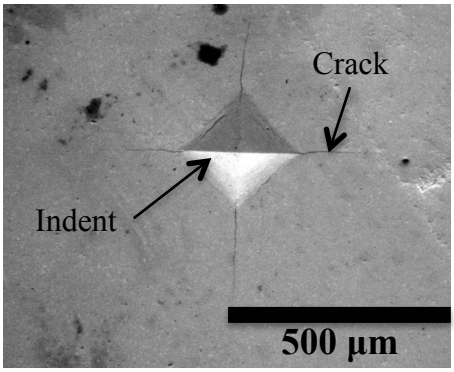

Figure 31: SEM image of an indent made into a pyrolyzed sample using a Vickers indenter tip and a peak indentation load of 200 N. It should be noted that this figure represents one of several images that were taken in order to obtain the fracture toughness measurements.

An observation of Figure 31 indicates that these SEM images can be used to measure the crack length and indent size, which are both needed for calculation of fracture toughness. Also, it is clear from Figure 31 that an indent can initiate as many as four cracks. Therefore, in the case where there were multiple cracks present, an average crack length was calculated to serve as the characteristic crack length used in the fracture

toughness calculation. For each indent, the characteristic crack length c and the indent size a were measured. Figure 32 represents a schematic of an indent, showing how both c and a were measured.

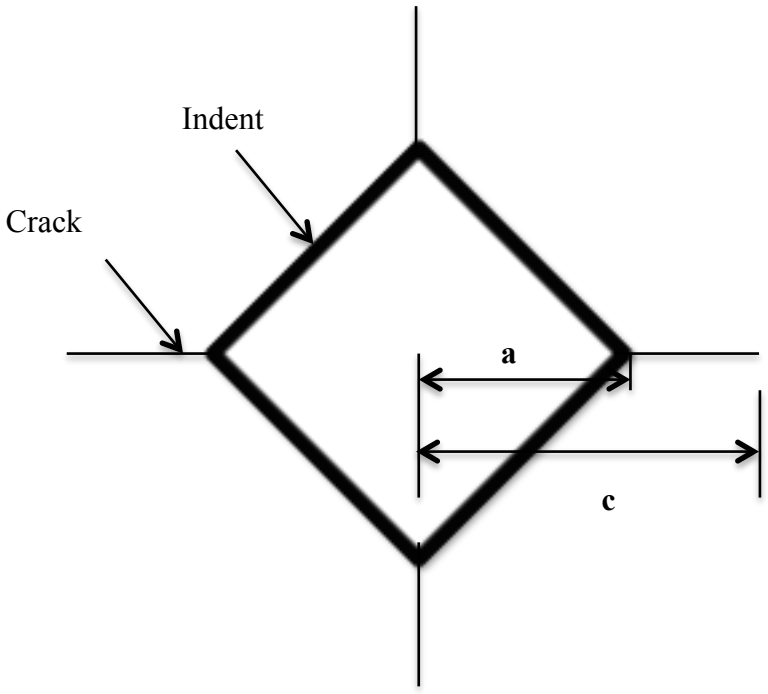

Figure 32: Schematic of crack initiation due to indentation into pyrolyzed samples using a Vickers pyramidal indenter tip.

In order to calculate the fracture toughness, one needs to determine the critical stress intensity fractor K_C by using the equation,

$$K_C = \alpha \sqrt{\frac{E}{H}} \frac{P}{c^{3/2}} \tag{14}$$

where α is an empirical constant, E is the Young's modulus, H is the hardness, P is the peak indentation load, and c is the characteristic crack length.[93] Also, it should be noted here that K_C is synonymous with fracture toughness. Since a Vickers pyramidal indenter

tip was used to make the indents as opposed to the cubic-corner tip used for nanoindentation, α has a value of 0.016. Also, since the estimation of hardness is dependent on the indenter tip, the hardness H that is used in equation (14) (usually called the Vickers hardness) is not equivalent to the hardness that was found during nanoindentation. To obtain H for the fracture toughness calculation, the equation

$$H = \frac{P}{2a^2} \tag{15}$$

was used, where P is the peak indentation load and a is the indent size. Since it is known that the peak indentation load is 200 N, P is given a value of 200 in equation (14) and equation (15). Using the known indent size, equation (15) was utilized to determine H for each indent. Then, equation (14) was used to determine K_C for each indent. The values of H and K_C for indents made into samples fabricated from the same build material solution were averaged together to obtain an average value of H and K_C for each build material variant. Figure 33 and Figure 34 represent the average hardness and average fracture toughness as a function of the volume fraction of TiB_2, respectively. A comparison between these two figures indicates a mostly inversely proportional relationship between the fracture toughness and the hardness. This is as expected because equation (14) shows that the fracture toughness is inversely proportional to the hardness and the Young's modulus was shown to be relatively constant with respect to the volume fraction of TiB_2. Therefore, higher hardness should be associated with lower fracture toughness and vice versa. The only point on both plots that does not represent the expected inversely proportional relationship between fracture toughness and hardness is at a TiB_2 volume fraction of 0.414. A reason for this behavior could be that at a filler particle volume fraction of 0.414, it is possible for enhanced porosity to occur, which lowers the

mechanical properties of the final ceramic.[75] If that is indeed the case, then at a TiB_2 volume fraction of 0.414, one should expect the fracture toughness to decrease, which corresponds to an increase in hardness. This would explain why the fraction toughness barely increases and the hardness significantly increases as the volume fraction of TiB_2 increases from 0.331 to 0.414.

From looking at Figure 33, it is clear that fracture toughness increases with the increase of the volume fraction of TiB_2. This makes sense because the addition of TiB_2 helps to impede crack propagation as will be discussed in the following section, thus increasing the fracture toughness of the material. Also, it is important to note that from an observation of Figure 33 and Figure 34, one sees that the fracture toughness ranges from approximately 3 – 5 $MPa\sqrt{m}$ and that the hardness of the material ranges from approximately 3.5 – 5 GPa.

The behavior of the fracture toughness in relation to the volume fraction of TiB_2 resembles that of other work that deals with the fabrication of ceramics using PCP in conjunction with filler particles. In the work of Parcianello et al.[96], zirconia (ZrO_2) filler particles were added to a solution containing PCP and isopropyl alcohol (IPA) in order to produce ceramic parts via pyrolysis. Variants of the mixture, which varied in the volume fraction of ZrO_2 particles within the solution, were created to analyze the behavior of the final ceramics as a function of the volume fraction of ZrO_2. This included analyzing the fracture toughness of the pyrolyzed product. Like what was seen in the present work, as the volume fraction of ZrO_2 increased, so too did the fracture toughness. Additionally, the fracture toughness of the final ceramic ranges from approximately 2 – 6.5 $MPa\sqrt{m}$ as the volume fraction of ZrO_2 is increased from 0 to 0.300, which shows similar behavior to

what is shown in present work where the fracture toughness ranges from approximately 3 – 5 MPa$\sqrt{m}$.

Compared to common engineering ceramics such as Alumina (Al_2O_3) and Silicon Carbide (SiC), which have a fracture toughness ranging from 2.0 – 6.0 MPa$\sqrt{m}$ and 3.0 – 6.0 MPa$\sqrt{m}$, a hardness ranging from 19.0 – 26.0 GPa and 26.0 – 36.0 GPa, and a Young's modulus of 390 GPa and 430 – 450 GPa, respectively[97], the samples made here have similar fracture toughness, lower hardness, and lower Young's modulus. Out of these three material properties, fracture toughness is the most important in relation to the present work as it is the main determinant of whether the prototype system is able to fabricate parts that avoid brittle failure in the environments for which they are purposed. This means that the reduced hardness and Young's modulus as compared to these common engineering ceramics is not reason for concern. However, this reduced hardness and Young's modulus does make the fabricated final ceramic prone to other modes of failure. Therefore, in order to produce a ceramic that can withstand all possible modes of failure, the both the Young's modulus and hardness must be increased. This will require manipulation to the build material solution. Also, since these common engineering ceramics are typically produced using non-additive manufacturing methods such as pressing[97], the similar fracture toughness shows that it is possible to employ additive manufacturing to fabricate ceramic parts that can withstand the environments in which common engineering ceramics must function.

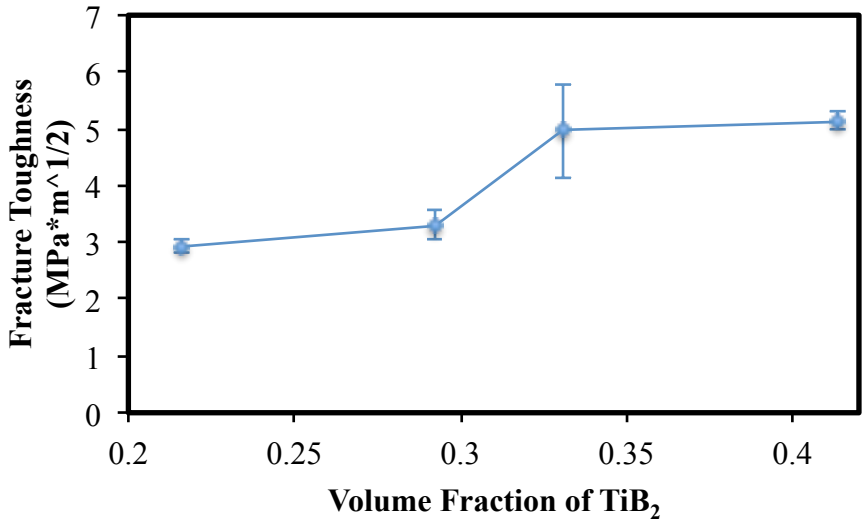

Figure 33: Plot of the fracture toughness vs. volume fraction of TiB_2 within the starting build material solution.

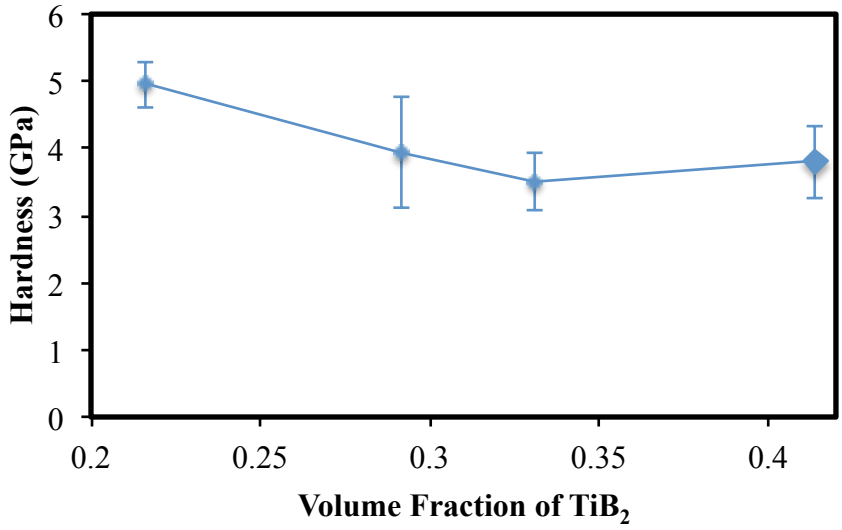

Figure 34: Plot of the hardness vs. volume fraction of TiB_2 within the starting build material solution.

3.4 Toughening Mechanisms

As seen in the previous section, the fracture toughness increases with the increase in the volume fraction of TiB_2. This increase in fracture toughness can be attributed to a few toughening mechanisms that come into play with addition of the TiB_2 filler particles into

the PCP matrix. These toughening mechanisms are crack deflection, secondary phase toughening, and elastic heterogeneity.

When the TiB_2 filler particles are added to the starting PCP, the particles make up inclusions within the ceramic matrix that are formed during pyrolysis. These inclusions serve as roadblocks that deflect cracks, impeding their propagation. This means that a larger stress is required in order to cause brittle failure than there would be if no filler particles were present, thus increasing the fracture toughness of the material.

The addition of TiB_2 particles also provides toughening due to the fact that their presence alone introduces a secondary phase into the ceramic. Similar to how light changes direction when transferring into a medium of different index of refraction, when a crack reaches the secondary phase, it will change its direction since the TiB_2 particles have a different stiffness than does the ceramic matrix. This, in turn, slows down crack propagation, thus increasing fracture toughness.

As stated before, another way the TiB_2 particles toughen the ceramic product is through elastic heterogeneity. Since TiB_2 filler particles have a higher Young's modulus than does the ceramic matrix, the effective Young's modulus of the material is increased. This makes the overall material stiffer and less prone to crack propagation, therefore increasing the overall fracture toughness of the ceramic.

3.5 Conclusions

In Section 3.1, the capability of producing near-net-shape parts and the effectiveness of each setup of the prototype system were evaluated. It was shown that the prototype system is capable of producing parts with very low volume shrinkage and dimensional error as is exemplified in Figure 13 and Figure 14, respectively. It was also shown in this

section that compared to other recently developed additive manufacturing methods for fabricating ceramics[85, 86], the prototype system is capable of producing parts that experience less volume shrinkage and can better maintain their desired geometry after pyrolysis.

The decision of whether to use the DOD or FDM setup ultimately is determined by the viscosity of the build material solution. It was discussed that if the build material solution is a fluid, the DOD setup should be used, but if the build material solution is a cream-like substance, then the FDM setup should be used. It important to note that this does not take into account the quality of fabricated parts. If the quality of fabricated parts is a concern, which it almost always is in engineering applications, the suggestion of what build material solution and setup to use is effected.

Since the parts made with the DOD setup were unable to maintain their desired rectangular shape and had a significantly higher dimensional error than did the parts made with the FDM setup, it is suggested that one should exclusively use the FDM setup going forward since it is much more capable of producing parts with the desired geometry than is the DOD setup, which will become much more a factor as parts become geometrically complex.

In Section 3.2, microstructural analysis of the samples both before and after pyrolysis was pursued. It was determined that the microstructure of the fabricated samples is mainly made up of TiB_2 particle inclusions within a matrix that is either PCP (before pyrolysis) or its pyrolyzed product. From the EDS analyses, it was seen that the inclusions also obtained the element N, which comes from the reaction of the TiB_2 particles with the N_2 atmosphere during pyrolysis. Also from EDS, it was evident that a

consequence of the ball milling procedure is Zr contamination within the microstructure. Additionally, a particle size analysis study was executed, which showed that as the ball milling time was increased, the concentration of smaller-sized particles increased, which led to a decrease in the average particle size. The particle size analysis also showed that the TiB_2 particles expand during pyrolysis, thus confirming their status as active fillers. To determine the type of bonds that make up the microstructure, XPS was performed. For the most part, the results of XPS fell in line with what was seen with the EDS analyses, with the microstructure consisting of bonds made up of a combination of Ti, B, or N or a combination of Si, O, or C.

In Section 3.3, nanoindentation was used to determine the Young's modulus and hardness of the material. It was seen that the volume fraction of TiB_2 did not have much of an effect on the Young's modulus of the pyrolyzed material with the modulus only ranging from 118.26 – 126.85 GPa. Nanoindentation tests also showed that fabricated parts experience a significant increase in both modulus and hardness during pyrolysis. In order to measure the fracture toughness of the final ceramic, pyrolyzed samples were indented using a Vickers pyramidal indenter tip. This resulted in samples having a fracture toughness ranging from about 3 – 5 $MPa\sqrt{m}$, which is comparable to that of common engineering ceramics as well as other pyrolyzed PCP/filler products[96]. Additionally, it was determined that as the volume fraction of TiB_2 increases, the fracture toughness increases.

In Section 3.4, a discussion of the different toughening mechanisms that are at work took place. It was shown how crack deflection, secondary phase toughening, and elastic heterogeneity all help to increase the fracture toughness of the final ceramic. The nature

of these toughening mechanisms also proved how the increase in volume fraction of TiB_2 increases the fracture toughness of the material.

CHAPTER 4

TOUGHENING ENHANCEMENT

4.1 Addition of Carbon Nanofibers (CNFs)

As discussed in Chapter 3, compared to common engineering ceramics such as Alumina and Silicon Carbide, the ceramics fabricated using the prototype system shown in Chapter 2 has similar fracture toughness, ranging from approximately 3 – 5 MPa$\sqrt{\text{m}}$. This result is good in that it proves that the additive manufacturing method proposed here is capable of fabricating geometrically complex parts with relative ease with properties that are comparable to that of common engineering ceramics. On the other hand, one of the goals for this system is to offer the ability of fabricating ceramic parts that are tough enough to withstand extreme engineering environments such as high-efficiency jet engines and next-generation nuclear reactors, areas in which current engineering ceramics are too brittle to suffice. Therefore, the current build material solution for the prototype system will be unable to fabricate ceramics to endure these conditions. This causes the need for additional toughening enhancement of the PCP, more than that which can be provided by the addition of TiB_2 particles alone.

To offer additional toughening, carbon nanofibers (CNFs) were added to the build material solution. CNFs are known to be one of the strongest and toughest material's on the nanoscale, with fibers capable of having a Young's Modulus of 600 GPa.[98] By introducing CNFs into the build material solution, the fracture toughness of the final ceramic should certainly increase for the following reasons.

Since CNFs have such a high Young's modulus, much higher than that of both the pyrolyzed PCP and the expanded TiB_2 inclusions, the effective Young's modulus of the

final ceramic should increase, thus increasing the fracture toughness as well. Additionally, the inclusion of CNFs introduces a tertiary phase into the material. This will cause even more crack deflection than there was previously, which further impedes crack propagation, causing the fracture toughness to increase. Unlike with the addition of TiB_2 filler particles, the addition of CNFs causes crack bridging to occur. When a macroscopic crack is initiated within the ceramic product, CNFs bridge the crack surface just behind the crack, therefore restraining the opening of the crack. This makes it more difficult for the crack to propagate, which means that a larger stress must be applied in order to cause failure, thus increasing the material's fracture toughness.

4.1.1 Build Material Production

In order to properly examine the effect of CNFs on the pyrolyzed product, two types of build material solutions were made, each with a different concentration of CNFs. Concentrations of 0.4wt% and 0.85wt% CNF were chosen because research has shown that the addition of as small as 1 – 5 vol% of CNFs has produced noticeable toughening within the final ceramic.[99, 100] It is important to note that concentrations of CNF here were minimized to ensure that parts maintain their near-net-shape capabilities. The concentrations of PCP, TiB_2, and catalyst were the same for both types.

4.1.1.1 0.4wt% CNF

This build material solution consisted of 7 g of PCP, 22.36 g of TiB_2, 0.070 g of catalyst, and 0.118 g of CNF (Sigma Aldrich Inc, St. Louis, MO, USA). This corresponds to a TiB_2 volume fraction of 0.414 and a 0.4wt% of CNF. It should be noted here that the volume fraction was determined only considering the PCP and TiB_2 particles. Since the

concentrations of catalyst and CNF are very small (< 1wt%), the error in the calculation of the volume fraction of TiB_2 is negligible. This applies to the 0.85wt% CNF solution as well. The preparation of this build material solution follows a similar procedure to what was used in the chapter 2. Once the TiB_2 particles have been added to the liquid PCP, the solution is ball-milled for approximately 45 minutes using Zr balls and a Zr container. Then, the solution is put into a vacuum chamber for approximately 30 minutes to degas the build material, getting rid of any air bubbles that might exist within the solution. Lastly, CNF and catalyst are added to the solution.

4.1.1.2 0.85wt% CNF

This build material solution consisted of 7 g of PCP, 22.36 g of TiB_2, 0.070 g of catalyst, and 0.252 g of CNF. This corresponds to a TiB_2 volume fraction of 0.414 and a 0.85wt% of CNF. The procedure for making this variant of the build material solution is exactly the same as it is for the 0.4wt% CNF build material solution.

4.2 Near-Net-Shape Characterization

4.2.1 0.4wt% CNF

Using the FDM setup of the prototype system (Figure 5), four samples were fabricated. Each sample was designed with the following parameters: a line width of 0.75 mm, a desired geometry of 11.625 mm x 15.375 mm, a nozzle diameter of 0.254 mm, an input pressure of 10 – 14 psi, and no negative pressure. The samples were pyrolyzed in the kiln using the temperature-time profile presented in Figure 6.

Figure 35(a) and Figure 35(b) represent pictures of the samples taken before and after pyrolysis, respectively. By observing Figure 35(a), one sees that the pre-pyrolyzed

version of sample 1 has a large bubble on its top surface. This is due to air bubbles being trapped inside the build material, which can be avoided in the future with increased degassing time. Also, from observation of Figure 35, it is clear that fabricated parts tend to have the desired rectangular shape and seem to main their geometry throughout pyrolysis.

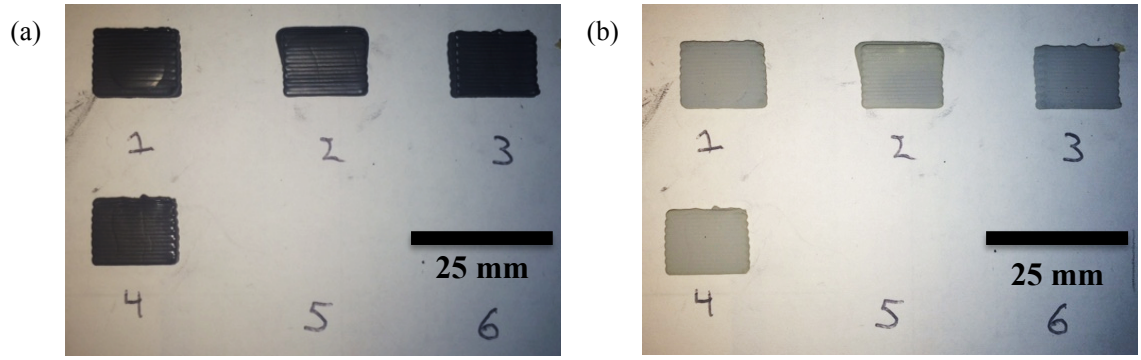

Figure 35: Pictures of samples fabricated using a build material solution that has a TiB_2 volume fraction of 0.414 and a CNF weight percentage of 0.4%.

The length and width measured for each sample before and after pyrolysis along with the associated shrinkage and error are presented in Table 7. The resulting average volume shrinkage and average linear dimensional error were 9.58 ± 2.83% and 2.44 ± 1.57%, respectively.

Table 7: Dimensional Measurements of Samples Before and After Pyrolysis With 0.40wt% CNF

Dimension ID	Pre-Pyrolyzed Sample (mm)	Pyrolyzed Sample (mm)	Percent Shrinkage (%)	Percent Error After Pyrolysis (%)
Sample 1 Width	16.04	15.72	2.02	2.23
Sample 1 Length	12.64	12.19	3.57	4.84
Sample 2 Width	15.19	14.58	4.03	5.17
Sample 2 Length	12.52	11.96	4.46	2.88
Sample 3 Width	16.04	15.26	4.86	0.73
Sample 3 Length	11.79	11.50	2.41	1.04
Sample 4 Width	15.68	15.26	2.65	0.73
Sample 4 Length	12.03	11.85	1.54	1.90

4.2.2 0.85wt% CNF

Using the FDM setup, four samples were fabricated. Each sample was designed with the following parameters: a line width of 0.75 mm, a desired geometry of 11.625 mm x 15.375 mm, a nozzle diameter of 0.254 mm, an input pressure of 22.0 psi, and a negative pressure of 19.9 in H_2O. The samples were pyrolyzed in the kiln using the temperature-time profile presented in Figure 6.

Figure 36 represents pictures of the samples taken before and after pyrolysis. By observing Figure 36(a), one sees that the pre-pyrolyzed version of samples 2 and 4 each have a large bubble on their top surface, which as stated before, is due to the presence of air bubbles within the build material solution. Like with the 0.4wt% CNF samples, these samples seem to have the desired rectangular geometry both before and after pyrolysis.

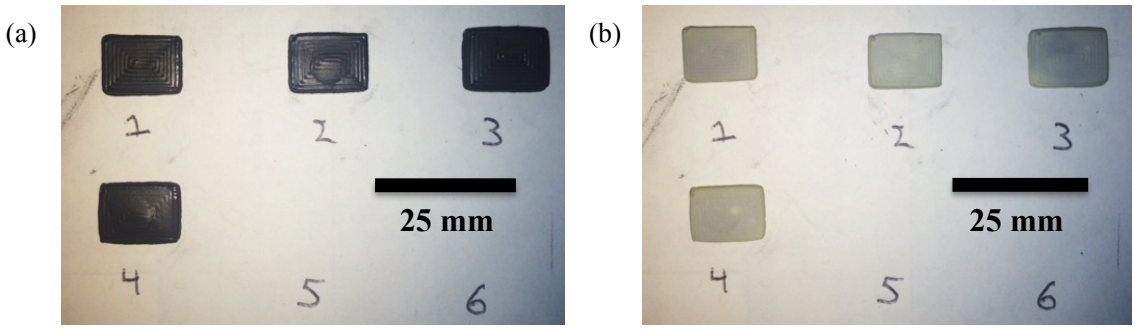

Figure 36: Pictures of samples fabricated using a build material solution that has a TiB_2 volume fraction of 0.414 and a CNF weight percentage of 0.85%.

The measured length and width for each sample before and after pyrolysis along with the associated shrinkage and error are presented in Table 8. The resulting average volume shrinkage and average linear dimensional error were 10.94 ± 3.05% and 6.39 ± 3.88%, respectively.

Table 8: Dimensional Measurements of Samples Before and After Pyrolysis With 0.85wt% CNF

Dimension ID	Pre-Pyrolyzed Sample (mm)	Pyrolyzed Sample (mm)	Percent Shrinkage (%)	Percent Error After Pyrolysis (%)
Sample 1 Width	14.69	14.14	3.72	8.03
Sample 1 Length	10.95	10.61	3.19	8.77
Sample 2 Width	14.57	14.14	2.92	8.03
Sample 2 Length	11.07	10.47	5.42	9.90
Sample 3 Width	16.01	15.32	4.32	0.37
Sample 3 Length	11.56	11.52	0.30	0.89
Sample 4 Width	15.17	14.40	5.05	6.33
Sample 4 Length	11.07	10.61	4.24	8.77

4.2.3 Volume Shrinkage and Dimensional Error

To analyze the effect of CNFs on the volume shrinkage experienced during pyrolysis, a plot was made of the volume shrinkage as a function of the concentration of CNF for samples having a TiB_2 volume fraction of 0.414 (Figure 37). This plot shows a noticeable decrease in volume shrinkage when going from no CNF to 0.4wt% CNF and a slight increase when going from 0.4wt% CNF to 0.85wt% CNF. This indicates that the presence of CNFs might have an effect on the volume shrinkage whereas the concentration of CNFs might not. Ideally, one would think that the addition of CNF would act as an additional roadblock to impede the shrinkage of the PCP during pyrolysis, therefore causing the volume shrinkage to decrease but that does not seem be the case according to the plot shown in Figure 37.

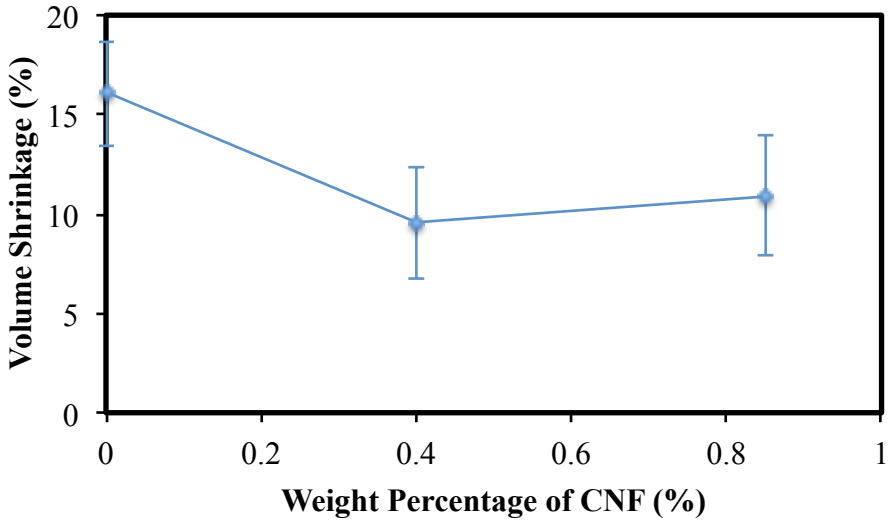

Figure 37: Plot of the average volume shrinkage experienced by the samples during pyrolysis as a function of the concentration of CNFs within the starting build material solution.

Going forward, it is suggested that parts be fabricated at several different concentrations of CNF in order to better understand the effect, if any, that the concentration of CNFs have on the volume shrinkage.

Although the effect that CNFs have on the volume shrinkage is difficult to determine from Figure 37, it important to note that the volume shrinkage experienced by the samples with CNFs is relatively low being around 10% for both types of samples (0.4wt% and 0.85wt% CNF). Therefore, these samples still show much better near-net-shape capabilities compared to the work of Gaytan et al.[85] and Shahzad et al.[86], in which fabricated ceramics experienced volume shrinkage of approximately 60 – 90%. Also, it was seen earlier that the dimensional error experience by these two types of samples was low as well with the 0.4wt% CNF samples having an average linear dimensional error of 2.44 ± 1.57% and the 0.85wt% CNF samples having an average linear dimensional error of 6.39 ± 3.88%.

4.3 Microstructural Characterization

4.3.1 0.4wt% CNF

After taking images of the pyrolyzed samples for the near-net-shape analysis, samples were cut and polished in order to perform microstructural characterization via SEM, EDS, and XPS. It should be noted that samples were polished on 120 grit, 400 grit, and 600 grit paper as well as on polishing cloth in conjunction with 50-nm colloidal silica. Also, unless other wise stated, the polishing procedure is consistent with what is discussed here going forward.

4.3.1.1 SEM Imaging

In order to gain a better sense of what the microstructure looked like, SEM images were taken of the polished surface of a pyrolyzed sample as shown in Figure 38.

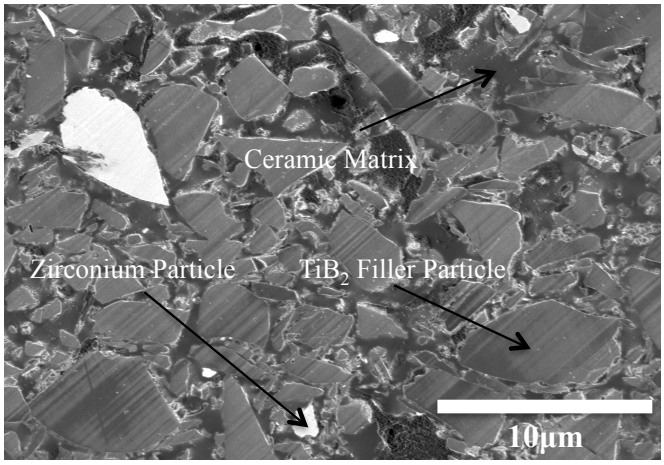

Figure 38: SEM image of a polished surface of a pyrolyzed sample with a TiB_2 volume fraction of 0.414 and 0.4 wt% CNF.

An observation of Figure 38 indicates that the 0.4wt% CNF samples have a similar microstructure to that of the samples without CNF that have a TiB_2 volume fraction of

0.414 (Figure 21). This makes sense since the only difference in the build material between these two types of samples is the presence of CNFs.

Like with Figure 21, here it is evident that the microstructure consists of inclusions within a matrix. Also, there is some Zr contamination as seen with the presence of bright luminescent particles in Figure 38. Another key observation here is that there seems to be no presence of CNF. A possibility for this occurrence is that the polishing of the surface causes only the heads of the CNFs to be exposed. Since CNFs only have a diameter of approximately 200 nm, CNFs would only look like tiny dots in the SEM images of the polished surface, making it very difficult to confirm the presence of CNFs within these samples. Therefore, an unpolished cross-section of a pyrolyzed sample was used for SEM analysis.

Figure 39 and Figure 40 represent SEM images of the cross-section of an unpolished 0.4wt% CNF pyrolyzed sample. Observation of both these figures provides evidence of the presence of CNFs within the microstructure. It is important to note that Figure 39 represents a more realistic view of what the CNFs distribution is like throughout the entire sample whereas Figure 40 shows that there are some areas with a large accumulation of CNFs. Large bundles of CNFs are typically viewed as a disadvantage since they an indicator of poor dispersion of CNFs throughout the microstructure. This will lead to areas without CNF and therefore lower fracture toughness than what would be seen with a sample with well-dispersed CNFs.

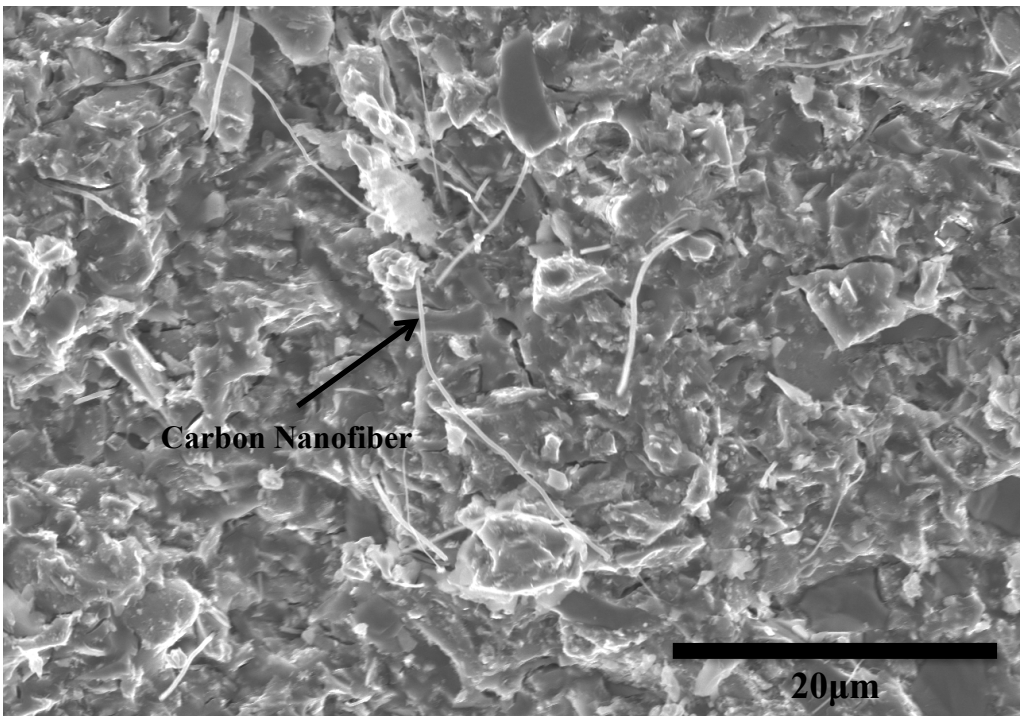

Figure 39: SEM image an unpolished cross-section of one of the samples that was fabricated using 0.4 wt% CNF.

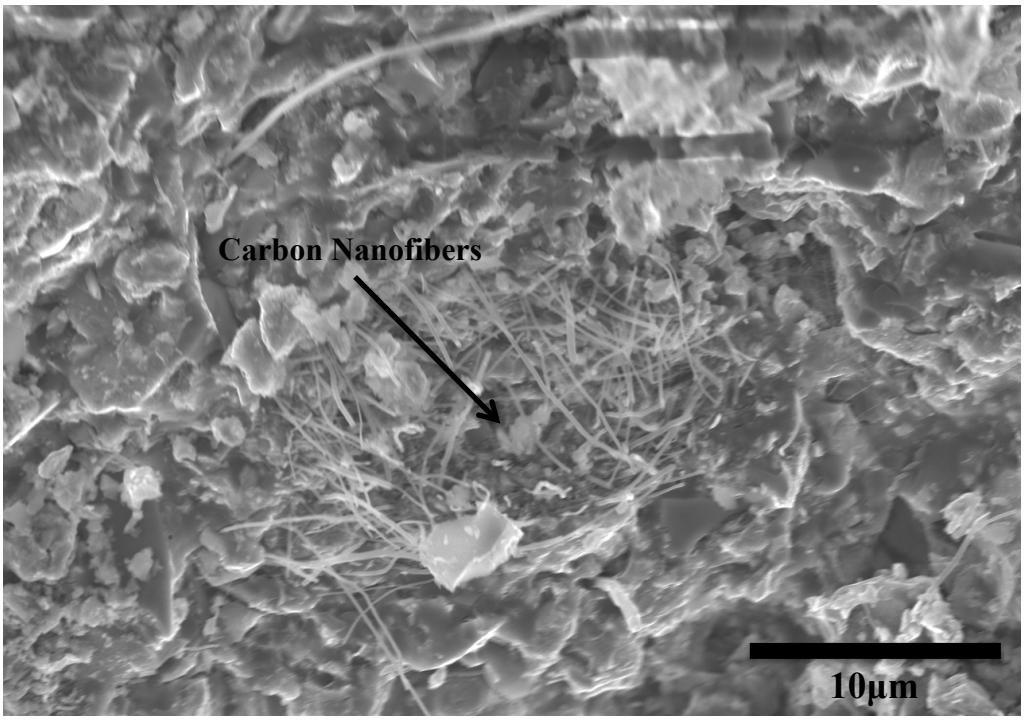

Figure 40: SEM image an unpolished cross-section of one of the samples that was fabricated using 0.4 wt% CNF that emphasizes the possibility of having large bundles of CNFs within the microstructure.

4.3.1.2 EDS Analysis

In order to determine what elements make up the microstructure, an EDS analysis was executed on the polished surface of a pyrolyzed sample, the results of which are represented by the EDS mappings shown in Figure 41.

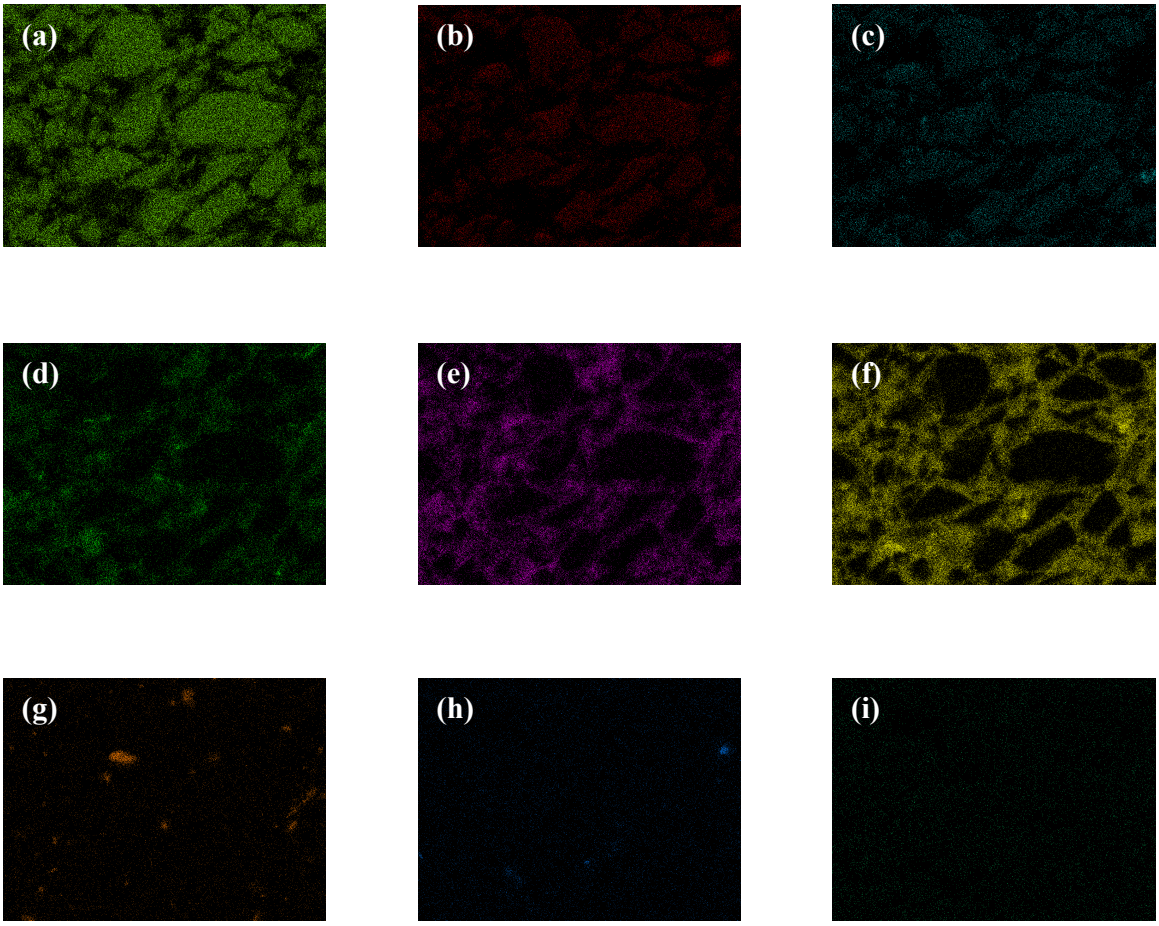

Figure 41: EDS mappings resulting from the EDS analysis done on the area with a similar microstructure to that which is shown in Figure 38. The elements shown in the EDS mappings are (a) Ti, (b) B, (c) N, (d) C, (e) O, (f) Si, (g) Zr, (h) Al, and (i) Na.

Like what was seen in Chapter 3 with samples without CNF, an observation of Figure 41 makes it clear that the inclusions consist of Ti, B, and N and the matrix material consists of Si, O, and C. This indicates that the inclusions are the expanded TiB_2 particles and that

the matrix is the pyrolyzed version of the PCP. Also from Figure 41, it is clear that the microstructure has some Zr contamination, which is a consequence of the ball milling procedure. Additionally, an observation of Figure 41 shows that the EDS analysis resulted in the EDS mappings of Aluminum (Al) and Sodium (Na). Since the EDS mapping of Na indicates a very low, well-distributed presence of Na, it is safe to assume that the mapping of Na is the result of background noise. On the other hand, the EDS mapping of Al shows regions of noticeable concentrations of Al within the microstructure and can therefore, not be treated as the result of background noise. This is unexpected since the procedure for creating the build material does not include the use of Al. It is also unclear where this Al contamination came from because the only element that should show up as contamination is Zr because of the ball milling procedure. Fortunately, from the EDS mapping of Al, is it evident that the Al contamination within the microstructure is very low, with only a few locations having any significant presence of Al. Therefore, the effect of this Al contamination on the overall material properties of the sample should be negligible.

4.3.2 0.85wt% CNF

After taking images of the pyrolyzed samples for the near-net-shape analysis, samples were cut and polished in order to perform microstructural characterization via SEM.

4.3.2.1 SEM Imaging

SEM images of the polished surface of a pyrolyzed sample were taken as shown in Figure 42. An observation of Figure 42 indicates that the 0.85wt% CNF samples have

a similar microstructure to that of the samples with 0.4wt% CNF. Like with the 0.4wt% CNF sample that underwent SEM imaging, it is evident that the microstructure consists of inclusions within a matrix. Also, there is some Zr contamination as indicated by the presence of bright luminescent particles in Figure 42.

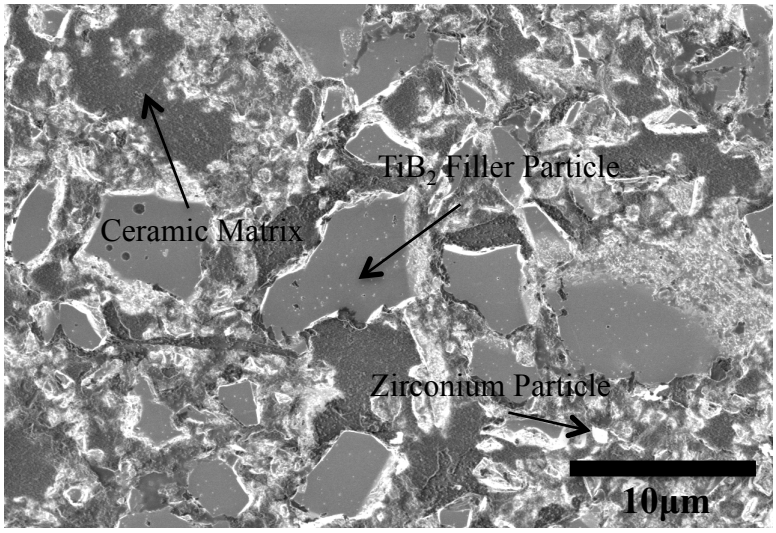

Figure 42: SEM image of the microstructure of a pyrolyzed sample with 0.85 wt% CNF.

Another observation to take note of here is that the matrix material looks rougher for this sample than it did for the 0.4wt% CNF sample (Figure 38). The matrix material also has areas of bright gray-colored regions unlike what was seen within the matrix material of the 0.4wt% CNF sample. Both of these occur due to the fact that although both samples went through the same polishing procedure, the 0.4wt% CNF sample had a better surface finish than did the 0.85wt% CNF sample. Like with the SEM image of the 0.4wt% CNF sample (Figure 38), one is unable to locate the presence of CNFs from Figure 42. But, since the microstructure is similar to that seen in Figure 38, it was deemed unnecessary to take SEM images of the unpolished cross-section of these samples in order to confirm the

presence of CNFs within the microstructure. Additionally, since the microstructure of the pyrolyzed samples is fairly consistent throughout all build material variants (both with and without CNF), it was unnecessary to perform EDS on these samples to show that the inclusions represent the expanded TiB_2 filler particles and that the matrix material is the pyrolyzed version of the starting PCP.

4.3.3 XPS Analysis

In order to see what type of bonds that were present within the microstructure of the pyrolyzed samples made using the build material solutions containing CNFs, XPS was executed on a polished and etched surface of a pyrolyzed 0.4wt% CNF sample. The resulting plot of counts/s as a function of the binding energy is shown in Figure 43.

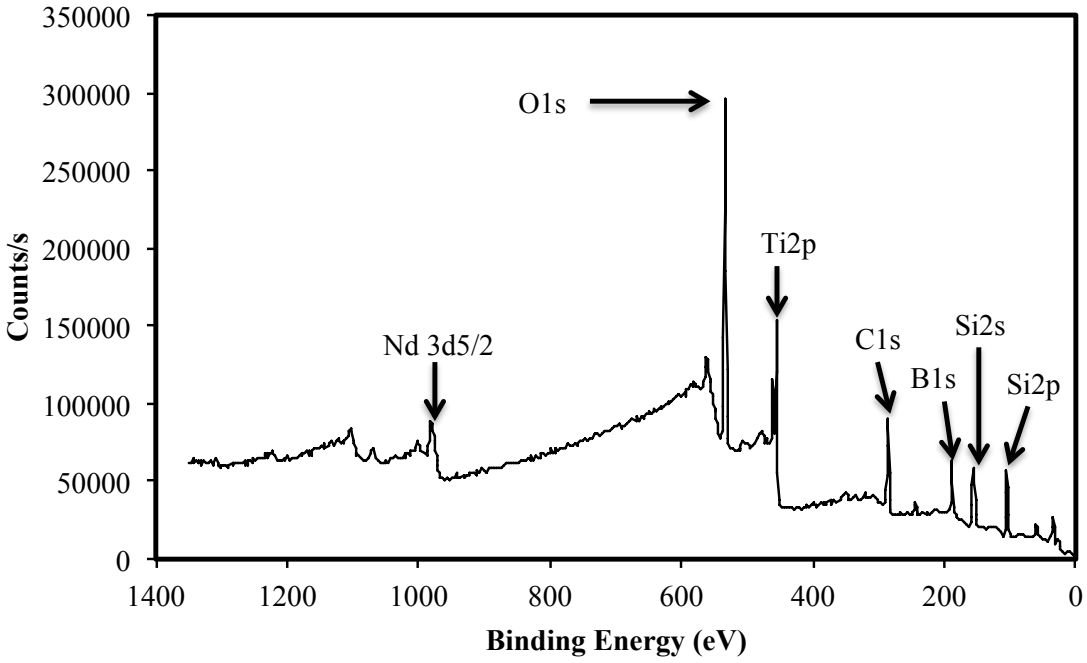

Figure 43: XPS result for a pyrolyzed 0.4wt% CNF sample.

From previous work from other researchers[87, 89-91, 101] as well as the previous XPS analysis that was done on a pyrolyzed sample that does not contain CNFs (Figure 25), the peaks within the plot were able to be determined along with their associated bonds, which are listed in Table 9.

Table 9: XPS Peak Assignment for a Pyrolyzed Sample with CNF

Element	Peak Position (eV)	Bond
Nd3d5/2	980.85	Neodymium (Nd) [90]
O1s	533.0	Silica (SiO_2)[91]
Ti2p	455.3	Titanium nitride (TiN)[87]
C1s	284.6	Silicon oxycarbide, graphitic or "adventitious" carbon[91]
B1s	187.5	Titanium diboride (TiB_2)[89]
Si2s	155.3	Silicon(IV) dioxide (Quartz)[101]
Si2p	101.7	Silicon oxycarbide[91]

From Table 9, it is clear that the XPS analysis indicates that the compounds that make up the microstructure of the pyrolyzed samples are Nd, SiO_2, TiN, Silicon oxycarbide, graphitic or "adventitious" carbon, TiB_2, and quartz. Except for the presence of quartz, this behavior is reflected by the XPS analysis done on a pyrolyzed sample without CNF that was discussed in Chapter 3. This is expected since the only difference in the microstructure between the two samples is the presence of CNFs, which are made up of C-C bonds. Also, since the surface used for XPS was polished, it is likely that the presence of CNFs cannot be detected due to the fact that the presence of CNFs within the microstructure could not be confirmed when taking SEM images of the polished surface as seen in Figure 38.

Like with the XPS analysis discussed in Chapter 3, the only result from this XPS analysis that does not make sense is the peak seen at 980.85 eV, which corresponds to the presence of Nd. But with this XPS analysis, the plot in Figure 43 gives a better indication of the reasoning behind the presence of Nd. Since in Figure 43, it is evident that the peak at 980.85 eV is significantly less than all the other peaks and the noise surrounding the peak has only slightly less amplitude than the peak itself, it is safe to assume that the peak at 980.85 eV can be attributed to noise within the XPS data more than anything else.

4.4 Mechanical Property Characterization

4.4.1 Young's Modulus Measurement

In order to obtain a measurement of the Young's modulus for the final ceramic product, a nanoindentation test was performed on a pyrolyzed 0.4wt% CNF sample with the following parameters: a cubic-corner tip geometry, a grid size of 17 points x 17 points (289 points in total) covering a 48 μm x 48 μm area, and an indentation force of 2000 μN. It important to note here that no nanoindentation test was performed on a pyrolyzed 0.85wt% CNF sample. This is because the difference in concentration of CNF is so small (only 0.45wt%) that the effect of the added concentration of CNF on overall modulus of the sample should be negligible. Therefore, it was assumed that the samples with 0.85wt% CNF have the same Young's modulus as do the samples with 0.4wt% CNF.

From the nanoindentation test, it was determined that the CNF samples had an average reduced modulus of 141.46 GPa. By setting E_r to the average reduced modulus and plugging in the values, 862.5, 0.20, and 0.25 for E_i, ν_i, and ν, respectively into equation (13), Young's modulus was calculated to be 157.40 GPa.

4.4.2 Fracture Toughness Measurement

Using the same indenter and parameters used for the fracture toughness measurements discussed in Chapter 3, fracture toughness measurements were made on the samples with CNF. After making a number of indents on both types of samples, SEM images were taken in order to measure the indent size and characteristic crack length for each indent. Then, equation (14) and equation (15) were used in order to calculate the fracture toughness and hardness associated with each indent, respectively. It is important remember that for each calculation, a value of 157.40 was used for E in equation (14) since the Young's modulus was determined to be 157.40 GPa for all samples containing CNF. The fracture toughness and hardness measurement for indents having the same CNF concentration as one another were averaged together in order to determine the average fracture toughness and hardness for each build material solution, respectively.

Figure 44 and Figure 45 represent plots of the fracture toughness and hardness as a function of the weight percentage of CNF within the starting build material solution, respectively. From observing Figure 44 and Figure 45, it is clear that as the concentration of CNF is increased from 0 to 0.4wt%, both the fracture toughness and hardness suffer a significant drop. As the concentration of CNF is further increased to 0.85wt%, both the fracture toughness and the hardness increase, with the fracture toughness exceeding and the hardness being very similar to that of the samples with no CNF. This was unexpected behavior because the addition of CNFs into the build solution should ideally increase the fracture toughness and hardness of the final ceramic as the concentration of CNFs is increased since CNFs have higher fracture toughness and hardness than both the TiB_2 particles and the pyrolyzed PCP. Therefore, as the concentration of CNFs is increased, so

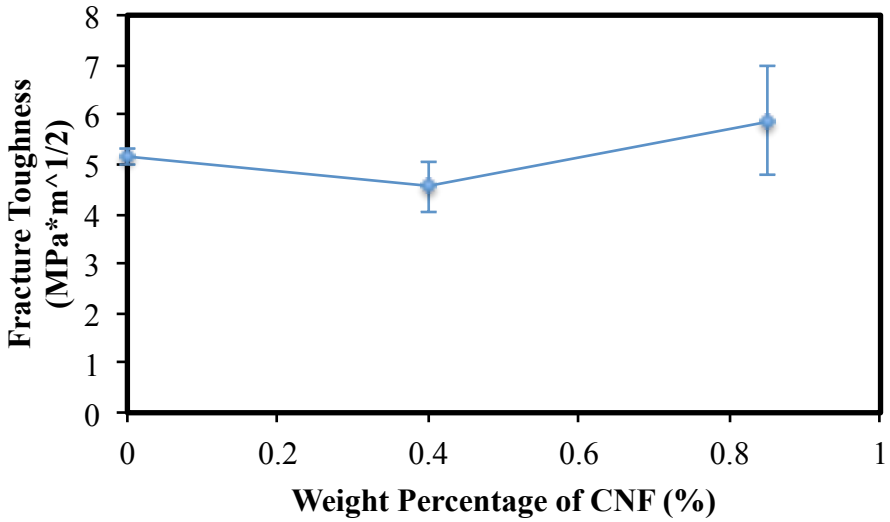

Figure 44: Plot of the fracture toughness vs. weight percentage of CNF within the starting build material solution

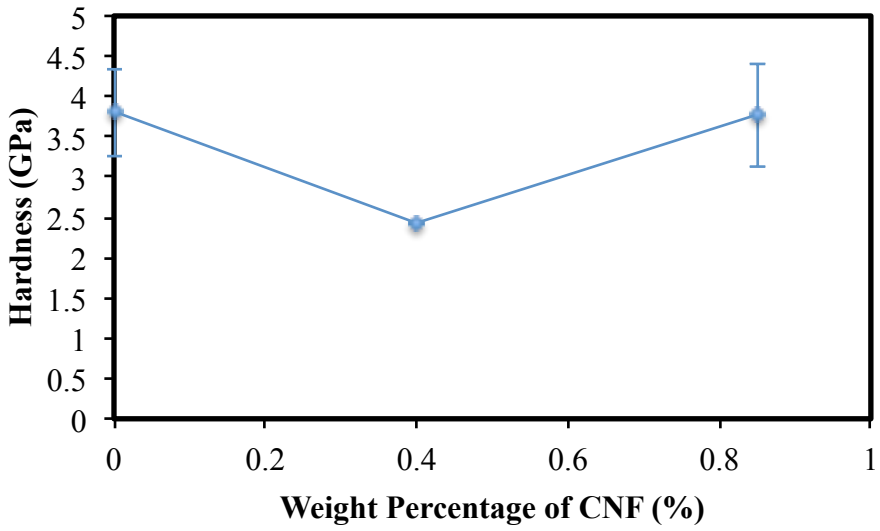

Figure 45: Plot of the hardness vs. weight percentage of CNF within the starting build material solution.

too should the fracture toughness and hardness, which is something that was not observed with the transition from no CNF to 0.4wt% CNF. A possible reason for this occurrence could be the quality of dispersion of CNFs within the build material solution. In Figure

40, it was observed that large bundles of CNFs were present within the microstructure of the 0.4wt% CNF sample, indicating the presence of poorly dispersed CNFs. This means that it was possible that indentation occurred in an area with no CNFs present, therefore explaining why no increase in either fracture toughness or hardness was seen when going from 0 to 0.4wt% CNF. The decrease in both of these properties could be due to poor dispersion of the TiB_2 particles within the microstructure, which would cause areas of lower fracture toughness and hardness than expected. Ultimately, it is seems that further testing needs to be done with build material solutions with even higher concentrations of CNF to ensure that the fracture toughness and hardness continue to increase as the concentration of CNF increases.

4.5 Conclusions

In Section 4.1, it was suggested that CNFs be added to the build material solution in order to increase the fracture toughness of fabricated parts. This is because they are known to be one of the toughest and strongest materials on the nanoscale. Additionally, it was shown that the addition of CNFs increase fracture toughness of the fabricated parts by crack bridging as well as adding a tertiary phase into the microstructure, which increases crack deflection.

In Section 4.2, the volume shrinkage and dimensional error of the CNF samples were determined and compared to that of a sample without CNF but made with the same volume fraction of TiB_2 as were the CNF samples. The presence of CNF seemed to have caused some noticeable decrease in the amount of volume shrinkage experienced during pyrolysis but the concentration of CNF seemed not to have much an effect. What the concentration did effect though was the amount of dimensional error. As the

concentration of CNF increased, so too did the dimensional error. Since the average dimensional error never was above 6.39%, dimensional error should not play too much of a role when considering what concentration of CNF to use if the concentration is below 0.85wt%. Since the volume shrinkage and dimensional error were determined at only two weight concentrations of CNF, it is suggested that samples made at different weight concentrations be tested to confirm the observed trends.

In Section 4.3, the microstructure of pyrolyzed samples made with CNFs was analyzed via SEM, EDS, and XPS. The SEM images of the polished surface indicated a similar microstructure to that of which was seen in the samples without CNF. On the other hand, SEM images of the unpolished cross-section confirm the presence of CNFs within the microstructure. EDS and XPS provided very similar results to what was seen with the samples without CNF. This is expected because the only difference in the microstructure is the presence of the C-C bonds that make up CNFs.

In Section 4.4, the material properties of pyrolyzed CNF samples were analyzed. The Young's modulus of the CNF samples was calculated to be 157.40 GPa, which is approximately 30 GPa larger than what was seen in the samples without CNF. This was expected behavior since the higher Young's modulus of CNF as compared to that of TiB_2 and PCP will cause the effective modulus to increase. Fracture toughness and hardness were plotted as a function of the weight percentage of CNF. These plots indicated that when the amount of CNF was increased from 0 to 0.4wt%, both the fracture toughness and hardness decreased, but as the amount of CNF was further increased to 0.85wt%, the fracture toughness and hardness increased. A possible reason for the drop in fracture toughness at 0.4wt% CNF was poor dispersion of CNFs and TiB_2 within the

microstructure. It is suggested that more fracture toughness and hardness measurements be done at different concentrations of CNF to get a better sense of the trend the fracture toughness and hardness have with the concentration of CNF. Since at a concentration of 0.85wt% CNF, the fracture toughness was almost 1 MPa$\sqrt{m}$ higher than it was at 0wt% CNF, the addition of CNFs into the build material indicates the capability of allowing the prototype system to produce parts with increased fracture toughness. This also suggests that as concentration of CNF is even further increased, the fracture toughness will continue to increase, possibly to the point at which fabricated parts will be tough enough to serve their intended purpose. Unfortunately, this behavior cannot be confirmed until samples of higher concentrations can be tested.

CHAPTER 5

CONCLUDING REMARKS AND FUTURE WORK

5.1 Concluding Remarks

In this thesis, a new additive manufacturing method was proposed in order to enable the fabrication of ultra-tough ceramics to serve in extreme engineering environments such as high-efficiency jet engines, armor ceramics[30], and next-generation nuclear reactors. A prototype system of the proposed method was developed. The prototype system shows the multi-functionality of the proposed method, which by its use of both DOD and FDM, is capable of working in conjunction with a wide variety of build materials. The prototype system was also capable of producing parts with desired geometry as well as geometric complexity. Material property characterization of fabricated ceramic samples indicates the capability of the proposed method to produce ceramic parts with equivalent fracture toughness to that of common engineering ceramics as well as other pyrolyzed PCP/filler products. The addition of CNFs into the build material shows that the fracture toughness of ceramics made with the proposed method can be further increased. This is a promising result that proves that with further increase of the concentration of CNFs within the build material, the production of ultra-tough ceramics is possible.

5.2 Recommendations for Future Work

The present work serves as a proof-of-concept of the proposed method. There is still a lot that needs to be done to obtain a full realization of the proposed method. One major area that needs to be addressed is the build material.

Since the samples without CNF experienced a significant amount of volume shrinkage once the volume fraction of TiB_2 was increased past 0.331, the point at which samples should theoretically experience no volume shrinkage, as opposed to volume expansion which is what is expected based off equation (3), it is suggested that more samples be tested at different volume fractions of TiB_2 that are greater than 0.331. This way, one can see whether the samples fabricated at a TiB_2 volume fraction of 0.414 represent an outlier in the data set. Also, since 0.414 was the only volume fraction of TiB_2 that did not show the expected inversely proportional relationship between fracture toughness and hardness, these further tests will be used to determine whether this behavior is due to enhanced porosity taking effect. Additionally, this can serve to pinpoint the maximum volume fraction of TiB_2 that can be added to the build material solution before enhanced porosity takes place, thus causing final ceramics to lose their structural integrity.

By comparing the material properties of fabricated samples to that of common engineering ceramics, it is clear that both the modulus and hardness of the final ceramic parts must be increased. To do this, the build material solution must be further manipulated. A possible suggestion is to replace the TiB_2 filler with a filler that will cause increased modulus and hardness as well as equivalent fracture toughness of the final ceramic compared to that associated with the fabricated samples of the present work. This will require additional research to see what filler will be able to produce this desired result.

In addition to increased modulus and hardness, the build material solution should also be further manipulated so as to better ensure near-net-shape production of final

ceramics as a result of pyrolysis. With the build material in its current state, the TiB_2 filler particles must react with the N_2 atmosphere in order to expand, which means that one has to rely on the diffusion of the N_2 gas into the PCP during pyrolysis. Since this diffusion is difficult to monitor, one is left unsure whether the appropriate reaction between the filler particles and N_2 take place. Therefore, it is suggested that an additional material be added to the PCP matrix that serves to react with TiB_2 filler particles during pyrolysis in order to produce near-net-shape ceramics. This will ensure that particle expansion will occur during pyrolysis even if N_2 diffusion into the PCP is unable to occur, thus aiding in the production of a near-net-shape ceramic.

As for the samples with CNF, since only two different weight concentrations of CNF were tested, it is suggested that more testing be done at different concentrations of CNF in order to confirm the trends that were seen in the obtained data as well as to point out any outliers within the data.

The present work has shown that the build material, as it currently stands, is only capable of producing parts with fracture toughness similar to that of common engineering ceramics, materials that are still too brittle to withstand the type of environments for which parts made with the proposed method are purposed. Since the addition of 0.85wt% CNF into the build material shows that capability of achieving increased fracture toughness when compared to that of parts made without CNF, it is suggested that the concentration of CNF be further increased to investigate how much the fracture toughness can be increased without altering the method's near-net-shape capability.

Since parts made with the prototype system for actual engineering applications within the extreme-engineering environments they are purposed for will need to have

much larger dimensions than what was used for samples in the present work, adjustments to the current fabrication process has to be made. As fabricated parts increase in thickness, the part will begin to experience inhomogeneous heating, which consists of layers closer to the heating stage surface to heat up faster than the layers further away. This causes adverse effects to the fabricated part such as deviation from desired geometry as well insufficient inter-layer bonding, which will cause increased dimensional error and diminished structural integrity of the final ceramic, respectively. In order to remedy this possible problem, it is suggested that for parts made using several layers, that once a layer is deposited, it should be completely pre-cured before initiation deposition of the next layer.

Additionally, one should realize that the path used to deposit the build material into the desired geometry could have an effect on fabricated parts. Therefore, work should be done to see how different deposition paths effect parts made with the same desired geometry. From this work, one might be able to optimize the deposition path for specific geometries so as to maximize their near-net-shape capabilities, which could be very useful if done for part geometries that will be necessary to fabricate when using the proposed method for its intended application.

Another area that should be addressed is the fabrication time. With the current prototype system, it is required that fabricated parts be heated in a kiln for several hours in order to execute pyrolysis. Therefore, it is suggested that a CO_2 laser be placed within in the prototype system so that once a layer is deposited, the CO_2 laser can heat the layer up to the temperature necessary for the layer to go through pyrolysis within a matter of seconds. This process can then be repeated in a layer-by-layer process until the entire part

has been fabricated. Since the pyrolysis time is reduced from hours to seconds, this will significantly decrease the amount of time it takes to make a part, which will be necessary if the proposed method is to be used for mass production.

REFERENCES

1. Melchels, F.P.W., J. Feijen, and D.W. Grijpma, *A review on stereolithography and its applications in biomedical engineering.* Biomaterials, 2010. **31**(24): p. 6121-6130.

2. Gabbrielli, R., I.G. Turner, and C.R. Bowen, *Development of modelling methods for materials to be used as bone substitutes.* Key Engineering Materials, 2008. **361**: p. 903-906.

3. Mankovich, N., et al., *Surgical planning using 3- dimensional imaging and computer modelling.* Otolaryngol Clin North Am, 1994. **27**(5): p. 875-889.

4. Gross, B.C., et al., *Evaluation of 3d printing and its potential impact on biotechnology and the chemical sciences.* Analytical chemistry, 2014. **86**(7): p. 3240-3253.

5. Huang, Y.-M., S. Kuriyama, and C.-P. Jiang, Int. J. Adv. Manuf. Technol. , 2004. **24**: p. 361−369.

6. Ikuta, K. and K. Hirowatari. *In Micro Electro Mechanical Systems*. in *MEMS'93*. 1993. Fort Lauderdale, FL.

7. Takagi, T. and N. Nakajima. *In Micro Electro Mechanical Systems*. in *MEMS'93*. 1993. Fort Lauderdale, FL.

8. Harris, R.A., R.J.M. Hague, and P.M. Dickens, Int. J. Machine Tools Manuf., 2004. **44**: p. 59−64.

9. Wang, Y., et al., Lab Chip, 2011. **11**: p. 3089−3097.

10. Yan, X. and P. Gu, *A review of rapid prototyping technologies and systems.* Computer-Aided Design, 1996. **28**(4): p. 307-318.

11. Kruth, J.-P., *Material incress manufacturing by rapid prototyping techniques.* CIRP Annals-Manufacturing Technology, 1991. **40**(2): p. 603-614.

12. Deckard, C.R. and J.J. Beaman. *Recent advances in selective laser sintering*. in *Fourteenth Conference on Production Research and Technology*. 1987.

13. Deckard, C.R. and J.J. Beaman, *Solid freeform fabrication and selective powder sintering.* Proceedings of the 15th NAMRC-SME, Bethlehem, PA, 1987: p. 636-640.

14. Crump, S.S. *Fast, Precise, Safe Prototypes with FDM*. in *ASME Annual Winter Conference, Atlanta, December*. 1991.

15. Van Weeren, R., et al. in *Proceedings of the Solid Freeform Fabrication Symposium*. 1995. New York.

16. Zhong, W.H., et al., Mater. Sci. Eng. A: Struct., 2001. **301**: p. 125−130.

17. Agarwala, M., et al. in *Proceedings of Solid Freeform Fabrication Symposium*. 1996. University of Texas, Austin, TX.

18. Wu, G., et al., *Solid freeform fabrication of metal components using fused deposition of metals.* Materials & design, 2002. **23**(1): p. 97-105.

19. Bandyopadghyay, A., et al., Am. Ceram. Soc. , 2005. **80**: p. 1366−1372.

20. Bellini, A., *Fused deposition of ceramics: A comprehensive experimental, analytical and computational study of material behavior, fabrication process and equipment design*. 2002, Drexel University: Ann Arbor, MI.

21. Jafari, M.A., et al., Rapid Prototyp. J. , 2000. **6**: p. 161−174.

22. Zein, I., et al., *Fused deposition modeling of novel scaffold architectures for tissue engineering applications.* Biomaterials, 2002. **23**(4): p. 1169-1185.

23. Dutta, D., et al., *Layered manufacturing: current status and future trends.* Journal of Computing and Information Science in Engineering, 2001. **1**(1): p. 60-71.

24. Frank, M.C., F.E. Peters, and R. Karthikeyan. in *24th Annual International Solid Freeform Fabrication Symposium−An Additive Manufacturing Conference*. 2010. University of Texas at Austin, Austin, TX.

25. Mueller, B. and D. Kochan, *Laminated object manufacturing for rapid tooling and patternmaking in foundry industry.* Computers in Industry, 1999. **39**(1): p. 47-53.

26. Flach, L., et al. in *Solid Freeform Fabrication Symposium Proceedings*. 1998. University of Texas at Austin, Austin, TX.

27. Wohlers, I., *Make fiction fact fast.* Man & Engng, 1991. **106**(3): p. 44-49.

28. Doraiswamy, A., et al., *Inkjet printing of bioadhesives.* Journal of Biomedical Materials Research Part B: Applied Biomaterials, 2009. **89**(1): p. 28-35.

29. de Gans, B.J., P.C. Duineveld, and U.S. Schubert, *Inkjet printing of polymers: state of the art and future developments.* Advanced materials, 2004. **16**(3): p. 203-213.

30. Hu, G., J. Mech. Phys. Solids, 2011. **59**: p. 1076-1093.

31. *Dynamic Ceramic Manufacture and Processing of Engineering Ceramics - Pressing - Maching - Grinding | Dynamic Ceramic*. [cited 2015 March 17th]; Available from: http://www.dynacer.com/processing/.

32. Agarwala, M., et al., *Solid freeform fabrication methods*. 1998, Google Patents.

33. Bellini, A., L. Shor, and S.I. Guceri, *New developments in fused deposition modeling of ceramics.* Rapid Prototyping Journal, 2005. **11**(4): p. 214-220.

34. Calvert, P., *Inkjet printing for materials and devices.* Chemistry of materials, 2001. **13**(10): p. 3299-3305.

35. Grida, I. and J.R.G. Evans, *Extrusion freeforming of ceramics through fine nozzles.* Journal of the European Ceramic Society, 2003. **23**(5): p. 629-635.

36. Karapatis, N.P., J.P.S. Van Griethuysen, and R. Glardon, *Direct rapid tooling: a review of current research.* Rapid Prototyping Journal, 1998. **4**(2): p. 77-89.

37. Lous, G.M., et al., *Fabrication of piezoelectric ceramic/polymer composite transducers using fused deposition of ceramics.* Journal of the American Ceramic Society, 2000. **83**(1): p. 124-28.

38. Omatete, O.O., M.A. Janney, and S.D. Nunn, *Gelcasting: from laboratory development toward industrial production.* Journal of the European Ceramic Society, 1997. **17**(2): p. 407-413.

39. Sukeshini, A.M., et al., *Aerosol jet printing and microstructure of SOFC electrolyte and cathode layers.* ECS Transactions, 2011. **35**(1): p. 2151-2160.

40. Wätjen, A.M., et al., *Novel Prospects and Possibilities in Additive Manufacturing of Ceramics by means of Direct Inkjet Printing.* Advances in Mechanical Engineering, 2014. **2014**.

41. Tiller, F.M. and C.D. Tsai, *Theory of filtration of ceramics: I, slip casting.* Journal of the American Ceramic Society, 1986. **69**(12): p. 882-887.

42. Richerson, D., *Modern ceramic engineering: properties, processing, and use in design*. 2005: CRC press.

43. Händle, F., *Extrusion in ceramics*. 2007: Springer.

44. Oberg, E., et al., *Machinery's Handbook (26th ed.)*. New York: Industrial Press.

45. Hotza, D. and P. Greil, *Review: aqueous tape casting of ceramic powders.* Materials Science and Engineering: A, 1995. **202**(1): p. 206-217.

46. Medvedovski, E. and M. Peltsman, *Low pressure injection moulding mass production technology of complex shape advanced ceramic components.* Advances in Applied Ceramics, 2012. **111**(5&6): p. 333-344.

47. German, R.M., *AZ of powder metallurgy*. 2005: Elsevier Science Ltd.

48. Helle, A.S., K.E. Easterling, and M.F. Ashby, *Hot-isostatic pressing diagrams: new developments.* Acta Metallurgica, 1985. **33**(12): p. 2163-2174.

49. Uhland, S.A., et al., Mater. Res. Soc. Symp. Proc. , 1999. **542**(Solid Freeform and Additive Fabrication): p. 153-158.

50. Blazdell, P.F., et al., *The computer aided manufacture of ceramics using multilayer jet printing.* Journal of Materials Science Letters, 1995. **14**(22): p. 1562-1565.

51. Mott, M., J.H. Song, and J.R.G. Evans, *Microengineering of Ceramics by Direct Ink‐Jet Printing.* Journal of the American Ceramic Society, 1999. **82**(7): p. 1653-1658.

52. Slade, C.E. and J.R.G. Evans, J.Mater.Sci.Lett., 1998. **17**: p. 1669-1671.

53. Song, J.H., M.J. Edirisinghe, and J.R.G. Evans, *Formulation and multilayer jet printing of ceramic inks.* Journal of the American Ceramic Society, 1999. **82**(12): p. 3374-3380.

54. Bellini, A. and S. Güçeri, *Mechanical characterization of parts fabricated using fused deposition modeling.* Rapid Prototyping Journal, 2003. **9**(4): p. 252-264.

55. Bellini, A., et al. *Nozzle shape, road cross section and space filling in FDM/SFF techniques*. in *Conf. Proc. of EUROMAT*. 2001.

56. Venkataraman, N., *The process-property- performance relationships of feedstock material used for fused deposition of ceramic (FDC)*, in *Ceramic and Materials Engineering*. 2000, Rutgers University.

57. McNulty, T.F., et al., *Dispersion of lead zirconate titanate for fused deposition of ceramics.* Journal of the American Ceramic Society, 1999. **82**(7): p. 1757-60.

58. Sternitzke, M., *Structural ceramic nanocomposites.* Journal of the European Ceramic Society, 1997. **17**(9): p. 1061-1082.

59. Hertzberg, R.W., *Deformation of Fracture Mechanics of Engineering Materials, Fourth Edition*. 1996, Hoboken, NJ: John Wiley and Sons.

60. Ritchie, R.O., *The conflicts between strength and toughness.* Nature materials, 2011. **10**(11): p. 817-822.

61. Ritchie, R.O., *Mechanisms of fatigue crack propagation in metals, ceramics and composites: role of crack tip shielding.* Materials Science and Engineering: A, 1988. **103**(1): p. 15-28.

62. Hannink, R.H.J., P.M. Kelly, and B.C. Muddle, *Transformation toughening in zirconia‐containing ceramics.* Journal of the American Ceramic Society, 2000. **83**(3): p. 461-487.

63. Mason, T.O. *Advanced structural ceramics*. [cited 2015 March 17th]; Available from: http://www.britannica.com/EBchecked/topic/6681/advanced-structural-ceramics/76760/Transformation-toughening.

64. Garvie, R.C., R.H. Hannink, and R.T. Pascoe, *Ceramic steel?* Nature (London), 1975. **258**: p. 703–704.

65. Hutchinson, J., *Mechanisms of toughening in ceramics.* Theoretical and applied mechanics, 1989: p. 139-144.

66. Xia, S. 2010.

67. Xia, S., Phys. Rev. Lett. , 2012. **108**.

68. Xia, S., J. Mech. Phys. Solids, 2013. **61**: p. 838-851.

69. Bernardo, E., et al., *Advanced Ceramics from Preceramic Polymers Modified at the Nano-Scale: A Review.* Materials, 2014. **7**(3): p. 1927-1956.

70. Griggio, F., et al., *Kinetic studies of mullite synthesis from alumina nanoparticles and a preceramic polymer.* Journal of the American Ceramic Society, 2008. **91**(8): p. 2529-2533.

71. Erny, T., et al., *Microstructure Development of Oxycarbide Composites during Active‐Filler‐Controlled Polymer Pyrolysis.* Journal of the American Ceramic Society, 1993. **76**(1): p. 207-213.

72. Greil, P., *Active‐Filler‐Controlled Pyrolysis of Preceramic Polymers.* Journal of the American Ceramic Society, 1995. **78**(4): p. 835-848.

73. Greil, P., *Near net shape manufacturing of polymer derived ceramics.* J. Eur. Ceram. Soc 1998. **18**: p. 1095–1114.

74. Greil, P., *Polymer-filled derived ceramics with hierarchical microstructures.* Key Eng. Mater 1999. **159–160**: p. 339–346.

75. Greil, P., *Polymer derived engineering ceramics.* Adv. Eng. Mater 2000. **2**: p. 339–348.

76. Greil, P. and M. Seibold, *Modelling of dimensional changes during polymer-ceramic conversion for bulk component fabrication.* Journal of materials science, 1992. **27**(4): p. 1053-1060.

77. Seibold, M. and P. Greil, *Thermodynamics and microstructural development of ceramic composite formation by active filler-controlled pyrolysis (AFCOP).* Journal of the European Ceramic Society, 1993. **11**(2): p. 105-113.

78. Schwartz, K.B. and D.J. Rowcliffe, *Modeling density contributions in preceramic polymer/ceramic powder systems.* Journal of the American Ceramic Society, 1986. **69**(5): p. C‐106-C‐108.

79. Seyferth, D., et al., *Preceramic polymers as "reagents" in the preparation of ceramics.* Journal of the American Ceramic Society, 1991. **74**(10): p. 2687-2689.

80. Zocca, A., et al., *SiOC ceramics with ordered porosity by 3D-printing of a preceramic polymer.* Journal of Materials Research, 2013. **28**(17): p. 2243-2252.

81. Hassanin, H. and K. Jiang, *Fabrication of Al2O3/SiC Composite Microcomponents using Non‐aqueous Suspension.* Advanced Engineering Materials, 2009. **11**(1‐2): p. 101-105.

82. Jeon, S. *grbl*. March 15th, 2015 [cited 2015 March 19th]; Available from: https://github.com/grbl/grbl/wiki.

83. *Universal-G-Code-Sender*. March 12th, 2015 [cited 2015 March 19th]; Available from: https://github.com/winder/Universal-G-Code-Sender.

84. Bernardo, E., G. Parcianello, and P. Colombo, *Novel synthesis and applications of yttrium silicates from a silicone resin containing oxide nano-particle fillers.* Ceramics International, 2012. **38**(7): p. 5469-5474.

85. Gaytan, S.M., et al., *Fabrication of barium titanate by binder jetting additive manufacturing technology.* Ceramics International, 2015.

86. Shahzad, K., et al., *Additive manufacturing of zirconia parts by indirect selective laser sintering.* Journal of the European Ceramic Society, 2014. **34**(1): p. 81-89.

87. Badrinarayanan, S., S. Sinha, and A.B. Mandale, *XPS studies of nitrogen ion implanted zirconium and titanium.* Journal of electron spectroscopy and related phenomena, 1989. **49**(3): p. 303-309.

88. Gross, T., et al., *An XPS analysis of different SiO2 modifications employing a C 1s as well as an Au 4f7/2 static charge reference.* Surface and interface analysis, 1992. **18**(1): p. 59-64.

89. Mavel, G., et al., *ESCA surface study of metal borides.* Surface Science, 1973. **35**: p. 109-116.

90. Powell, C.J., *Recommended Auger parameters for 42 elemental solids.* Journal of Electron Spectroscopy and Related Phenomena, 2012. **185**(1): p. 1-3.

91. Yu, S.H., et al., *Pyrolysis of Titanium‐Metal‐Filled Poly (siloxane) Preceramic Polymers: Effect of Atmosphere on Pyrolysis Product Chemistry.* Journal of the American Ceramic Society, 1995. **78**(7): p. 1818-1824.

92. *Hysitron Nanomechanical Testing Probe Selection Guide*. [cited 2015 March 17th]; Available from: http://www.hysitron.com/Default.aspx?tabid=120.

93. Gdoutos, E.E., *Fracture mechanics: an introduction*. Vol. 123. 2006: Springer Science & Business Media.

94. *Diamond, Synthetic*. [cited 2015 Marth 17th]; Available from: http://www.matweb.com/search/DataSheet.aspx?MatGUID=4b8970a9250943a882a509f1dc637280&ckck=1.

95. Greaves, G.N., et al., *Poisson's ratio and modern materials.* Nature materials, 2011. **10**(11): p. 823-837.

96. Parcianello, G., E. Bernardo, and P. Colombo, *Mullite/zirconia nanocomposites from a preceramic polymer and nanosized fillers.* Journal of the American Ceramic Society, 2011. **94**(5): p. 1357-1362.

97. Barsoum, M. and M.W. Barsoum, *Fundamentals of ceramics*. 2002: CRC Press.

98. D. Burton, P.L., A. Palmer. *Properties and Applications of Carbon Nanofibers (CNFs) Synthesized using Vapor-grown Carbon Fiber (VGCF) Manufacturing Technology*. [cited 2015 March 15th]; Available from: http://www.sigmaaldrich.com/materials-science/nanomaterials/carbon-nanofibers.html.

99. Maensiri, S., et al., *Carbon nanofiber-reinforced alumina nanocomposites: Fabrication and mechanical properties.* Materials Science and Engineering: A, 2007. **447**(1): p. 44-50.

100. Hyuga, H., et al., *Processing and tribological properties of Si3N4/carbon short fiber composites.* Journal of the American Ceramic Society, 2003. **86**(7): p. 1081-1087.

101. Clarke, T.A. and E.N. Rizkalla, *X-ray photoelectron spectroscopy of some silicates.* Chemical Physics Letters, 1976. **37**(3): p. 523-526.